Quantifying Intermolecular Interactions in Asymmetric Peptide Organocatalysis as a Key Towards Understanding Selectivity

Jens Nowag,¶ Matthias Brauser,¶ Raffael C. Wende,§ Peter R. Schreiner,§ and Christina M. Thiele*,¶

¶*Clemens-Schöpf-Institut für Organische Chemie und Biochemie, Technische Universität Darmstadt, Peter-Grünberg-Straße 16, D-64287 Darmstadt, Germany*
§*Institute of Organic Chemistry, Justus Liebig University, Heinrich-Buff-Ring 17, D-35392 Giessen, Germany*

E-mail: cthiele@thielelab.de

Abstract

The kinetic resolution of *trans*-cyclohexane-1,2-diol with a lipophilic oligopeptide catalyst shows extraordinary selectivities. To improve our understanding of the factors governing selectivity, we quantified the Gibbs energies of interactions of the peptide with both enantiomers of *trans*-cyclohexane-1,2-diol using nuclear magnetic resonance (NMR) spectroscopy. For this we use advanced methods such as transverse relaxation (R_2), diffusion measurements, saturation transfer difference (STD), and chemical shift (δ) analysis of peptide-diol mixtures upon varying their composition (NMR titrations). The methods employed give comparable and consistent results: The molecular recognition by the catalyst is approx. $3\,\mathrm{kJ\,mol^{-1}}$ in favor of the preferentially acetylated (R,R)-enantiomer in the temperature range studied. Interestingly, the difference of $3\,\mathrm{kJ\,mol^{-1}}$ is also confirmed by results from reaction monitoring of the acylation step under catalytic conditions, indicating that this finding is true regardless of whether the investigation is performed on the acetylated species or on the free catalyst. To arrive at these conclusions the self-association of both catalyst and substrate in toluene were found to play an important role and thus need to be taken into account in reaction screening.

Introduction

Asymmetric organocatalysis is a versatile tool for the synthesis of enantiomerically enriched compounds,[1] and is often employed in drug development.[2] A particular class of catalysts used for this purpose are oligopeptides.[3–6] Those peptides can be readily prepared by well established peptide synthesis protocols and may contain natural as well as unnatural amino acids.[7–10] Such tailor-made peptides often adopt a preferred conformation, thus providing a binding site for the substrate akin to enzymatic pockets.[11] Enzymes form energetically different transition states with the two enantiomers of a chiral substrate resulting in one reaction pathway being faster with one enantiomer than the other. This selectivity towards a specific enantiomer can be exploited to separate both enantiomers from a racemate in a kinetic resolution.[12] The active site of an enzyme has usually evolved to accept a very specific scope of substrates. Oligopeptides functioning as catalysts – on the other hand – are designed as small-molecule analogs of enzymes, offer tunable properties and can be readily modified. This allows for a larger substrate scope.

Understanding the mode of actions of these catalysts is essential for further improvement of their selectivity and substrate scope. The system investigated here, is tetrapeptide **1** (Scheme 1), which shows excellent selectivities in the kinetic resolution of *trans*-cycloalkane-

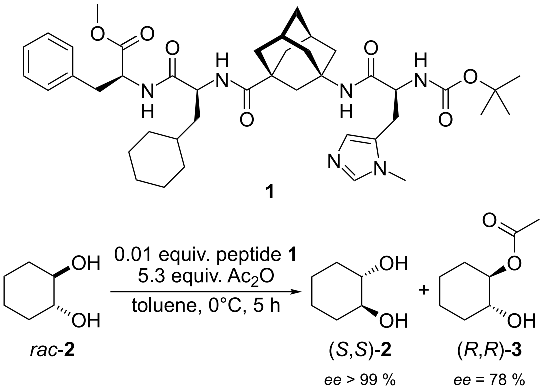

Scheme 1: Kinetic resolution of racemic *trans*-cyclohexane-1,2-diol **2** with the peptide catalyst Boc-L-(π-Me)-His-^{A}Gly-L-Cha-L-Phe-OMe (**1**).[13]

https://doi.org/10.26434/chemrxiv-2023-8sgz7 **ORCID:** https://orcid.org/0000-0001-7876-536X

1,2-diols via monoacylation.[13,14] The catalytically active amino acid π-methylhistidine has been complemented by phenylalanine to increase the solubility in organic solvents. The γ-aminoadamantanecarboxylic acid ($^{\mathrm{A}}$Gly) is thought to induce a turn-like structure in the peptide,[15] thereby creating a cavity mimicking an enzymatic pocket. The last amino acid cyclohexylalanine has been determined by catalyst screening to give the highest selectivities. It has been found that the highest selectivities were observed at low concentrations – this parallels previous findings for other organocatalysts.[16–22]

It was proposed that the high enantioselectivity ($s > 50$)[23] at reaction conditions results from complex formation of **1** with **2**, which should be stronger with the faster reacting enantiomer of **2**.[13,14] Thus the complex with the faster reacting enantiomer (R,R)-**2** would actually be stronger. This implies some kind of molecular recognition of (R,R)-**2** by peptide **1** during catalysis. However, little experimental proof of this complex formation is available to date. We investigate here, whether this complexation can be detected and quantified and whether differences between the two enantiomers can be observed.

Nuclear magnetic resonance (NMR) spectroscopy is well suited for non-invasive investigations under conditions, that are close to the reaction conditions[24–27] as NMR spectroscopy allows the detection of very weak binding processes.[28–30] Previous NMR investigations of mixtures of **1** and **2** showed first indications of a complexation via small changes in chemical shifts (δ), longitudinal relaxation rates (R_1) and translational diffusion coefficients (D) and thus provided first hints that the faster reacting enantiomer (R,R)-**2** shows qualitatively stronger binding than the (S,S)-enantiomer.[31] In our previous study[31] mainly samples containing equimolar mixtures of peptide and the two respective diols were investigated. These conditions are quite far from the catalytic ones,[13,14] a weakness we aim to eliminate here.

Importantly, previous measurements of peptide **1** have shown dependencies, *e.g.*, of the chemical shift, on temperature and concentration,[31] which are identified here as resulting mainly from self-association. For alcohols in general and diol **2** in particular, this behavior is also known in non-polar solvents and has already been investigated by infrared (IR) spectroscopy and also by NMR spectroscopy.[32–36] Since potential (weak) nonconvalent interactions of **1** with **2** may be affected by self-association, both compounds first need to be investigated separately to determine the impact of self-association. Only after that mixtures can be investigated properly.

Since no separate signal sets can be observed in the NMR spectra of mixtures of **1** and **2**, the process must be in the fast exchange limit with respect to the NMR time scale. This implies the presence of transient catalyst-substrate species. To detect these transient complexes and quantify their strengths by NMR, we use several NMR techniques at various concentrations and ratios of **1** and **2** as is required by some of the methods.[29]

The parameter that one would consider the most obvious one to probe non-covalent catalyst-substrate interactions also employed herein are proton chemical shifts while varying the concentrations of the respective species.[29,30] During these so called NMR titrations, chemical shifts of both catalyst and substrate show changes in case of a binding event. This is also exploited herein, but needs carefully designed experiments and rather sophisticated analysis as self-aggregation of both **1** and **2** is present while catalyst substrate complexes are investigated.

One potential reason for aggregation is hydrogen bonding.[37,38] To investigate their importance for self-aggregation of **1**, the temperature dependency of chemical shifts is exploited measuring so called temperature coefficients. These have been well studied for amide protons in proteins, and classifications have been made whether the proton is part of a hydrogen bond.[39] While these classifications were initially made for proteins, it has been proposed that these are also applicable for molecules of a similar size as tetrapeptide **1**.[40,41]

Furthermore, diffusion measurements are used to study binding events – both self-aggregation and the formation of transient substrate-catalyst complexes. The diffusion coefficient depends on the hydrodynamic radius and thus roughly on the size of the diffusing complex. Thus, diffusion coefficients for complexes are smaller than those of unrestrictedly diffusing binding partners[29,42,43] and a decreasing diffusion coefficient potentially indicates a binding event. As is shown here diffusion measurements also allow distinguishing between different models employed in the chemical shift analysis of self-aggregation of tetrapeptide **1**. Finally, we show that saturation transfer difference (STD)[44] is suitable to detect the intermolecular interactions present here. In STD experiments detectable magnetization builds up, when one binding partner is selectively irradiated and interacts with the other. STD is a common tool in the context of drug binding,[29,45] where there usually is a large difference in molecular weights and rotational correlation times of the interacting species. It is to note, that here we envisioned investigating the binding of compounds much smaller than proteins. To the best of our knowledge, we show here for the first time that STD can detect interactions in (peptide) catalysis and allows quantifying the interactions present. Whether the aggregation present in this system is essential to observe STD and whether STD becomes generally applicable to catalyis screening remains to be seen in the future.

Thus, in the present manuscript we investigate the interactions between the tetrapeptide catalyst **1** and both enantiomers of diol **2**. We used different NMR methods to quantify the affinities of **1** for (R,R)-**2** and (S,S)-**2**. They are in excellent agreement with each other and with the previously determined selectivities under catalytic conditions.[13,14] Finally, we monitor the acetylation under catalytic conditions NMR spectroscopically and determine the reaction rates. Also here a difference of $3\,\text{kJ mol}^{-1}$ is observed. In order to do all these investigations, self-association had to be investigated first.

.

Results & discussion

Self-Association of Tetrapeptide

Contrary to the original design intention,[13] some form of peptide self-association is observable in toluene. This could be qualitatively shown in previous NMR spectroscopic studies.[31,46] As the determination of the solution structure was one goal of the previous study, the peptide concentration was chosen significantly higher in the previous NMR studies due to sensitivity reasons ($[\text{P}] \approx 3.2\,\text{mM}$ to $19.7\,\text{mM}$[31]) compared to the actual reaction conditions ($[\text{P}] \approx 0.1\,\text{mM}$ to $1\,\text{mM}$[13,14,47]). Thus, a quantitative evaluation of self-association becomes necessary, since its effects might obscure the effect of complexation of the diols when investigating the interactions between substrate and catalyst. This is accomplished NMR spectroscopically by following the proton chemical shifts of **1** in toluene-d_8 in the concentration range from $0.1\,\text{mM}$ to $19.9\,\text{mM}$ and a temperature range from $270\,\text{K}$ to $310\,\text{K}$. At $300\,\text{K}$ a concentration of up to $20\,\text{mM}$ can be obtained, but the solubility decreases with lower temperatures, so that at $270\,\text{K}$ only an approximately $3\,\text{mM}$ solution is feasible. If the solubility limit is exceeded inhomogeneities emerge, resulting in asymmetric signals, broader linewidths and decreased signal intensities. The chemical shifts of **1** show a significant change upon variation of concentration. This is an indication of changes in the position of the chemical equilibrium in toluene (amide proton $^{\text{P}}$H16 shown in Figure 1A; superscript P and D are referring to peptide and diol, respectively; for nuclei numbering see SI section 1).

As chemical shifts obey equation 1 in the context of fast exchange, a plausible chemical equilibrium model for the self-association of **1** must be defined, in order to describe the data obtained analytically.

$$\langle \delta_j \rangle = \sum_i \alpha_i \; \delta_{i,j} \tag{1}$$

The averaged, observed chemical shift $\langle \delta_j \rangle$ of resonance j depends on the weight fractions in equilibrium α_i of a molecular species i with corresponding chemical shift of $\delta_{i,j}$ of that species. Both, the weight fractions and chemical shifts in the pure species must be fitted against the experimental data. The chemical shifts of peptide **1** obtained in toluene-d_8 between $270\,\text{K}$ and $310\,\text{K}$ are subjected to a global analysis,[30,48] where the individual isotherms of each proton are fitted simultaneously over all temperatures (see SI section 3 for details). The fit is done under the assumption that the linear form of the Van 't Hoff equation is valid, which assumes the heat capacity to be constant. As underlying model we assume the isodesmic model (equal-K-model)[49,50] for a stepwise aggregation of peptide monomers to form an oligomer distribution (Eq. 2), whereby K^{iso} is the corresponding equilibrium constant and is equal for all equilibrium steps.

$$\text{P}_{i-1} + \text{P} \overset{K^{\text{iso}}}{\rightleftharpoons} \text{P}_i \qquad i = 2 \ldots \infty \tag{2}$$

As a simplification, in the isodesmic model dimers and higher oligomers are combined into one species P_ξ, so that only monomers P and the self-associates (oligomers) P_ξ can be distinguished. Fitting the chemical shifts to the isodesmic model results in a solution with a small RMSD. The chemical shifts themselves do not show any discontinuity, which would indicate an improperly chosen model. The obtained enthalpy and entropy of self-association are $\Delta H = (-41.82 \pm 4.03)\,\text{kJ mol}^{-1}$ and $\Delta S = (-94.50 \pm 13.45)\,\text{J K}^{-1}\,\text{mol}^{-1}$, respectively. As Figure 1C shows that peptide self-association is driven by an energy gain of roughly $-15\,\text{kJ mol}^{-1}$ in the temperature range studied, thus rendering this a non-negligible interaction. From the chemical shift analysis, it is possible to calculate the peptide monomer weight fraction at reaction conditions by intrapolating ΔG to $273\,\text{K}$ and extrapolating the total peptide concentration $[\text{P}]_t$ to $108\,\mu\text{M}$, resulting mainly in a peptide monomer (P) population of about $81\,\text{mol\%}$.

Apart from the isodesmic equilibrium a monomer-dimer equilibrium is also possible. As these are formally indistinguishable by chemical shifts,[49] we take diffusion coefficients as an absolute reference for the self-association into account. Diffusion coefficients extracted from double stimulated echo experiments[51] exhibit the same trends upon variation of concentration or temperature as chemical shifts do (data shown in SI section 4). At low concentration ($[\text{P}] = 0.07\,\text{mM}$) diffusion measurements lead to a hydrodynamic radius of $r_h = (7.2 \pm 0.2)\,\text{Å}$, which is in perfect agreement with monomeric peptide **1**, for which a radius of $(7.5 \pm 0.7)\,\text{Å}$ is predicted when applying an empirically derived power law[52] (see SI section 4.1 for calculations). For higher concentrations the corresponding diffusion coefficients are reproduced accurately, when accounting for the oligomer distribution in the isodesmic equilibrium proposed by Price.[43,50] For this the equilibrium constants determined from the chemical shifts are used as input (see SI section 4.2).

From the back-calculated chemical shifts corresponding to monomer and oligomers, the trend of shift versus temperature can be evaluated further to investigate potential hydrogen bonding: For amide protons, the temperature dependencies in organic solvents have been well studied and classifications[40] have been made as to when an amide proton forms a hydrogen bond (HB) to an acceptor. When a proton is not involved in a hydrogen bond, it is accessible to the solvent and thus the temperature dependency of the chemical shift of that proton is stronger (more negative). In turn, the chemical shifts of protons within a hydrogen bond are mainly unaffected by a change in temperature. To extract the temperature coefficients (TC) the chemical shifts of P and P_ξ derived from the global fit are subjected to a linear regression against the temperature (see SI section 5 for the fits). The slope is equal to TC and is shown in Figure 2 for all amide protons present in peptide **1**. Note, however, that the acceptor for any hydrogen bond formed may not be derived from the analysis of ^{1}H chemical shifts.

A small temperature coefficient in the monomer can be directly interpreted as an intramolecular hydrogen bond as it is the case for ^{P}H25. The species P_ξ needs to be treated differently, since the chemical shifts derived for this species are an average over the oligomer distribution present. Therefore, the observed TC is also an average over all oligomers, and the interpretation must be made in relation to the TC of the monomer: For protons ^{P}H7 and ^{P}H31, no significant change is observed in the transition from monomer to oligomer and thus in self-association. We therefore assume that no change of the H-bonds upon self-association occurs. Proton ^{P}H7 is not involved in a hydrogen bond in either species, while ^{P}H31 shows an intramolecular H-bond in both species. ^{P}H16 shows a very large TC in the monomer, and would thus usually be classified as not H-bonded. Its large TC would be ascribed to a conformational change in the usual classification. In the species P_ξ the TC value of ^{P}H16 is in the range of "no hydrogen bond" but strongly reduced with respect to the monomer. While these values do not match the usual classifications, the large change when going from monomer to self-associated species is notable. Since TC is an average of all ^{P}H16 in P_ξ, this value could result from the protons being only partially involved in an H-bond.

The energy gain from forming an H-bond (4 kJ mol^{-1} to 60 kJ mol^{-1})[53] corresponds well to the enthalpy of association determined by the analysis of chemical shifts (*vide supra*). The proton ^{P}H25 does not contribute to this, as the intramolecular hydrogen bond present in the monomer weakens for P_ξ as compared to the monomer.

We note that, this quantitative analysis of the temperature coefficents only gives a thermodynamic picture of the self-association equilibrium and does not directly allow structural interpretations.

The peptide self-association also has been examined in dichloromethane, where the experimentally observed selectivity of the kinetic resolution (Scheme 1) is significantly lower and the reaction slower than in toluene,[13] as well as in acetone. Both solvents are shown to impede H-bonding to some extent.[54–56] In both solvents a decreased self-association is observed in our NMR analyses compared to toluene (see SI section 6). This could indicate that (H-bonded driven) self-association is a factor to take into account in peptide organocatalysis as previously also shown for other organocatalytic processes[19,21,22]

Thus if one suspects that catalyst self-association is present in an organocatalytic process, we recommend performing an NMR titration and to additionally determine whether higher selectivities are achieved as a function of catalyst concentration. If selectivities are highest at low concentrations, self-association could be counteracted by chemically modifying the sites responsible for self-association, which could be identified using temperature coefficients. On the other hand, if the highest selectivities are achieved at high catalyst concentrations, it may be possible to further strengthen the interactions responsible for self-association either by increasing the number of interaction sites or by even covalently linking the monomers.

Self-Association of *trans*-Cyclohexane-1,2-diol

As self-association of *trans*-cyclohexane-1,2-diol (**2**) might obscure the interaction of **1** and **2**, it is also necessary to investigate its self-association in toluene. This was accomplished by NMR spectroscopy following the

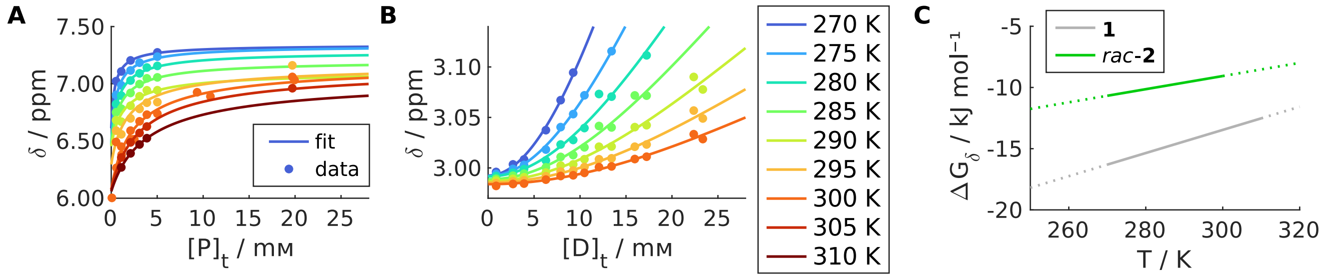

Figure 1: Change of the chemical shifts for ^{P}H16 of **1** (A) and ^{D}H1 of *rac*-**2** (B) versus (A) the total peptide $[P]_t$ and (B) total diol $[D]_t$ concentration in toluene-d_8 at different temperatures. Measured data are represented by ●, while the solid lines represent the back-calculated chemical shifts from the global fit. (C) Plot of the Gibbs energies for the self-association of **1** and **2** derived from global fitting assuming the equilibria as defined in the text. The solid line corresponds to the measured temperature range, whereas the dotted line is extrapolated from the retrieved fit parameters.

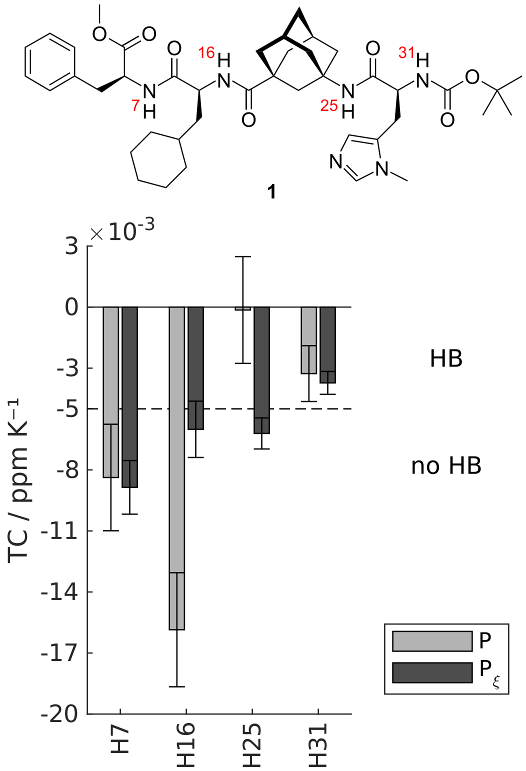

Figure 2: Temperature coefficients (TC) of the amide protons in peptide **1** (numbering of amide protons shown above) separated into the species P and P_ξ. Classification as hydrogen bond (HB) or no HB is taken from reference 40 for the solvent toluene.

proton chemical shifts of *rac*-**2** in toluene-d_8 in the concentration range from 0.9 mM to 23.4 mM and a temperature range from 270 K to 300 K. As Figure 1B shows for proton $^{\mathrm{D}}$H1 of diol **2** (aliphatic proton geminal to the hydroxy group), the chemical shift changes depending on both concentration and temperature. All other proton chemical shifts experience a similar trend. At lower temperatures fewer data points are available as the solubility of **2** in toluene decreases, which leads to decreased signal intensities and inhomogeneities, in the same manner as described for the peptide.

IR spectroscopic investigations at room temperature have shown previously, that self-associates consist mainly of diol trimers in tetrachloromethane.[36] Tetrachloromethane has a similar relative permittivity as toluene (2.22 vs. 2.31 at 300 K[57]), so the conclusions drawn on the self-association of diol **2** in tetrachloromethane may be adopted for toluene. Thus, we define the self-association of diol **2** as simultaneous association of three diol monomers (D) to the trimer (D_3) (Eq. 3), but we also discuss the association in two steps via the diol dimer in the SI (section 3.3.3).

$$3\,\mathrm{D} \overset{K^{\mathrm{diol}}}{\rightleftharpoons} \mathrm{D}_3 \tag{3}$$

The global fit of all proton shifts gave a satisfactory result for the monomer-trimer model (Eq. 3), as all extracted chemical shifts of diol monomer and diol trimer are in a reasonable range. The isotherms derived are plotted in Figure 1B as solid line. The fit reproduces the experimental chemical shifts accurately. The assigned overall enthalpy and entropy of this equilibrium model are $\Delta H = (-25.17 \pm 12.97)\,\mathrm{kJ\,mol^{-1}}$ and $\Delta S = (-53.69 \pm 45.63)\,\mathrm{J\,K^{-1}\,mol^{-1}}$, respectively. With a Gibbs energy gain of roughly $-10\,\mathrm{kJ\,mol^{-1}}$ in the studied temperature range the diol self-association is less pronounced as compared to the peptide self-association. This is also reflected in Figure 1C. It nonetheless needs to be taken into account when investigating the interactions of **1** and **2**.

Complexation of *trans*-Cyclohexane-1,2-diol with Tetrapeptide

With the known self-association of substrate and catalyst, the interactions between peptide **1** and both enantiomers of diol **2** can now be studied in detail. For this, the interactions in (separate) mixtures of **1** with (*R*,*R*)-**2** and **1** with (*S*,*S*)-**2** were investigated using saturation transfer difference (STD), diffusion-ordered spectroscopy, and chemical shift analysis.[29,30]

Saturation Transfer Difference. In STD measurements, detectable magnetization accumulates on the substrate if it binds to the catalyst, while the catalyst is selectively irradiated. The exemplary STD spectra in Figure 3 indicate stronger binding of (*R*,*R*)-**2** than (*S*,*S*)-**2** to **1**. This is evidenced by more intense signals of (*R*,*R*)-**2** (blue) as compared to the signals of (*S*,*S*)-**2** (red) in a mixture with **1** at otherwise identical conditions. Also, the hypothesis that the diol enters a pocket formed by peptide **1** with both hydroxy groups

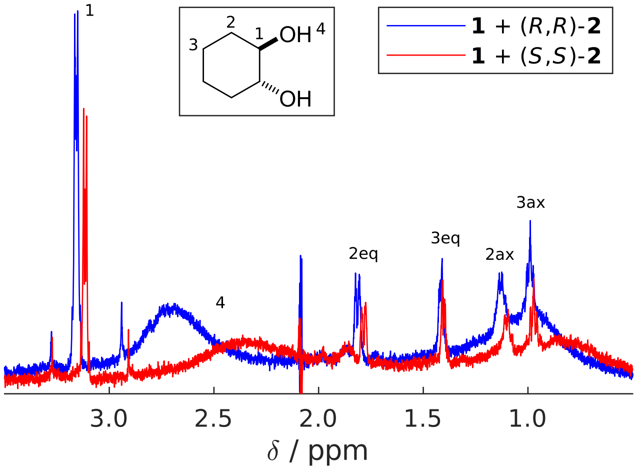

Figure 3: ^{1}H STD spectrum of (*R*,*R*)-**2** (blue) and (*S*,*S*)-**2** (red) with identical settings (10 s of selective irradiation on peptide **1**) at 270 K on a 700 MHz spectrometer in toluene-d_8. The concentrations are 10 mM of **2** and 0.5 mM of **1**. Inset: Numbering of **2**.

ahead,[14] is supported by the trend of intensities of the STD responses with decreasing intensities from proton $^{\mathrm{D}}$H1 (most intense signal) to the other aliphatic protons (less intense signals).

For the quantitative evaluation the resonance of the hydroxy group $^{\mathrm{D}}$H4 would be of particular interest, but is broadened presumably due to hydrogen bonding and thus not visible in most spectra. Nonetheless, the resonance $^{\mathrm{D}}$H1, which is next to the hydroxy group, is the most intense signal in the difference spectra and is available as a reporter for the whole substrate to obtain quantitative information on binding affinities.

From a series of STD spectra at different saturation times, temperatures, and concentrations equilibrium constants were obtained. At all temperatures and concentration ratios typical saturation build up curves were recorded for both enantiomers of **2** (see SI section 8 for an exemplary build up curve and details on the evaluation procedure). The equilibrium constants obtained can be expressed as Gibbs energies. We determined an energy gain of about $-6\,\mathrm{kJ\,mol^{-1}}$ to $-9\,\mathrm{kJ\,mol^{-1}}$ for the complexation of the (R,R)-enantiomer by peptide **1** with increasing temperature. On the other hand the (S,S)-enantiomer only shows an energy gain of around $-5\,\mathrm{kJ\,mol^{-1}}$, which also seems to be less dependent on temperature. The more negative Gibbs energy means that (R,R)-**2** quantitatively interacts more strongly with **1** than (S,S)-**2**. Note that both binding affinities are in the range of weak interactions.[29]

In general, STD measurements show a response as soon as magnetization can be transferred. This can be modeled in the simplest case by a 1:1 complex, and therefore the equations for analysis were developed assuming the presence of a 1:1 complex.[28,45] The stoichiometry of the complexes, however, cannot be derived by STD, since a magnetization transfer would happen in any stoichiometric ratio. Due to the rapid exchange between peptide **1** as monomer and oligomers and the diol **2** as monomer and trimer various combinations are possible. Therefore, only the combined apparent equilibrium constant K^{STD} of an arbitrary m:n-complex is accessible from the STD measurements (Eq. 4):

$$\mathrm{m\,P + n\,D} \xrightleftharpoons{K^{\mathrm{STD}}} \mathrm{P_m D_n} \tag{4}$$

The STD amplifications are potentially biased by the self-association of peptide and diol due to the fact that the amplifications determined are influenced by the ratio of diol and peptide concentrations (see SI section 8). It is unclear whether the magnetization transfer is equally efficient when starting from selectively irradiated monomer versus starting from the oligomer. This would be a necessary assumption for further evaluation. However, a bias by the peptide oligomers can be minimized by measuring STD amplifications at conditions that favor the monomeric state.[58] At the chosen concentration of $0.5\,\mathrm{mM}$ **1** the peptide-peptide equilibrium constant predicts a molar monomer fraction, that depends on temperature and ranges from 83 % (300 K) to 46 % (270 K). Due to the changing peptide self-association equilibrium, a temperature dependency of the complexation may be present, but thus would be masked. Therefore, the STD measurements can only be taken as an estimate of the complexation and further investigations are necessary.

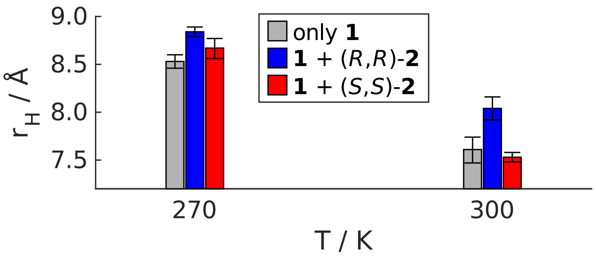

Figure 4: The hydrodynamic radii of the peptide **1** derived from diffusion measurements reveal an increase at 270 K and 300 K for the mixture with 20-fold excess of (R,R)-**2** over the sample without any diol. At the same conditions **1** shows no significant increase with (S,S)-**2** present. At 270 K the higher radii are dominated by the peptide self-association, but still with (R,R)-**2** an increase is observable.

Diffusion Coefficients. Binding events can also be detected by the measurement of translational diffusion.[29,43] The diffusion coefficient is related to the hydrodynamic radius and thus a direct reporter on the size of a diffusing species. In the context of small molecules, any additionally bound species decreases the diffusion coefficient. Using a large excess of the binding partner helps shifting the equilibrium towards a transient complex, such that the largest possible change in diffusion coefficient is obtained. Here we have examined the peptide resonances in 20-fold excess of the diol and without diol for comparison at 270 K and 300 K. From the diffusion coefficients we derived the hydrodynamic radii, assuming spherical hydrodynamic volumes for all occurring species. The hydrodynamic radius of the peptide increases at lower temperatures (Figure 4B, gray bars) due to self-association, as shown above (see section peptide self-association and SI section 4).

In the presence of a 20-fold excess of (R,R)-**2** a significant increase in hydrodynamic radius is observed, at both low (270 K) and high (300 K) temperatures. With (S,S)-**2** no significant increase of the radius is observed. This indicates tighter binding of (R,R)-**2** versus (S,S)-**2** and thus supports the data derived by STD at both temperatures. Any complex formed by **1** and (S,S)-**2** must thus be present at such low concentrations, that no change in diffusion coefficient is detected. However, these are still high enough to produce reasonable STD amplifications as discussed above.

Chemical Shifts. Since the binding energies and diffusion coefficients determined so far provide only semi-quantitative trends, a chemical shift titration is per-

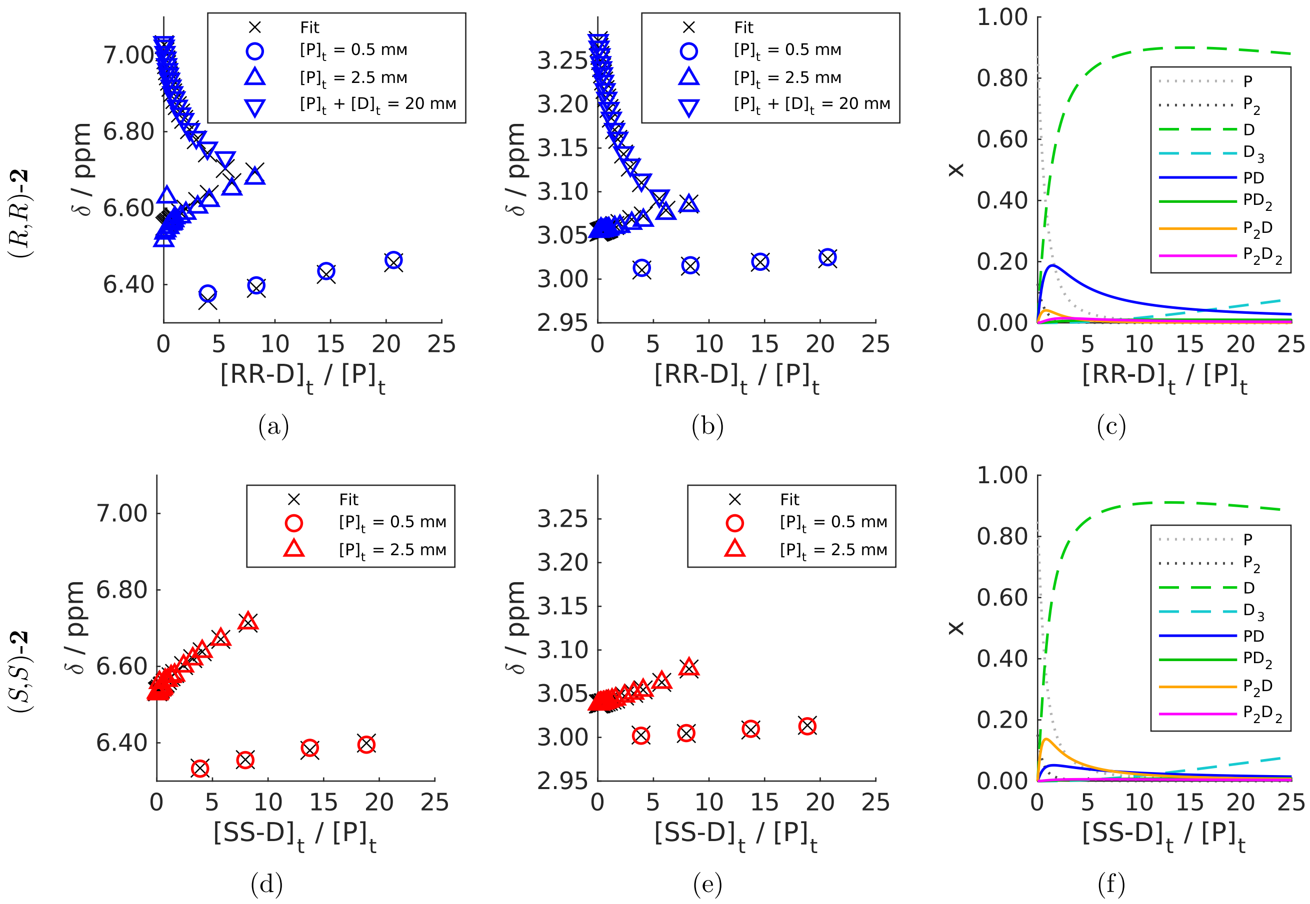

(a) (b) (c)

(d) (e) (f)

Figure 5: Chemical shifts of amide proton ^{P}H16 in **1** (a) and (d) and aliphatic proton ^{D}H1 in **2** (b) and (e) versus molar excess of **2**. The titrations of **1** with (R,R)-**2** (top row) and **1** with (S,S)-**2** (bottom row) were performed at 300 K. The fit was performed with the equilibrium model EM-PD8, which includes peptide self-association, diol self-association, and various peptide-diol complexes (see Eqs. 2, 3, and 5 to 8 and SI section 3.3.13). Plots (c) and (f) display the molar fractions derived from the fit at a constant peptide concentration of 2.5 mM.

formed. This usually is the best source of quantitative information in the absence of self-association, but requires quite a demanding analysis in its presence. It is important to note, that a model describing the experimental data needs to be consistent for both enantiomers of **2**. Additionally, the chemical shifts of both compounds under investigation (**1** with (R,R)-**2** or **1** with (S,S)-**2**) need to be fitted simultaneously. From the results discussed above it is evident that both **1** and **2** form higher aggregates. Analyzing both compounds in mixtures significantly increases the number of possible combinations of equilibrating species to be considered when modelling complex formation. From STD and diffusion data we conclude that a complex of **1** must be present with **2**. However, no information on the stochiometry of this complex could be obtained from this data (see above).

The influence of the peptide oligomers can be reduced by selecting conditions that favor the monomeric state, which is achieved either by lower concentrations or higher temperatures. We have therefore decided to perform several titrations at 300 K, while keeping the peptide concentration constant (△ in Figure 5), which is recommended if self-association is present.[59] The variation according to Job (constant total concentrations)[60,61] has also been done for **1** with (R,R)-**2** (▽ in Figure 5). However, the classical Job plot analysis fails due to the weak binding affinities and the presence of multiple equilibria.[62]

The chemical shift is even more sensitive to changes in the environment than STD amplifications or diffusion coefficients.[29] Thus, the simple model that leads to a 1:1 complex of peptide and diol monomer (Eq. 5) is not sufficient to describe the chemical shifts of **1** and **2** in a simultaneous fit without significant systematic deviation. Even if both equilibria (Eqs. 2 and 3) from the first sections are also included, the fit is not satisfactory (see SI section 3.3.6 for fitting result).

$$\mathrm{P} + \mathrm{D} \rightleftharpoons \mathrm{PD} \qquad (5)$$

As shown in Figure 5a) and b), the chemical shifts of **2** also depend on the peptide concentration, which in turn changes the peptide monomer to oligomer ratio. Therefore, a more complex equilibrium model is necessary to adequately describe the data. The description of the peptide self-association with Eq. 2 is done using an equilibrium model that considers an infinite number of equilibrium steps. If now all possible oligomers would be allowed to interact with **2** the resulting model would be far too complex. Thus we restricted the model employed here by only considering the dimeric peptide species interacting with diol **2**. The diol shifts at low diol concentration are reproduced well if P_2D is included as additional species (Eq. 6). However, both peptide and diol shifts deviate from the calculated values at higher diol concentrations. Thus, higher complexes need to be considered (Eqs. 7 and 8). This leads to a fitting result in which all chemical shifts of all selected protons are in accordance with our spectroscopic findings.

$$P_2 + D \rightleftharpoons P_2D \tag{6}$$

$$PD + D \rightleftharpoons PD_2 \tag{7}$$

$$P_2D + D \rightleftharpoons P_2D_2 \tag{8}$$

All fitted equilibrium models describing the mixture are shown in detail in the SI (starting from section 3.3.5). The introduction of more fit parameters generally leads to a better fit, but may also over-fit the data. This is not the case here. With each signal included in the analysis, the number of data points increases by the number of concentrations measured, but the number of fit parameters increases only by the number of species included in the model. In general, the number of species is smaller than the number of measured concentrations, and thus considering as many signals as possible in a global analysis is advantageous.[30] The number of data points ($N = 957$) is sufficiently high, such that in the global fit still a high degree of freedom ($df = 695$) in the case of **1** with (R,R)-**2** is preserved. Furthermore, this complex model is justified by the significant improvement of the root mean square deviation (RMSD).[30]

As a nice feature, the global fitting procedure yields information on the composition of the respective mixtures and thus the position of the respective equilibrium: Figures 5c) and f) show which species are present to which extent at a peptide concentration of 2.5 mM as a function of molar excess. Interestingly, for diol (R,R)-**2** the 1:1 complex PD is the major peptide-diol complex, while other peptide-diol species are negligible. In contrast, the species P_2D is the predominant one for (S,S)-**2**, while the 1:1 complex is much less concentrated. When comparing the equilibrium composition at 20-fold excess of diol, these figures nicely reflect the observations from the diffusion measurements, in which a higher hydrodynamic radius for the peptide **1** was observed at 20-fold excess of (R,R)-**2** than with (S,S)-**2**.

Additionally to the qualitative finding that the two enantiomers seem to have different affinities to the aggregates, with (R,R)-**2** favouring the 1:1 complex (*i.e.*, the monomer) over the 2:1, while (S,S)-**2** favours the aggregate(s), the global fitting procedure also provides ΔG. Thus an evaluation in terms of $\Delta\Delta G$ is possible for the mixtures with the two enantiomers.

These numbers can be compared to the ones obtained from the STD enhancement factors, if the concentrations used for these measurements are taken into account. The difference of the 1:1-complex of (R,R)-**2** over (S,S)-**2** by **1** at 300 K extracted from the chemical shift fitting is about $3.3\,\mathrm{kJ\,mol^{-1}}$ in favor of (R,R)-**2** (calculated as difference $\Delta\Delta G$ of the individual values ΔG_3 in table S23 in the SI). This matches the difference derived from the STD amplifications very well, but can be considered to be even more precise, as chemical shifts are more sensitive reporters on changes in the environment. On the other hand, the binding of (S,S)-**2** to the oligomers (modelled as dimer P_2) is favored by approximately $2.6\,\mathrm{kJ\,mol^{-1}}$ ($\Delta\Delta G_4$ from table S23).

Thus, we found that the self-association of peptide **1** is an important aspect in the recognition and binding of the two enantiomers and that the different enantiomers show different affinities to either monomer of **1**(valid for (R,R)-**2**) or aggregate of **1**(valid for (S,S)-**2**). This confirms the finding that selectivity of the kinetic resolution decreases at higher concentrations of **1**.

Catalytic Rate of Acetylation

So far the interactions between **1** and **2** have been investigated under nearly catalytical concentrations, but without the presence of the acetylating agent acetic anhydride (Ac_2O). We concluded from the above sections that peptide **1** displays molecular recognition even if no acetic anhydride is present. Hence, to examine the molecular interactions under reaction conditions, we performed four reactions with the two enantiomers of **2** by following the conversion of the acylation with time-resolved NMR spectroscopy. While initial concentrations of all compounds and temperature were kept constant, two reactions were sampled and quenched from stirred vessels and the other two reactions were performed without additional mixing in NMR tubes.

Figure 6 shows the resulting time-conversion-profiles of the acylations. Both reactions of (R,R)-**2** are almost complete after 5 h. In contrast, in the acylations of (S,S)-**2** approximately 10 % of starting material is left after 120 h.

In order to be able to perform a quantitative analysis of the catalyst-substrate interactions at play, a detailed consideration of the reaction mechanism is necessary. Two scenarios are conceivable, one in which the peptide is acetylated first (depicted in Scheme 2) and one in which the complex formation between **1** and **2** precedes acylation (discussed in the SI, section 9). Apart from the experimental evidence discussed below, we chose to propose the one depicted to be operative based on literature evidence: In the generally accepted mechanism for acylations the peptide catalyst acts as Lewis base that is acylated in the initial step.[63–67] The molecular recognition must then be performed by the acylated catalyst, which can be modelled with the substrate ap-

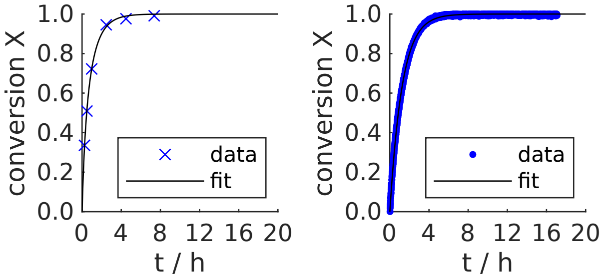

(a) (R,R)-**2**, stirred (b) (R,R)-**2**, static

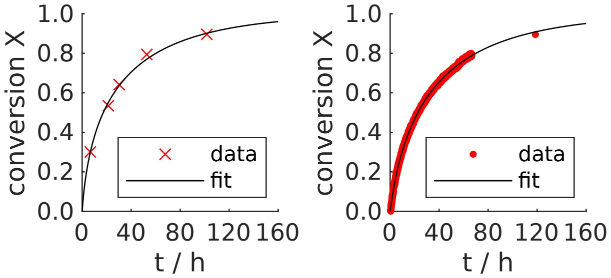

(c) (S,S)-**2**, stirred (d) (S,S)-**2**, static

Figure 6: Conversion versus time of both enantiomers of **2** during catalysis with 2 mol% **1** at 0 °C. Solutions in (a) and (c) have been stirred, while (b) and (d) show the reactions conducted in NMR tubes without additional mixing. The solid lines are the corresponding fits by numerically solving a set of differential equations derived from the catalytic cycle (Scheme 2). The corresponding rate and equilibrium constants were fitted to the data. For plot (d) an additional single point measurement was performed after the original measurement was completed. As can be seen any decreased mass transport in the NMR tube[26] seems not to interfere significantly with reaction progress.

proaching in a reversible step. Finally, the acyl group is transferred from the catalyst onto the substrate and the catalyst is regenerated.

Literature evidence stems *inter alia* from concentration dependent reaction rate measurements with a similar non-chiral catalyst (*N*,*N*-dimethyl-4-aminopyridine, DMAP), which revealed a first-order rate dependency in each, catalyst as well as alcohol (here cyclohexanol), and acetic anhydride (total reaction order 3).[68] Acetate is likely the base relevant for the deprotonation in the final step,[68] as catalysis progresses in absence of an auxiliary base.[13,69] Furthermore, the basicity of acetate and imidazole derivatives is inverted in non-polar organic solvents relative to water.[70–76] Thus acetate is more basic than imidazole, ruling out major contributions of the catalyst acting as Brønsted base, which would favor the alternative mechanism.

The stabilization of ions in general is unfavorable in non-polar organic solvents,[77] thus the concentration of ionic species appears to be low. Nevertheless, the acetylated peptide (PAc^+) was detected NMR spectroscopically in toluene, at high peptide concentration and an excess of acetic anhydride.[78]

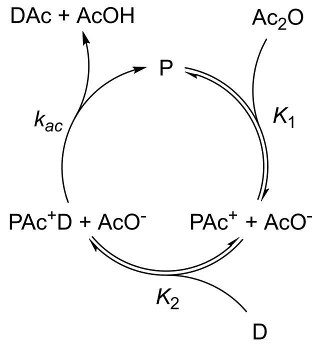

Scheme 2: Schematic catalytic cycle, in which the peptide catalyst P is acetylated in the first step. Then, the diol (D) forms a complex with the acetylated intermediate (PAc^+). The formation of the monoacetylated diol (DAc), as the final step, is irreversible and slow compared to the preceding two equilibrium steps.

Finally, a primary inverse kinetic isotope effect observed in a similar catalytic system (DMAP, *tert*-butanol, Ac_2O) has been associated with the presence of at least one preequilibrium prior to the acyl transfer.[79]

For the quantitative evaluation of our reaction monitoring results (*i.e.*, time dependent concentrations of the respective species), differential rate equations are established for the catalytic cycle proposed in Scheme 2, which are solved numerically for different equilibrium and rate constants.

For this analysis we assume that the equilibria are established faster than the reaction progresses, which makes the acyl transfer step rate-determining.[68] That the differential equations derived from Scheme 2 are a reasonable assumption for the description of catalysis by peptide **1** and that this mechanism is thus the more likely one, is supported by several results from fitting rate and equilibrium constants to the data: Varying the constants yield fit solutions, in which all reactions exhibit the same equilibrium constant for the first step (K_1). This is a necessary outcome for the validity of the catalytic cycle as this step is independent of the diol used. The Gibbs energy for the initial step is in the range of $+5.5\,\mathrm{kJ\,mol^{-1}}$ to $+7.4\,\mathrm{kJ\,mol^{-1}}$ and thus explains the experimental findings, that a huge excess (approx. 500[13,14]) of acetic anhydride with respect to the catalyst must be present to generate PAc^+ albeit in low concentrations. The next step (K_2) depends on the diol used. In terms of Gibbs energy the formation of PAc^+D is $-9.2\,\mathrm{kJ\,mol^{-1}}$ for (R,R)-**2** and $-6.5\,\mathrm{kJ\,mol^{-1}}$ for (S,S)-**2**, and thus the peptide favors (R,R)-**2** by around $3\,\mathrm{kJ\,mol^{-1}}$. This is nearly identical to the energetic difference determined under non-reaction conditions by STD and chemical shift analysis (*vide supra*). The molecular recognition of (R,R)-**2** by peptide **1** is thus only affected to a minor extent by whether the catalyst is acylated or not. Finally, the rate of acyl transfer (k_{ac}) for (R,R)-**2** is an order of magnitude faster than for (S,S)-**2**, which could indicate that the structure or dynamics in PAc$^+$D is more favorable for the acyl transfer in the case of (R,R)-**2**.

The selectivities determined for the acetylations with and without additional mixing are 63 and 55, respectively. Both values are in excellent agreement with the previously determined selectivities ($s > 50$).[13] When doing the same kind of analysis for the alternative scenario (first formation of PD, followed by acylation) unreasonable values are obtained (see SI (section 9)).

In summary, this confirms that the catalytic cycle depicted in Scheme 2 is consistent with literature evidence and experimental data, and thus is the more likely scenario.

Conclusions

We extensively studied a peptide catalyzed kinetic resolution of *trans*-cyclohexane-1,2-diol by NMR spectroscopy in order to decipher the decisive interactions at play. We successfully applied STD, diffusion, and chemical shift analysis – techniques mostly known from protein binding studies, to an interacting system of small organic compounds. All investigated compounds showed concentration-dependent behavior of NMR observables indicating self-association. This asked for an in-depth analysis of the individual compounds before mixtures could be prepared. The investigation of the tetrapeptide revealed self-association, which was analyzed in detail with diffusion coefficients, chemical shift analysis, and temperature coefficients. Thus, all NMR observables of the peptide – and most probably also of other organocatalytic systems – must be viewed in the context of self-association, which has rarely been done in the past.

At higher temperatures and the concentrations typically employed in catalytic reactions, the monomeric peptide species dominates, while the equilibrium moves towards higher self-associates/complexes at low temperatures and/or higher concentrations.

The interactions between tetrapeptide **1** and the two enantiomers of **2** can be appropriately described by an equilibrium model developed for the chemical shift analysis, yielding concentration profiles for the monomeric species as well as the transiently populated higher associates and complexes. The mixtures of tetrapeptide **1** with the two enantiomers of **2** behave differently: (R,R)-**2** shows the qualitatively and quantitatively stronger interactions. Thus the more strongly binding enantiomer is also the faster reacting enantiomer.

Interestingly, there is a further difference between the two enantiomers of **2**: While (R,R)-**2** favors the monomeric tetrapeptide, (S,S)-**2** has a higher affinity towards oligomeric species. If one could regulate this behaviour by chemical modification, catalysts with even higher selectivity are conceivable.

Finally, the reaction rate determined under catalytic conditions (thus also in the presence of the acetylating agent) can be fitted with a reasonable catalytic cycle, reproducing the experimental selectivities reported earlier. The preference of tetrapeptide **1** for (R,R)-**2** extracted at reaction conditions from this kinetic analysis fits well to the previously determined values from chemical shift analysis, showing the complementarity of the employed methods.

As the results show, taking into account self-association should play a greater role in catalyst design in the future. Even without the extensive quantitative analysis performed here, qualitative investigations of the concentration dependence of catalyst selectivities and chemical shifts should be carried out to assess the impact of catalyst self-association. Interestingly, just looking at the spectra obtained from saturation transfer difference measurements already revealed a preference of (R,R)-**2**) over (S,S)-**2**). More importantly, the quantitative analysis yielded approximately the same difference in energy ($3\,\mathrm{kJ\,mol^{-1}}$ in favor of (R,R)-**2**) as was obtained from reaction monitoring and the more extensive chemical shift fitting despite the fact that the stochiometry of the complex is not accessible from STD. This might indicate that STD can potentially be used in catalyst screening in the future.

Acknowledgement J. Nowag, M. Brauser and C. M. Thiele thank the Deutsche Forschungsgesellschaft (TH1115/12-1) for financial support. M. Brauser acknowledges funding by the Dr. Hans Messer Foundation. The authors would like to thank S. Zurmühl for her contributions to the peptide temperature coefficients.

Supporting Information Available

Additional experimental procedures, materials, and methods, compound characterization, NMR spectra (PDF)

References

(1) Aukland, M. H.; List, B. *Pure Appl. Chem.* **2021**, *93*, 1371–1381.

(2) Hughes, D. L. *Org. Process Res. Dev.* **2018**, *22*, 574–584.

(3) Jacobsen, E. N.; Pfaltz, A.; Yamamoto, H. *Comprehensive asymmetric catalysis*, 1st ed.; Springer: London, 1999.

(4) Wennemers, H. *Chem. Commun.* **2011**, *47*, 12036–12041.

(5) Davie, E. A. C.; Mennen, S. M.; Xu, Y.; Miller, S. J. *Chem. Rev.* **2007**, *107*, 5759–5812.

(6) Metrano, A. J.; Chinn, A. J.; Shugrue, C. R.; Stone, E. A.; Kim, B.; Miller, S. J. *Chem. Rev.* **2020**, *120*, 11479–11615.

(7) Amblard, M.; Fehrentz, J.-A.; Martinez, J.; Subra, G. *Mol. Biotechnol.* **2006**, *33*, 239–254.

(8) Masui, H.; Fuse, S. *Org. Process Res. Dev.* **2022**, *26*, 1751–1765.

(9) Narancic, T.; Almahboub, S. A.; O'Connor, K. E. *World J. Microbiol. Biotechnol.* **2019**, *35*, 67.

(10) Sharma, A.; Kumar, A.; de la Torre, B. G.; Albericio, F. *Chem. Rev.* **2022**, *122*, 13516–13546.

(11) Breslow, R. *J. Biol. Chem.* **2009**, *284*, 1337–1342.

(12) Dabkowska, K.; Szewczyk, K. W. *Biochem. Eng. J.* **2009**, *46*, 147–153.

(13) (a) Müller, C. E.; Wanka, L.; Jewell, K.; Schreiner, P. R. *Angew. Chem. Int. Ed.* **2008**, *47*, 6180–6183; (b) Müller, C. E.; Wanka, L.; Jewell, K.; Schreiner, P. R. *Angew. Chem.* **2008**, *120*, 6275–6278.

(14) Müller, C. E.; Zell, D.; Hrdina, R.; Wende, R. C.; Wanka, L.; Schuler, S. M. M.; Schreiner, P. R. *J. Org. Chem.* **2013**, *78*, 8465–8484.

(15) Wanka, L.; Cabrele, C.; Vanejews, M.; Schreiner, P. R. *Eur. J. Org. Chem.* **2007**, *2007*, 1474–1490.

(16) Jarvo, E. R.; Copeland, G. T.; Papaioannou, N.; Bonitatebus, P. J.; Miller, S. J. *J. Am. Chem. Soc.* **1999**, *121*, 11638–11643.

(17) Jarvo, E. R.; Vasbinder, M. M.; Miller, S. J. *Tetrahedron* **2000**, *56*, 9773–9779.

(18) Griswold, K. S.; Miller, S. J. *Tetrahedron* **2003**, *59*, 8869–8875.

(19) Rho, H. S.; Oh, S. H.; Lee, J. W.; Lee, J. Y.; Chin, J.; Song, C. E. *Chem. Commun.* **2008**, 1208–1210.

(20) Jang, H. B.; Rho, H. S.; Oh, J. S.; Nam, E. H.; Park, S. E.; Bae, H. Y.; Song, C. E. *Org. Biomol. Chem.* **2010**, *8*, 3918–3922.

(21) (a) Mitra, R.; Zhu, H.; Grimme, S.; Niemeyer, J. *Angew. Chem. Int. Ed.* **2017**, *56*, 11456–11459; (b) Mitra, R.; Zhu, H.; Grimme, S.; Niemeyer, J. *Angew. Chem.* **2017**, *129*, 11614–11617.

(22) Jansen, D.; Gramüller, J.; Niemeyer, F.; Schaller, T.; Letzel, M. C.; Grimme, S.; Zhu, H.; Gschwind, R. M.; Niemeyer, J. *Chem. Sci.* **2020**, *11*, 4381–4390.

(23) Kagan, H. B.; Fiaud, J. C. *Top. Stereochem.* **1988**, *18*, 249–330.

(24) Poli, R. *Comments Inorg. Chem.* **2009**, *30*, 177–228.

(25) Foley, D. A.; Bez, E.; Codina, A.; Colson, K. L.; Fey, M.; Krull, R.; Piroli, D.; Zell, M. T.; Marquez, B. L. *Anal. Chem.* **2014**, *86*, 12008–12013.

(26) Foley, D. A.; Dunn, A. L.; Zell, M. T. *Magn. Reson. Chem.* **2016**, *54*, 451–456.

(27) Ben-Tal, Y.; Boaler, P. J.; Dale, H. J.; Dooley, R. E.; Fohn, N. A.; Gao, Y.; García-Domínguez, A.; Grant, K. M.; Hall, A. M.; Hayes, H. L.; Kucharski, M. M.; Wei, R.; Lloyd-Jones, G. C. *Prog. Nucl. Magn. Reson. Spectrosc.* **2022**, *129*, 28–106.

(28) Lepre, C. A.; Moore, J. M.; Peng, J. W. *Chem. Rev.* **2004**, *104*, 3641–3676.

(29) Gossert, A. D.; Jahnke, W. *Prog. Nucl. Magn. Reson. Spectrosc.* **2016**, *97*, 82–125.

(30) Thordarson, P. *Chem. Soc. Rev.* **2011**, *40*, 1305–1323.

(31) (a) Procházková, E.; Kolmer, A.; Ilgen, J.; Schwab, M.; Kaltschnee, L.; Fredersdorf, M.; Schmidts, V.; Wende, R. C.; Schreiner, P. R.; Thiele, C. M. *Angew. Chem. Int. Ed.* **2016**, *55*, 15754–15759; (b) Procházková, E.; Kolmer, A.; Ilgen, J.; Schwab, M.; Kaltschnee, L.; Fredersdorf, M.; Schmidts, V.; Wende, R. C.; Schreiner, P. R.; Thiele, C. M. *Angew. Chem.* **2016**, *128*, 15986–15991.

(32) Griffiths, V.; Socrates, G. *J. Mol. Spectrosc.* **1966**, *21*, 302–309.

(33) Fletcher, A. N.; Heller, C. A. *J. Phys. Chem.* **1967**, *71*, 3742–3756.

(34) Førland, G. M.; Libnau, F. O.; Kvalheim, O. M.; Høiland, H. *Appl. Spectrosc.* **1996**, *50*, 1264–1272.

(35) Nodland, E. *Appl. Spectrosc.* **2000**, *54*, 1339–1349.

(36) Lopes Jesus, A.; Redinha, J. *J. Mol. Struct.* **2014**, *1067*, 104–111.

(37) (a) Schneider, H.-J. *Angew. Chem. Int. Ed.* **2009**, *48*, 3924–3977; (b) Schneider, H.-J. *Angew. Chem.* **2009**, *121*, 3982–4036.

(38) Knowles, R. R.; Jacobsen, E. N. *Proc. Natl. Acad. Sci.* **2010**, *107*, 20678–20685.

(39) Cierpicki, T.; Otlewski, J. *J. Biomol. NMR* **2001**, *21*, 249–261.

(40) Alex, A.; Millan, D. S.; Perez, M.; Wakenhut, F.; Whitlock, G. A. *Med. Chem. Commun.* **2011**, *2*, 669–674.

(41) Peintner, S.; Erdélyi, M. *Chem. Eur. J.* **2022**, *28*, e202103559.

(42) Lucas, L. H.; Larive, C. K. *Concepts Magn. Reson.* **2004**, *20A*, 24–41.

(43) Price, W. S. *eMagRes* **2002**, *9*, 367–374.

(44) (a) Mayer, M.; Meyer, B. *Angew. Chem. Int. Ed.* **1999**, *38*, 1784–1788; (b) Mayer, M.; Meyer, B. *Angew. Chem.* **1999**, *111*, 1902–1906.

(45) Angulo, J.; Enríquez-Navas, P. M.; Nieto, P. M. *Chem. Eur. J.* **2010**, *16*, 7803–7812.

(46) Kolmer, A. Aufklärung von Struktur-Reaktivitäts-Beziehungen komplexer organischer Moleküle mit moderner NMR-Spektroskopie. PhD-Thesis, Technische Universität Darmstadt, Darmstadt, 2015.

(47) Seitz, A.; Wende, R. C.; Roesner, E.; Niedek, D.; Topp, C.; Colgan, A. C.; McGarrigle, E. M.; Schreiner, P. R. *J. Org. Chem.* **2021**, *86*, 3907–3922.

(48) Beechem, J. M. *Methods Enzymol.* **1992**, *210*, 37–54.

(49) Martin, R. B. *Chem. Rev.* **1996**, *96*, 3043–3064.

(50) Price, W. S.; Tsuchiya, F.; Arata, Y. *J. Am. Chem. Soc.* **1999**, *121*, 11503–11512.

(51) Jerschow, A.; Müller, N. *J. Magn. Reson.* **1997**, *125*, 372–375.

(52) Neufeld, R.; Stalke, D. *Chem. Sci.* **2015**, *6*, 3354–

3364.

(53) Ajitha, M.; Huang, K.-W. *Synthesis* **2016**, *48*, 3449–3458.

(54) Cook, J. L.; Hunter, C. A.; Low, C. M. R.; Perez-Velasco, A.; Vinter, J. G. *Angew. Chem. Int. Ed.* **2007**, *46*, 3706–3709.

(55) Fujii, Y.; Yamada, H.; Mizuta, M. *J. Phys. Chem.* **1988**, *92*, 6768–6772.

(56) Shirota, H.; Fukuda, T.; Kato, T. *J. Phys. Chem.* **2013**, *117*, 16196–16205.

(57) Haynes, W. M., Lide, D. R., Eds. *CRC Handbook of Chemistry and Physics*, 96th ed.; CRC Press: Boca Raton, Fla., 2015.

(58) Huang, H.; Milojevic, J.; Melacini, G. *J. Phys. Chem.* **2008**, *112*, 5795–5802.

(59) Webb, J. E. A.; Crossley, M. J.; Turner, P.; Thordarson, P. *J. Am. Chem. Soc.* **2007**, *129*, 7155–7162.

(60) Job, P. *Ann. Chim.* **1928**, *9*, 113–203.

(61) (a) Renny, J. S.; Tomasevich, L. L.; Tallmadge, E. H.; Collum, D. B. *Angew. Chem. Int. Ed.* **2013**, *52*, 11998–12013; (b) Renny, J. S.; Tomasevich, L. L.; Tallmadge, E. H.; Collum, D. B. *Angew. Chem.* **2013**, *125*, 12218–12234.

(62) Hibbert, D. B.; Thordarson, P. *Chem. Commun.* **2016**, *52*, 12792–12805.

(63) Lutz, V.; Glatthaar, J.; Würtele, C.; Serafin, M.; Hausmann, H.; Schreiner, P. R. *Chem. Eur. J.* **2009**, *15*, 8548–8557.

(64) Furuta, T.; Kawabata, T. In *Asymmetric Organocatalysis 1: Lewis Base and Acid Catalysts*; List, B., Ed.; Georg Thieme Verlag: Stuttgart, 2012; pp 497–546.

(65) Smith, A. D.; Woods, P. A. In *Asymmetric Organocatalysis 1: Lewis Base and Acid Catalysts*; List, B., Ed.; Georg Thieme Verlag: Stuttgart, 2012; pp 547–590.

(66) Liao, R.-Z.; Santoro, S.; Gotsev, M.; Marcelli, T.; Himo, F. *ACS Catal.* **2016**, *6*, 1165–1171.

(67) Metrano, A. J.; Miller, S. J. *Acc. Chem. Res.* **2019**, *52*, 199–215.

(68) Xu, S.; Held, I.; Kempf, B.; Mayr, H.; Steglich, W.; Zipse, H. *Chem. Eur. J.* **2005**, *11*, 4751–4757.

(69) Lamaty, G.; Mary, F.; Roque, J. P. *J. Chim. Phys. Phys.-Chim. Biol.* **1991**, *88*, 1793–1810.

(70) Bordwell, F. G. *Acc. Chem. Res.* **1988**, *21*, 456–463.

(71) Benoit, R. L.; Boulet, D.; Séguin, L.; Fréchette, M. *Can. J. Chem.* **1985**, *63*, 1228–1232.

(72) Klicić, J. J.; Friesner, R. A.; Liu, S.-Y.; Guida, W. C. *J. Phys. Chem.* **2002**, *106*, 1327–1335.

(73) Kolthoff, I. M.; Chantooni, M. K.; Bhowmik, S. *J. Am. Chem. Soc.* **1968**, *90*, 23–28.

(74) Cox, B. G. *Org. Process Res. Dev.* **2015**, *19*, 1800–1808.

(75) Nurminen, E. J.; Mattinen, J. K.; Lönnberg, H. *J. Chem. Soc., Perkin Trans. 2* **2001**, 2159–2165.

(76) Pandit, N. K.; Connors, K. A. *J. Pharm. Sci.* **1982**, *71*, 485–491.

(77) (a) Bülow, M.; Ascani, M.; Held, C. *Fluid Phase Equilib.* **2021**, *535*, 112967; (b) Bülow, M.; Ascani, M.; Held, C. *Fluid Phase Equilib.* **2021**, *537*, 112989.

(78) Brauser, M.; Heymann, T.; Thiele, C. M. *Molecules* **2022**, *27*, 6351.

(79) Guibe-Jampel, E.; Le Corre, G.; Wakselman, M. *Tetrahedron Lett.* **1979**, *20*, 1157–1160.

TOC Graphic

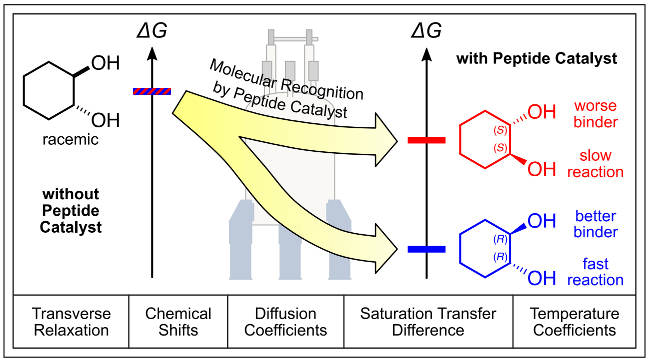
ΔG
ΔG
OH
OH
racemic
without Peptide Catalyst
Molecular Recognition by Peptide Catalyst
with Peptide Catalyst
(S)
(S)
OH
OH
worse binder
slow reaction
(R)
(R)
OH
OH
better binder
fast reaction
Transverse Relaxation
Chemical Shifts
Diffusion Coefficients
Saturation Transfer Difference
Temperature Coefficients

Quantifying Intermolecular Interactions in Asymmetric Peptide Organocatalysis as a Key Towards Understanding Selectivity

Jens Nowag,¶ Matthias Brauser,¶ Raffael C. Wende,§ Peter R. Schreiner,§ and Christina M. Thiele*,¶

¶*Clemens-Schöpf-Institut für Organische Chemie und Biochemie, Technische Universität Darmstadt, Peter-Grünberg-Straße 16, D-64287 Darmstadt, Germany*

§*Institute of Organic Chemistry, Justus Liebig University, Heinrich-Buff-Ring 17, D-35392 Giessen, Germany*

E-mail: cthiele@thielelab.de

Supporting Information

1 Compound Structures and Chemical Shift Assignment

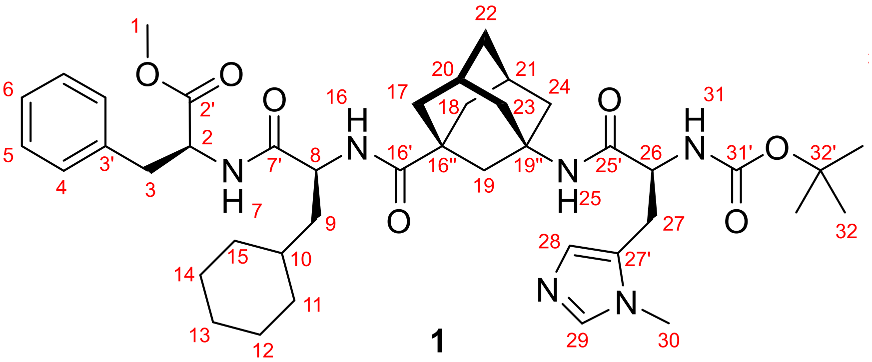

1

Figure S1: Structure and numbering of tetrapeptide Boc-L-(π-Me)-His-^{A}Gly-L-Cha-L-Phe-OMe **1**.

Table S1: Proton, carbon and nitrogen chemical shift assignment of 5.02 mM **1** at 300 K in toluene-d_8 (sample jn-123). Deviating values may be observed at other concentrations and temperatures.[1] Chemical shifts are referenced to the ^{1}H residual solvent signal ($\delta_H = 2.08$ ppm) via Ξ-referencing for all nuclei.[2] Nitrogen chemical shifts are reported relative to liquid ammonia ($\delta_N(NH_3) \approx 0$).

Position	Affix	δ_H / ppm	δ_C / ppm	δ_N / ppm	Position	Affix	δ_H / ppm	δ_C / ppm	δ_N / ppm
1		3.30	51.2		17^b	a	1.83	38.0	
2’			171.5			b	1.68		
2		4.95	53.6		18^b	a	1.80	38.2	
3	a	3.13	37.8			b	1.65		
	b	3.01			19	a	2.11	42.5	
3’			136.6			b	2.01		
4		7.15	129.3		19’			52.0	
5		7.18	128.4		20^b		1.97	29.4	
6		7.09	126.8		21^b		1.96	29.4	
7		7.62		115.0	22	a	1.47	35.2	
7’			172.4			b	1.38		
8		4.77	51.0		23^b	a	1.98	40.1	
9	a	1.83	39.6			b	1.93		
	b	1.66			24^b	a	2.00	40.2	
10		1.44	34.3			b	1.86		
11^a	ax	0.90	33.4		25		6.61		76.5
	eq	1.75			25’			169.7	
12^a	ax	1.27	26.3		26		4.41	54.6	
	eq	1.67			27	a	2.85	27.4	
13	ax	1.12	26.5			b	2.81		
	eq	1.61			27’			127.3	160.8
14^a	ax	1.23	26.3		28		7.01	128.2	256.5
	eq	1.66			29		7.17	137.7	
15^a	ax	0.83	32.8		30		2.99	30.3	
	eq	1.77			31		5.77		88.5
16		6.73		113.2	31’			155.3	
16’			176.3		32’			79.0	
16”			42.5		32		1.40	28.0	

^{a} assignments of diastereotopic resonances 11 and 12 may be switched with 15 and 14, respectively

^{b} assignments of diastereotopic resonances 17, 20 and 23 may be switched with 18, 21 and 24, respectively

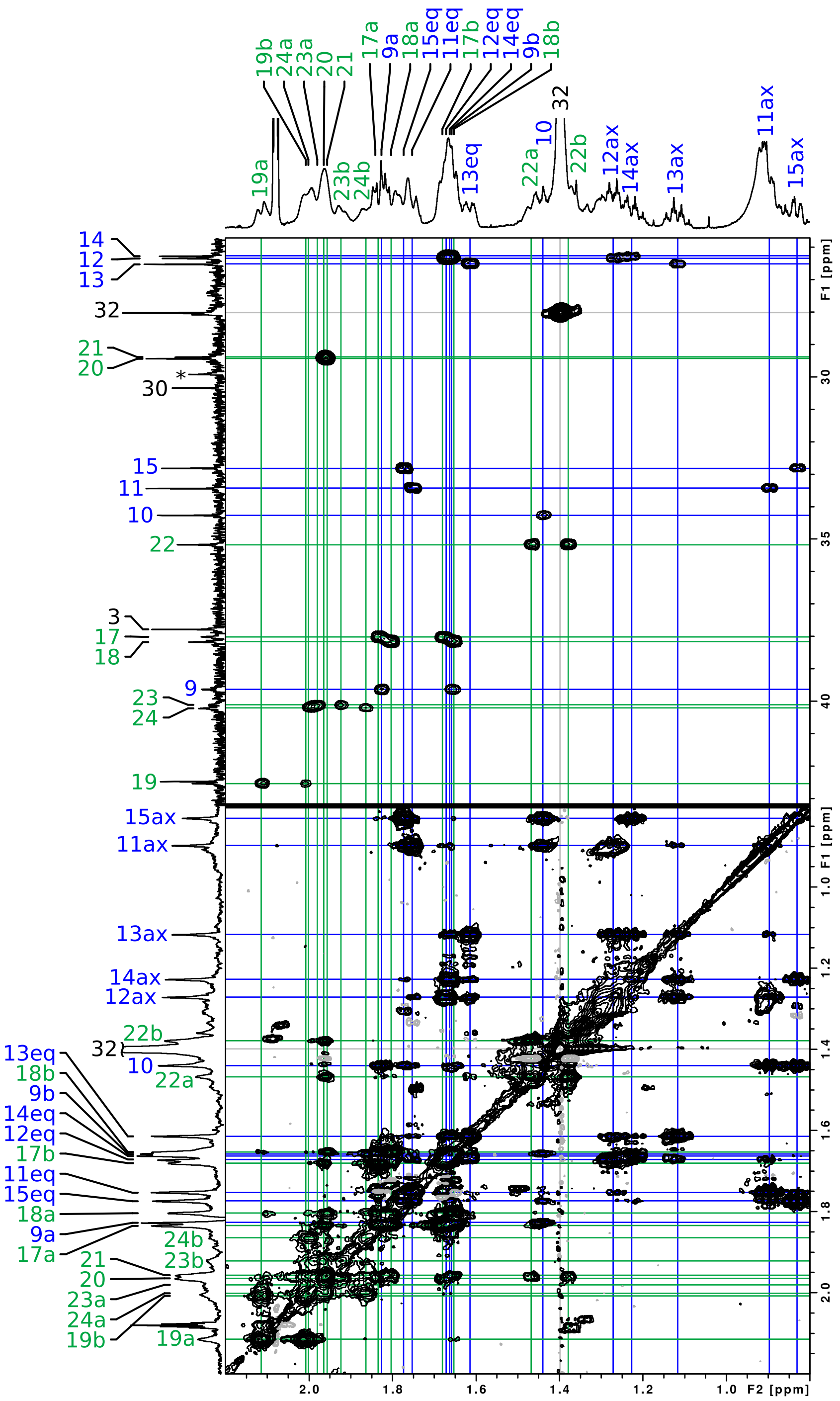

Figure S2: Two 2D-Spectra in the aliphatic region with assignment of **1** at 700 MHz proton resonance frequency (sample jn-123). Top: ^{1}H-^{13}C HSQC. Bottom: ^{1}H-^{1}H F1-PSYCHE-CLIP-COSY. Top trace: conventional ^{1}H spectrum. Upper left trace: conventional ^{13}C spectrum. Lower left trace: homodecoupled ^{1}H PSYCHE spectrum. Experimental details are given in section 2.2. The spin system of the adamantyl moiety is color coded in green, while the cyclohexyl group is color coded in blue.

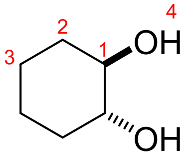

rac-**2**

Figure S3: Structure and numbering of *trans*-cyclohexane-1,2-diol **2**.

Table S2: Proton and carbon chemical shift assignment of 22.37 mM *rac*-**2** at 300 K in toluene-d_8 (sample jn-140-1). Chemical shifts are referenced to the ^{1}H residual solvent signal ($\delta_H = 2.08$ ppm) via Ξ-referencing for all nuclei.[2]

Position	Affix	δ_H / ppm	δ_C / ppm
1		3.03	75.4
2	ax	1.04	32.7
	eq	1.72	
3	ax	0.95	24.2
	eq	1.38	
4		1.89	

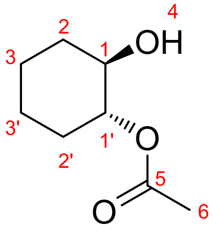

(*R*,*R*)-**3**

Figure S4: Structure and numbering of (*R*,*R*)-cyclohexane-1,2-diol monoacetate **3**.

Table S3: Proton and carbon chemical shift assignment of ∼2.3 mM (*R*,*R*)-**3** at 273.2 K in toluene-d_8 (reaction solution jn-146 at ca. 85 % conversion). Assignment performed under reaction conditions in presence of acetic acid. Chemical shifts are referenced to the ^{1}H residual solvent signal ($\delta_H = 2.08$ ppm) via Ξ-referencing for all nuclei.[2]

Position	Affix	δ_H / ppm	δ_C / ppm
1		3.32	72.3
2	ax	1.08	32.9
	eq	1.80	
3	ax	0.87	23.5
	eq	1.32	
4		n.a.[a]	
1'		4.58	77.6
2'	ax	1.06	29.8
	eq	1.89	
3'	ax	0.94	23.7
	eq	1.31	
5			170.1
6		1.67	20.4

[a] The resonance is not observable due to extensive broadening.

Assignments at other temperatures and concentrations can be found in the supplementary material (section 11).

2 Experimental

2.1 NMR Sample Preparation

NMR samples have been prepared either directly in an NMR tube or as combined mixture of different stock solutions. toluene-d_8, dichloromethane-d_2, acetone-d_6, methanol-d_4, and (S,S)-cyclohexane-1,2-diol (**2**) have been obtained from Sigma Aldrich. Both (R,R)-**2** and tetrapeptide **1** have been synthesized as reported previously.[3] The chemicals have been used without any further purification.

In the following Tables S4 to S9 the indices P, D, and sol stand for masses m of peptide, diol, and solvent, respectively. These tables include only the samples used for the peptide-diol interaction studies. Information on other samples can be found in section 9. The concentrations of peptide ($[\mathrm{P}]_t$) and diol ($[\mathrm{D}]_t$) are denoted with a t to indicate that the total concentration is meant (irrespective of aggregation state). The ratio of both concentrations is given by $r = \frac{[\mathrm{D}]_t}{[\mathrm{P}]_t}$. The molar fraction of the diol x_D is calculated via $\frac{[\mathrm{D}]_t}{[\mathrm{P}]_t+[\mathrm{D}]_t}$. For the experimental details of the reaction monitoring see section 9.2.

2.1.1 Samples Containing only *rac*-*trans*-Cyclohexane-1,2-diol

Table S4: Final concentrations of the samples containing *rac*-*trans*-cyclohexane-1,2-diol (*rac*-**2**). The concentration varied is color coded.

m_P / mg	m_D / mg	m_sol / mg	$[\mathrm{P}]_t$ / mM	$[\mathrm{D}]_t$ / mM	r	x_D	sample
0.00	0.05	428.37	0.00	0.87	∞	1.0000	jn-140-4
0.00	0.21	633.70	0.00	2.70	∞	1.0000	jn-140-3
0.00	0.23	473.40	0.00	3.91	∞	1.0000	jn-113
0.00	0.74	958.48	0.00	6.28	∞	1.0000	jn-152-5
0.00	0.36	373.00	0.00	7.89	∞	1.0000	jn-143
0.00	0.74	650.45	0.00	9.26	∞	1.0000	jn-152-4
0.00	0.74	576.01	0.00	10.48	∞	1.0000	jn-152-3
0.00	0.63	420.86	0.00	12.06	∞	1.0000	jn-140-2
0.00	0.74	449.64	0.00	13.43	∞	1.0000	jn-152-2
0.00	0.64	323.69	0.00	15.96	∞	1.0000	jn-142
0.00	0.74	349.79	0.00	17.24	∞	1.0000	jn-152-1
0.00	1.26	456.35	0.00	22.37	∞	1.0000	jn-140-1
0.00	1.92	667.36	0.00	23.36	∞	1.0000	jn-101

2.1.2 Samples Containing only Tetrapeptide

Table S5: Final concentrations of the samples containing only tetrapeptide **1** in toluene-d_8. The concentration varied is color coded.

m_P / mg	m_D / mg	m_sol / mg	$[\mathrm{P}]_t$ / mM	$[\mathrm{D}]_t$ / mM	r	x_D	sample
0.04	0.00	683.76	0.07	0.00	0.00	0.0000	jn-47
0.20	0.00	470.28	0.52	0.00	0.00	0.0000	jn-122
0.22	0.00	471.99	0.57	0.00	0.00	0.0000	jn-44
1.04	0.00	1176.72	1.10	0.00	0.00	0.0000	jn-107-4
0.43	0.00	473.98	1.13	0.00	0.00	0.0000	jn-45
0.95	0.00	523.44	2.25	0.00	0.00	0.0000	jn-46
0.94	0.00	463.32	2.51	0.00	0.00	0.0000	jn-27
1.04	0.00	613.63	3.13	0.00	0.00	0.0000	jn-107-3
1.04	0.00	418.50	4.59	0.00	0.00	0.0000	jn-107-2
1.72	0.00	426.87	5.02	0.00	0.00	0.0000	jn-123
1.04	0.00	332.51	5.78	0.00	0.00	0.0000	jn-107-1
5.39	0.00	715.07	9.34	0.00	0.00	0.0000	jn-102
5.51	0.00	632.61	10.79	0.00	0.00	0.0000	jn-48
7.21	0.00	460.72	19.70	0.00	0.00	0.0000	jn-sz-001
7.54	0.00	468.40	19.94	0.00	0.00	0.0000	jn-49

Table S6: Final concentrations of the samples containing only tetrapeptide **1** in dichloromethane-d_2. The concentration varied is color coded.

m_P / mg	m_D / mg	m_sol / mg	$[\mathrm{P}]_t$ / mM	$[\mathrm{D}]_t$ / mM	r	x_D	sample
1.15	0.00	733.5	2.81	0.00	0.00	0.0000	mkb-19
7.8	0.00	1165.3	12.06	0.00	0.00	0.0000	mkb-18-2
7.8	0.00	352.1	40.55	0.00	0.00	0.0000	mkb-18-1

Table S7: Final concentrations of the samples containing only tetrapeptide **1** in acetone-d_6. The concentration varied is color coded.

m_P / mg	m_D / mg	m_sol / mg	$[\mathrm{P}]_t$ / mM	$[\mathrm{D}]_t$ / mM	r	x_D	sample
1.09	0.00	260.0	4.84	0.00	0.00	0.0000	mkb-21
7.6	0.00	305.1	29.27	0.00	0.00	0.0000	mkb-20-2
7.6	0.00	231.0	38.98	0.00	0.00	0.0000	mkb-20-1

2.1.3 Mixtures of Tetrapeptide with (*R*,*R*)-Cyclohexane-1,2-diol

Table S8: Final concentrations of the samples containing **1** and (*R*,*R*)-**2** in toluene-d_8. The concentrations varied are color coded.

m_P / mg	m_D / mg	m_sol / mg	$[\mathrm{P}]_t$ / mM	$[\mathrm{D}]_t$ / mM	r	x_D	sample
1.27	0.02	626.70	2.51	0.23	0.09	0.0839	jn-28
1.19	0.04	586.39	2.51	0.48	0.19	0.1605	jn-29
1.01	0.04	500.80	2.50	0.71	0.28	0.2212	jn-30
0.96	0.06	475.16	2.50	0.94	0.38	0.2733	jn-31
0.95	0.07	471.65	2.50	1.19	0.48	0.3225	jn-32
1.00	0.09	496.41	2.50	1.52	0.61	0.3781	jn-33
0.99	0.10	487.93	2.50	1.73	0.69	0.4090	jn-34
0.96	0.12	476.83	2.50	1.99	0.80	0.4432	jn-35
0.95	0.13	468.51	2.50	2.25	0.90	0.4737	jn-36
0.95	0.14	470.63	2.50	2.48	0.99	0.4980	jn-37
1.01	0.23	502.38	2.50	3.78	1.51	0.6019	jn-38
0.95	0.29	469.93	2.49	4.94	1.98	0.6649	jn-39
1.04	0.48	516.43	2.49	7.55	3.03	0.7520	jn-40
0.96	0.60	476.62	2.48	10.13	4.08	0.8033	jn-41
0.93	0.87	468.79	2.47	15.10	6.11	0.8594	jn-42
0.93	1.17	470.72	2.45	20.11	8.21	0.8914	jn-43
7.18	0.04	464.45	19.14	0.78	0.04	0.0392	jn-50
6.72	0.11	463.29	17.96	1.94	0.11	0.0975	jn-51
6.34	0.19	471.39	16.65	3.22	0.19	0.1621	jn-52
6.05	0.23	472.32	15.85	4.00	0.25	0.2015	jn-53
5.62	0.29	468.92	14.83	5.00	0.34	0.2521	jn-54
5.23	0.33	463.34	13.96	5.85	0.42	0.2953	jn-55
4.86	0.39	462.07	13.02	6.78	0.52	0.3424	jn-56
4.49	0.45	463.79	11.98	7.79	0.65	0.3940	jn-57
4.14	0.51	466.75	10.97	8.79	0.80	0.4448	jn-58
3.68	0.56	462.64	9.84	9.89	1.01	0.5013	jn-59
3.34	0.62	464.93	8.89	10.82	1.22	0.5490	jn-60
2.95	0.68	466.30	7.84	11.85	1.51	0.6018	jn-61
2.65	0.73	466.68	7.04	12.64	1.80	0.6423	jn-62
2.23	0.79	466.83	5.92	13.73	2.32	0.6987	jn-63
1.88	0.84	466.37	5.00	14.63	2.93	0.7453	jn-64
1.51	0.90	468.12	3.98	15.63	3.93	0.7970	jn-65
1.14	0.96	469.45	3.00	16.59	5.53	0.8469	jn-66
0.19	0.11	470.45	0.49	1.94	3.96	0.7984	jn-108
0.19	0.24	473.54	0.49	4.08	8.33	0.8928	jn-110
0.19	0.42	471.37	0.49	7.16	14.61	0.9359	jn-111
0.19	0.59	470.62	0.49	10.13	20.67	0.9539	jn-112

2.1.4 Mixtures of Tetrapeptide with (*S*,*S*)-Cyclohexane-1,2-diol

Table S9: Final concentrations of the samples containing **1** and (*S*,*S*)-**2** in toluene-d_8. The concentration varied is color coded.

m_P / mg	m_D / mg	m_sol / mg	$[\mathrm{P}]_t$ / mM	$[\mathrm{D}]_t$ / mM	r	x_D	sample
0.94	0.01	468.48	2.47	0.13	0.05	0.0487	jn-68
0.93	0.01	467.12	2.47	0.22	0.09	0.0827	jn-69
0.94	0.02	472.25	2.47	0.38	0.16	0.1342	jn-70
0.94	0.03	472.59	2.47	0.59	0.24	0.1916	jn-71
0.94	0.05	470.15	2.47	0.79	0.32	0.2419	jn-72
0.94	0.07	471.01	2.47	1.18	0.48	0.3230	jn-73
0.93	0.08	467.19	2.47	1.37	0.55	0.3561	jn-74
0.93	0.11	465.27	2.47	1.85	0.75	0.4279	jn-75
0.94	0.14	472.76	2.47	2.36	0.95	0.4884	jn-76
0.95	0.19	477.25	2.47	3.16	1.28	0.5611	jn-77
0.93	0.23	467.60	2.47	3.94	1.60	0.6150	jn-78
0.92	0.34	462.82	2.47	5.93	2.40	0.7061	jn-79
0.93	0.46	466.55	2.47	7.96	3.23	0.7634	jn-80
0.92	0.58	463.79	2.47	10.05	4.08	0.8030	jn-81
0.93	0.82	463.23	2.47	14.18	5.75	0.8519	jn-82
0.93	1.17	468.55	2.46	20.22	8.21	0.8914	jn-83
0.19	0.12	471.70	0.51	1.99	3.89	0.7955	jn-118
0.19	0.23	473.00	0.51	4.02	7.95	0.8883	jn-119
0.19	0.41	471.56	0.51	6.99	13.76	0.9322	jn-120
0.20	0.58	472.71	0.53	9.97	18.85	0.9496	jn-121

2.2 NMR Spectroscopic Experiments

All spectra were recorded without spinning on a 16.4 T (700 MHz ^{1}H frequency) spectrometer (*Bruker* AVANCE III HD, equipped with a QCI cryo probe (^{1}H/^{19}F, ^{31}P, ^{13}C, ^{15}N, ^{2}H) with a 54 G s cm^{-1} z-gradient) including a BCU-II temperature unit. Chemical shifts are reported relative to the residual solvent signals of toluene-d_7 (methyl group), dichloromethane-d_1, and acetone-d_5 (methyl group) at 2.08 ppm, 5.32 ppm and 2.05 ppm, respectively.[4] Experiments with varying temperature are calibrated with a methanol-d_4 (99.8 %D) shift thermometer and standard calibration curve.[5] The VT-gas flow rate for all measurements was set to 535 L h^{-1}. Gradient strengths for the diffusion measurements have been calibrated using the "doped water" standard sample (Z10083) from *Bruker* containing 0.1 % ^{13}CD$_3$OD and 0.1 mg GdCl$_3$ in D$_2$O (99 %D). Prior to all quantitative measurements the 90° proton pulse and the longitudinal relaxation rates (to fulfill recycle delay $\mathrm{D1} \geqslant 5 \cdot T_1$) were determined for each sample. NMR experiments (^{1}H / ^{13}C{^{1}H} / ^{1}H,^{1}H CLIP-COSY[6] / ^{1}H,^{13}C HSQC / ^{1}H,^{13}C HMBC) were used for assignments. For assignments of diol **2** an additional ^{13}C{^{1}H} DEPT-135 experiment was recorded. For assignments of peptide **1** additional experiments (^{1}H PSYCHE[7] / ^{1}H,^{1}H EASY-ROESY[8] / ^{1}H,^{1}H F1-PSYCHE-CLIP-COSY[9] / ^{1}H,^{15}N HSQC / ^{1}H,^{15}N HMBC) were recorded. Interactions between **1** and **2** were probed with ^{1}H chemical shifts, ^{1}H PROJECT,[10] ^{1}H DSTE,[11] and ^{1}H STD.[12] Proton chemical shifts were determined from 1D proton spectra reported at different temperatures. In the crowded regions (aromatic and aliphatic region), aliased HSQC spectra aided in this analysis. As the amide resonances display large temperature-dependent chemical shift differences, occasionally CLIP-COSY[6] spectra have been recorded for the unequivocal assignment of these resonances.

2.2.1 ^{1}H

^{1}H-NMR spectra were recorded with the pulse sequence `zg` from the *Bruker* pulse sequence library. The FIDs received, consisting of 65536 time domain points within a spectral width of 14.1 kHz, were multiplied by an exponential apodization function (0.3 Hz line broadening) prior to Fourier transform without zero-filling. Phase correction was done manually, followed by automatic baseline correction.

2.2.2 ^{13}C{^{1}H}

^{13}C-NMR spectra for assignments were recorded with the pulse sequence `zgpg30` from the *Bruker* pulse sequence library. 1024 scans were acquired with a recycle delay of 2 s. Heteronuclear decoupling was achieved employing the WALTZ-65[13] sequence. The FIDs received, consisting of 65536 time domain points within a spectral width of 41.6 kHz, were zero-filled by a factor of two. The FIDs were multiplied by an exponential apodization function (1 Hz line broadening) prior to Fourier transform. Phase correction was done manually, followed by automatic baseline correction.

2.2.3 ^{13}C{^{1}H} DEPT-135

^{13}C-DEPT spectra for assignments were recorded with the pulse sequence `deptsp135` from the *Bruker* pulse sequence library. 32 scans were acquired with a recycle delay of 2 s. The INEPT delay was optimized for a coupling constant of $^1J_{\mathrm{HC}} = 145$ Hz. Broadband inversion of carbon frequencies was achieved with a 58.7 kHz Chirp composite pulse (`Crp80comp.4`) whose power was calibrated relative to the hard 90° carbon pulse. Heteronuclear decoupling was achieved employing the WALTZ-16[14,15] sequence. The FID received, consisting of 65536 time domain points within a spectral width of 28.4 kHz, was zero-filled by a factor of two. The FIDs were multiplied by an exponential apodization function (1 Hz line broadening) prior to Fourier transform. Phase correction was done manually, followed by automatic baseline correction.

2.2.4 ^{1}H PSYCHE

Pure shift ^{1}H-NMR spectra for assignments were recorded with the interferogram based PSYCHE[7] pulse sequence. PSYCHE homonuclear decoupling was performed with a 30 ms long element (`Crp_psyche.20`) consisting of two saltire low power chirp pulses[7] with 20° flip angle, 10 kHz sweep width, and 15 ms durations each. Power calibration was hard coded in the pulse program. The gradient during the chirp pulse in the PSYCHE element was rectangular (`RECT.1`), had a duration of 30 ms and a strength of 1.95 %. Gradients for coherence selection (`SMSQ10.100`) had durations of 1 ms each, and 77 % and 49 % gradient strength, respectively. 8192 time domain points over a spectral width of 6.3 kHz were acquired in 128 scans with a recycle delay of 2 s. The number of chunks was set to 32 for a spectral window of 50 Hz. Reconstruction of the pure shift FID was done by the `pshift` macro downloaded from the Manchester NMR Methodology Group of Prof. Gareth A. Morris (https://www.nmr.chemistry.manchester.ac.uk). The FIDs received, consisting of 8136 time domain points were zero-filled to 16384 points and multiplied by an exponential apodization function (0.3 Hz line broadening) prior to Fourier transform. Phase correction was done manually, followed by automatic baseline correction.

2.2.5 ^{1}H,^{1}H CLIP-COSY

Proton-proton correlations for assignments were obtained by the CLIP-COSY[6] pulse sequence. Frequency-swept chirp pulses[16] of 20 ms length were utilized as adiabatic z-filter pulses. Both pulses had a bandwidth of 25 kHz and were 20 % smoothed. The mixing delay $\Delta = (2\ {}^nJ_{\mathrm{HH}})^{-1}$ was set according to a coupling constant of 30 Hz. The gradients during the chirp pulses were both rectangular (`RECT.1`), had a duration of 20 ms and a strength of 7.2 % and −7.5 %, respectively. The purge gradient pulse (`SMSQ10.100`) of 1 ms length prior to the final proton pulse was set to −17.9 % gradient strength. In the direct dimension 4096 total number of time domain points were collected over a spectral width of 7.7 kHz and for the indirect dimension 128 increments were recorded over a spectral width of 7.7 kHz. 16 scans per increment were acquired with a recycle delay of 1.5 s. The acquired FIDs were zero-filled by a factor of two in both dimensions and multiplied by a 90° shifted squared sine bell function in both dimensions prior to Fourier transform. Phase correction was done manually in both dimensions, followed by an automatic baseline correction.

2.2.6 ^{1}H,^{1}H F1-PSYCHE-CLIP-COSY

Proton-proton correlations for assignments were obtained by the CLIP-COSY[9] pulse sequence with PSYCHE homonuclear decoupling in the indirect dimension. The pulse sequence used was an in-house variant of the published pulse sequence. Two frequency-swept chirp pulses[16] of 20 ms and 30 ms length were utilized as adiabatic z-filter pulses. Both z-filter pulses had a bandwidth of 25 kHz and 60 kHz, respectively, and were 20 % smoothed. The gradients during the chirp pulses were both rectangular (`RECT.1`), had a duration of 20 ms and 30 ms and a strength of 6.5 % and 9.25 %, respectively. The purge gradient pulse (`SMSQ10.100`) of 1 ms length prior to the final proton pulse was set to −17.9 % gradient strength. The mixing delay $\Delta = (2\ {}^nJ_{\mathrm{HH}})^{-1}$ was set according to a coupling constant of 20 Hz. PSYCHE homonuclear decoupling in the indirect dimension (F1) was performed with a 30 ms long element (`Crp_psyche.20`) consisting of two low power chirp pulses with 20° flip angle, 10 kHz sweep width and 15 ms durations each. Power calibration was hard coded in the pulse program. The gradient during the chirp pulse in the PSYCHE element was rectangular (`RECT.1`), has a duration of 30 ms and a strength of 1.95 %. Gradients for coherence selection (`SMSQ10.100`) had durations of 1 ms each, and 77 % and 49 % gradient strength, respectively. In the direct dimension 4096 total number of time domain points were collected over a spectral width of 9.8 kHz and for the indirect dimension 2048 increments were recorded over a spectral width of 5.6 kHz. 8 scans per increment were acquired with a recycle delay of 2 s. The acquired FIDs were zero-filled by a factor of two in both dimensions and multiplied by a 90° shifted squared sine bell function in both dimensions prior to Fourier transform. Phase correction was done manually in both dimensions, followed by an automatic baseline correction.

2.2.7 ^{1}H,^{1}H EASY-ROESY

EASY-ROESY spectra for assignments were obtained by the pulse sequence `roesyadjsphpr`[8] from the *Bruker* pulse sequence library. The mixing delay was set to $\tau_m = 200$ ms. The EASY-ROESY mixing was performed using two spinlocks with a spinlock angle of 45° with respect to the transversal plane and an RF field of 6.4 kHz and duration of 100 ms each. The frequency offsets for spinlocking were shifted by +6.4 kHz (high frequency) and −6.4 kHz (low frequency) relative to the offset. Each ramp (half-Gaussian shape) has a duration of 1 ms. Power calibration and the offset calculation for symmetrical shifting were hard coded in the pulse program. Purge gradients before and after the spinlock had a smoothed-square shape (`SMSQ10.100`) with 1 ms duration and strengths of 31 % and 11 %, respectively. In the direct dimension 2048 total number of time domain points were collected over a spectral width of 9.8 kHz and for the indirect dimension 512 increments were recorded over a spectral width of 5.6 kHz. 8 scans per increment were acquired with a recycle delay of 2 s. The acquired FIDs were zero-filled by a factor of two in both dimensions and multiplied by a 90° shifted squared sine bell function in both dimensions prior to Fourier transform. Phase correction was done manually in both dimensions, followed by an automatic baseline correction.

2.2.8 ^{1}H,^{13}C HSQC (full spectral width)

Proton-carbon correlations for assignments were obtained by the pulse sequence `hsqcetgpsp.2` from the *Bruker* pulse sequence library. The INEPT delay was optimized for a coupling constant of $^1J_{\mathrm{HC}} = 145\,\mathrm{Hz}$. In the direct dimension 2048 total number of time domain points were collected over a spectral width of 9.8 kHz and for the indirect dimension 512 increments were recorded over a spectral width of 26.4 kHz. 4 scans per increment were acquired with a recycle delay of 1.5 s. The acquired FIDs were zero-filled by a factor of two in both dimensions and multiplied by a 90° shifted squared sine bell function in both dimensions prior to Fourier transform. Phase correction was done manually in both dimensions, followed by an automatic baseline correction.

2.2.9 ^{1}H,^{15}N HSQC (full spectral width)

Proton-nitrogen correlations for assignments were obtained by the pulse sequence `hsqcetf3gp`[17] from the *Bruker* pulse sequence library. The INEPT delay was optimized for a coupling constant of $^1J_{\mathrm{HN}} = 90\,\mathrm{Hz}$. In the direct dimension 2048 total number of time domain points were collected over a spectral width of 9.8 kHz and for the indirect dimension 64 increments were recorded over a spectral width of 4.3 kHz. 128 scans per increment were acquired with a recycle delay of 1.5 s. The acquired FIDs were zero-filled by a factor of two in both dimensions and multiplied by a 90° shifted squared sine bell function in both dimensions prior to Fourier transform. Phase correction was done manually in both dimensions, followed by an automatic baseline correction.

2.2.10 ^{1}H,^{13}C HMBC

Proton-carbon correlations for assignments were obtained by the pulse sequence `hmbcetgpl3nd`[18,19] from the *Bruker* pulse sequence library. The period for ^{1}H–^{13}C long-range coupling evolution was optimized for a coupling constant of $^nJ_{\mathrm{HC}} = 8\,\mathrm{Hz}$. The three-fold low-pass J-filter was optimized by setting the expected minimum and maximum for a one-bond ^{1}H–^{13}C J-coupling constant to $^1J_{\mathrm{HC}} = 120\,\mathrm{Hz}$ and $^1J_{\mathrm{HC}} = 170\,\mathrm{Hz}$, respectively. In the direct dimension 4096 total number of time domain points were collected over a spectral width of 8.4 kHz and for the indirect dimension 256 increments were recorded over a spectral width of 35.2 kHz. 64 scans per increment were acquired with a recycle delay of 1.5 s. The acquired FIDs were zero-filled by a factor of two in both dimensions and multiplied by a sine bell function in both dimensions prior to Fourier transform. The indirect dimension was processed in the magnitude mode.

2.2.11 ^{1}H,^{15}N HMBC

Proton-nitrogen correlations for assignments were obtained by the pulse sequence `hmbcgpndqf`[18] from the *Bruker* pulse sequence library. The period for ^{1}H–^{15}N long-range coupling evolution was optimized for a coupling constant of $^nJ_{\mathrm{HN}} = 8\,\mathrm{Hz}$. In the direct dimension 4096 total number of time domain points were collected over a spectral width of 9.3 kHz and for the indirect dimension 256 increments were recorded over a spectral width of 17.7 kHz. 128 scans per increment were acquired with a recycle delay of 1.5 s. The acquired FIDs were zero-filled by a factor of two in both dimensions and multiplied by a sine bell function in both dimensions prior to Fourier transform. The indirect dimension was processed in the magnitude mode.

2.2.12 ^{1}H,^{13}C HSQC (aliased)

Proton-carbon correlations were obtained by the pulse sequence `hsqcetgpsp.2` from the *Bruker* pulse sequence library. The INEPT delay was optimized for a coupling constant of $^1J_{\mathrm{HC}} = 145\,\mathrm{Hz}$. In the direct dimension 1398 total number of time domain points were collected over a spectral width of 7 kHz and for the indirect dimension 24 increments were recorded over a spectral width of 4.2 kHz. 16 scans per increment were acquired with a recycle delay of 1.5 s. The acquired FIDs were zero-filled to the next power of two in both dimensions and multiplied by a 90° shifted squared sine bell function in both dimensions prior to Fourier transform. Phase correction was done manually in both dimensions, followed by an automatic baseline correction.

2.2.13 ^{1}H,^{15}N HSQC (aliased)

Proton-nitrogen correlations were obtained by the pulse sequence `hsqcetf3gp`[17] from the *Bruker* pulse sequence library. The INEPT delay was optimized for a coupling constant of $^1J_{\mathrm{HN}} = 90\,\mathrm{Hz}$. In the direct dimension 1398 total number of time domain points were collected over a spectral width of 7 kHz and for the indirect dimension 8 increments were recorded over a spectral width of 220 Hz. 128 scans per increment were acquired with a recycle delay of 1.5 s. The acquired FIDs were zero-filled to the next power of two in both dimensions and multiplied by a 90° shifted squared sine bell function in both dimensions prior to Fourier transform. Phase correction was done manually in both dimensions, followed by an automatic baseline correction.

2.2.14 ^{1}H Inversion Recovery

Proton longitudinal relaxation rates $R_1 = T_1^{-1}$ were measured with the pulse sequence `t1ir`[20] from the *Bruker* pulse sequence library. In the direct dimension 65536 total number of time domain points were collected over a spectral width of 14.1 kHz. The delay t between the 90° and 180° pulse was varied (VDLIST, t ={0.1, 0.5, 1, 2, 4, 8, 14, 20} s). The acquired FIDs were zero-filled by a factor of two in the direct dimension and multiplied by an exponential apodization function (0.3 Hz line broadening) in the direct dimension prior to Fourier transform. Phase correction was done manually, followed by an automatic baseline correction. From the measured intensities I, R_1 was obtained by fitting to Equation 1.

$$I(t) = I_0\left[1 - 2\exp(-R_1 t)\right] \tag{1}$$

2.2.15 ^{1}H PROJECT

Proton transverse relaxation rates R_2 were measured with the PROJECT[10] pulse sequence. The interpulse delay was set to $\tau = 500\,\mu\mathrm{s}$, which fulfills $\tau J \ll 1$ for common proton proton scalar coupling constants ($^nJ_{\mathrm{HH}} < 20\,\mathrm{Hz}$) to suppress J-modulation. In the direct dimension 65536 total number of time domain points were collected over a spectral width of 14.1 kHz. Analysis was performed with Equation 2, which was fitted to the extracted signal intensities I to give the transverse relaxation rate R_2 using Equation 3 for the determination of the duration t. N is the repetition number of spin echoes, τ the length of the interpulse delay defined in the pulse sequence and P1 the length of the 90° proton pulse. The double spin echos were executed for 8 selected numbers of repetition (N ={10, 20, 50, 80, 150, 250, 500, 1000}), which equals roughly to t ={0.02, 0.04, 0.1, 0.16, 0.3, 0.5, 1, 2} s.

$$I(t) = I_0 \exp(-R_2 t) \tag{2}$$

$$t = N \cdot (4\tau + 5 \cdot \mathrm{P1}) \tag{3}$$

The acquired FIDs were zero-filled by a factor of two in the direct dimension and multiplied by an exponential apodization function (0.3 Hz line broadening) in the direct dimension prior to Fourier transform. Phase correction was done manually, followed by an automatic baseline correction. For analysis the acquired intensities were fitted with an exponential decay function as described in section 7.

2.2.16 ^{1}H Double Stimulated Echo (DSTE) with Bipolar Gradient Pulses

Diffusion measurements were performed by using the pulse sequence `dstebpgp3s`[11] from the *Bruker* pulse sequence library. The z-gradient was varied in 16 linear steps from 2 % up to 98 % of 54 $\mathrm{G\,s\,cm^{-1}}$ maximum gradient strength. All gradient pulse-pairs δ had a duration of 2 ms (pulse sequence parameter P30 $= 1000\,\mu\mathrm{s}$) and use the shape file `SMSQ10.100`. In the direct dimension 16384 total number of time domain points were collected over a spectral width of 14 kHz. The diffusion delay Δ was optimized prior to the measurement with the 1-dimensional variant `dstebpgp3s1d` (also *Bruker* pulse sequence library) to achieve little attenuation at low gradient strengths and high attenuation at high gradient strengths. Therefore, Δ varies between 50 ms for low peptide concentrations to 120 ms for high peptide concentrations. The acquired FIDs were zero-filled by a factor of two in the direct dimension and multiplied by a exponential apodization function (0.3 Hz line broadening) in the direct dimension prior to Fourier transform. Phase correction was done manually, followed by an automatic baseline correction.

The attenuation curves obtained were fitted with Equation 43 to yield the diffusion coefficients D considering shaped and double bipolar gradients[21] as described in section 4.

2.2.17 ^{1}H STD Amplifications

STD experiments were carried out with an adapted version of the pulse sequence published by Mayer and Meyer[12] in the default 1D variant or in a pseudo 2D form (pulse sequences for the use on *Bruker* spectrometers are provided in the supplementary material). Selective saturation was achieved by applying a pulse train for a set time (t_{sat}). Each pulse train consisted of 5 ms selective ESnob[22] pulses with delays of 5 ms between them. Power calibration was hard coded in the pulse program. In the direct dimension 65536 total number of time domain points were collected over a spectral width of 14.1 kHz. The selective pulse length was a trade-off between, on the one hand, the maximum power introduced into the sample and thus obtaining strong STD signal amplifications and the excitation bandwidth (here 384.4 Hz at the 3 dB point),[23] on the other hand. The offset of the selective pulse train was set on resonance of proton $^{\mathrm{P}}$H8 in **1** for each temperature. This resonance and the nearest resonance of **2** ($^{\mathrm{D}}$H1) were separated at least by 1100 Hz ensuring no direct excitation of diol resonances by the pulse train and thus leading to false STD responses. A saturation profile of an ESnob cascade is shown in section 10, that confirms no saturation outside of about 2.5 times the calculated excitation bandwidth. The off-resonance irradiation was placed at −10 ppm. The acquired FIDs were zero-filled by a factor of two in the direct dimension and multiplied by a exponential apodization function (0.3 Hz line broadening) in the direct dimension prior to Fourier transform. Phase correction was done manually, followed by an automatic baseline correction. Analysis of the acquired data is shown in section 8.

3 Chemical Shift Fits

3.1 Fitting Procedure

NMR signals of exchanging species are affected by the nature of chemical exchange. As no individual signal sets were observed for the different Gibbs or bound species in the investigation of **1** and **2** and mixtures of **1** and **2** and all chemical shifts reported herein gradually change with temperature and/or concentration, we treat chemical exchange as fast on the NMR time scale. For the description of signals in the slow exchange regime the reader is referred to Reference 24.

In the fast exchange regime the shifts are observed as an averaged value over all individual species according to Equation 4.

$$\langle \delta_j \rangle = \sum_i \alpha_i \, \delta_{i,j} \tag{4}$$

Here, $\delta_{i,j}$ denotes the chemical shift of the proton j in the compound i and is a fitting parameter in the later procedure. The corresponding weight fraction α_i of that compound scales the individual contribution to the observed signal. The sum over all fractions equals 1. Weight fractions depend on the position of equilibria. With every equilibrium reaction an equilibrium constant (K) is connected, which is the quotient of the on-rate (k_f) and off-rate (k_b). The whole set of equilibrium reactions that contributes to an equilibrium model (EM) needs to be defined before any chemical shift fitting is performed. Thus, several plausible equilibrium models need to be fitted against the experimental data. In general, a good fit expressed by a low RMSD (root of the mean square deviation), but also the chemical shifts derived by a fit ($\delta_{i,j}$) need to be reasonable.[25]

To perform a fit, several chemical shifts of at least one proton originating from different concentrations at the same temperature are required (also called binding isotherm). In the case of only one temperature, the Gibbs energy (ΔG) according to Gibbs energy isotherm Equation 5[26] can be used to determine the equilibrium constants of association (K_A) at that specific temperature.

$$\Delta G = -RT \ln(K_A) \quad \Leftrightarrow \quad K_A = \exp\left(-\frac{\Delta G}{RT}\right) \tag{5}$$

The temperature dependency of the Gibbs energy can be expressed as a function of absolute temperature by the Gibbs–Helmholtz Equation 6.[26] By assuming a temperature independent enthalpy ($\Delta H \neq \Delta H(T)$), enthalpy and entropy are used to determine the temperature dependent equilibrium constants via Equations 5 and 6.

$$\Delta G = \Delta H - T\Delta S \tag{6}$$

The actual fitting of NMR chemical shifts was carried out using the `fminsearch` algorithm[27] of *Matlab R2020b* (version 9.9.0.1718557). The scripts are provided in the supplementary material. The input requires: the experimental chemical shifts, the equilibrium model in the form of the differential rate equations, initial values for the thermodynamic parameters (ΔG for one temperature or ΔH and ΔS for multiple temperatures), the total concentrations for peptide ($[\mathrm{P}]_t$) and diol ($[\mathrm{D}]_t$), and the temperatures at which the chemical shifts have been determined. The differential equations for the equilibrium models are different for each model and are described in the following sections. In general, the scripts utilize the numerical solving of sets of differential equations dictated by the underlying equilibrium model to yield the equilibrium concentrations. For every temperature the corresponding equilibrium constant $K_A(T)$ is calculated, from which the equilibrium concentrations $[\,]_i$ at that temperature follow. From that, the weight fractions α_i are determined. In some specific cases, the analytical solution of the differential equations in equilibrium is known and therefore used. For each proton signal j the experimental chemical shifts are fitted simultaneously against all concentrations at equilibrium. The free parameters for this fit are the chemical shifts of pure species $\delta_{i,j}$. The variable to be optimized is the root of the mean square deviation (RMSD, Equation 7) between the observed and calculated chemical shifts for all provided n data points.

$$\mathrm{RMSD} = \sqrt{\frac{1}{N}\sum_n^N \left(\delta_n^{\mathrm{exp}} - \delta_n^{\mathrm{calc}}\right)^2} \tag{7}$$

Ranges can optionally be defined in which chemical shifts of the pure substances must lie, to reach a convergence of the fit for plausible chemical shifts (*e.g.* −100 ppm or 1000 ppm are no reasonable proton chemical shifts in the context of the binding processes studied herein[25]). The definition of a chemical shift range can be considered as lower and upper boundaries for each temperature and signal in each occurring species. These ranges ensure a plausible order of magnitude of the values and are handled similarly to force constants known from a force field. If the ranges are violated, the squares of the deviations multiplied by a constant (here 1×10^6) are added to the RMSD as a penalty.

The fits to probe interactions with the peptide were done with the amide ($^{\mathrm{P}}$H7, $^{\mathrm{P}}$H16, $^{\mathrm{P}}$H25, $^{\mathrm{P}}$H31), aromatic ($^{\mathrm{P}}$H28, $^{\mathrm{P}}$H29), and α-protons ($^{\mathrm{P}}$H2, $^{\mathrm{P}}$H8, $^{\mathrm{P}}$H26) of peptide **1**. Fits involving interactions to the diol **2** were performed with all aliphatic protons ($^{\mathrm{D}}$H1, $^{\mathrm{D}}$H2eq, $^{\mathrm{D}}$H2ax, $^{\mathrm{D}}$H3eq, $^{\mathrm{D}}$H3ax). For studies performed with both peptide and diol present in the same sample, all 14 protons were used simultaneously in one combined fit.

Those protons were selected here as they showed the greatest shift changes, and therefore had the smallest relative errors. If any other proton chemical shifts are reported, those have not been used to determine association constants, but were calculated from the fit produced.

A good strategy for optimizing enthalpy and entropy as quickly and purposefully as possible is to first optimize each temperature individually using information at multiple concentrations. Then perform a linear fit with the Gibbs energies obtained, which provides initial values for enthalpy and entropy that are already close to the minimum. The values determined this way were then used as initial values for the global fit.

3.2 Uncertainty Estimation

In order to estimate uncertainties of the parameters obtained, the procedure according to de Levie was applied.[28] For this, a standard deviation σ was estimated by assuming a symmetrical interval of the fit parameters represented here as vector $\boldsymbol{\beta}$. The standard deviation was calculated by Equation 8, where N and P are the number of data points and parameters used in the corresponding fit, respectively, and m_{ii}^{-1} are the diagonal elements of the inverse of the $P \times P$ matrix $\mathbf{M}$.

$$\sigma(\beta_i) \approx \sqrt{\frac{m_{ii}^{-1}\chi^2}{N-P}} \tag{8}$$

χ^2 is defined (Equation 9) as the sum over the squared differences between an observed value y and the fitted value $F(x,\boldsymbol{\beta})$, that depends on a general variable x and the fit parameter vector $\boldsymbol{\beta}$.

$$\chi^2 = \sum_{n}^{N} \left(y_n^{\mathrm{exp}} - F_n(x_n, \boldsymbol{\beta}) \right)^2 \tag{9}$$

The matrix elements of $\mathbf{M}$ are defined as the sum over all partial differentials given by Equation 10.

$$m_{ij} = \sum_{n}^{N} \frac{\partial F_n}{\partial \beta_i} \cdot \frac{\partial F_n}{\partial \beta_j} \tag{10}$$

In practice, the partial differentials are calculated numerically by Newton's difference quotient with the assumption of a small variation d (Equation 11). In all uncertainty estimations d was fixed to the value 10^{-10}, which is sufficiently small in our case of chemical shift fitting.

$$\frac{\partial F_n}{\partial \beta_i} = \lim_{\beta_i \to 0} \frac{\Delta F_n}{\Delta \beta_i} \approx \frac{F_n(x_n, (1+d)\beta_i, \beta_{j\neq i}) - F_n(x_n, \beta_i, \beta_{j\neq i})}{(1+d)\beta_i - \beta_i} \tag{11}$$

3.3 Equilibrium Models

Species of the peptide are denoted with $\mathrm{P_n}$ and the diol with $\mathrm{D_m}$. Equilibrium concentrations were derived from numerically solving the given differential equations over a certain time period until the concentrations did not change anymore ($\frac{\mathrm{d}}{\mathrm{d}t}\mathbf{c} = 0$). Here, **c** and **r** are both vectors of concentrations and reactions rates, respectively. The matrix $\boldsymbol{\nu}$ contains the stoichiometric factors to ensure the law of mass conservation is adhered.

$$\frac{\mathrm{d}}{\mathrm{d}t}\mathbf{c} = \boldsymbol{\nu}\mathbf{r}^T$$

The equilibrium concentration was averaged over the last 5 s of the time period to overcome potential oscillations introduced by the solving algorithm (`ode15s`[29,30]). Additionally, the standard deviation for every calculated equilibrium concentration should not exceed 1×10^{-8} M to ensure an equilibrated value.

3.3.1 Peptide Self-Association (EM-P1, monomer-dimer self-association)

Self-association of tetrapeptide **1** can be described in the simplest way as two monomers that form a homodimer.

$$2\,\mathrm{P} \xrightleftharpoons{K} \mathrm{P_2}$$

From the law of mass action (Equation 12) and the mass balance (Equation 13), Equation 14 follows directly, which can be solved analytically.

$$[\mathrm{P_2}] = K\,[\mathrm{P}]^2 \tag{12}$$

$$[\mathrm{P}]_t = 2\,[\mathrm{P_2}] + [\mathrm{P}] \tag{13}$$

$$0 = 2K\,[\mathrm{P}]^2 + [\mathrm{P}] - [\mathrm{P}]_t \tag{14}$$

The weight fractions (Equation 15) of the two species in equilibrium can be derived from the solution of Equation 14 (Equation 16).

$$\alpha_{\mathrm{P}_i} = \frac{i[\mathrm{P}_i]}{[\mathrm{P}]_t} \qquad i = 1,2 \tag{15}$$

$$[\mathrm{P}] = \frac{1}{4K}\left(-1 + \sqrt{1 - 8K\,[\mathrm{P}]_t}\right) \tag{16}$$

The chemical shifts obtained can be well described by Equations 4 and 15. The RMSD for the fit for the temperature ranged from 270 K to 310 K is 2.473×10^{-2} ppm. The enthalpy and entropy obtained were $\Delta H = (-59.76 \pm 9.86)\,\mathrm{kJ\,mol^{-1}}$ and $\Delta S = (-152.92 \pm 32.97)\,\mathrm{J\,K^{-1}\,mol^{-1}}$, respectively. Figure S5 shows the fit for proton $^{\mathrm{P}}$H16 (amide) and Figure S6 shows the resulting molar fractions x of the peptide monomer and dimer depending on the total peptide concentration $[\mathrm{P}]_t$. The fitted chemical shifts for peptide monomer and dimer at 300 K are given in Table S10. The experimental data is represented well by this equilibrium model, but due to discrepancies in the diffusion coefficient (sec. 4), another model (EM-P2) was also fitted to the data.

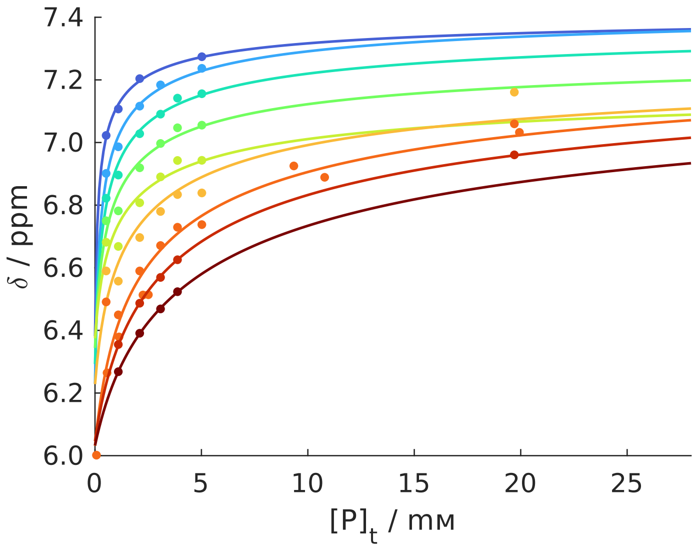

Figure S5: Fitted chemical shifts for ^{P}H16 by the global chemical shift fitting procedure with equilibrium model EM-P1. The measured temperature range from 270 K (blue) to 310 K (dark red) in 5 K steps and the total peptide concentration $[P]_t$ range from 0 mM up to 20 mM is shown. Bullets (●) represent measured data points, while the solid lines (—) represents the fit.

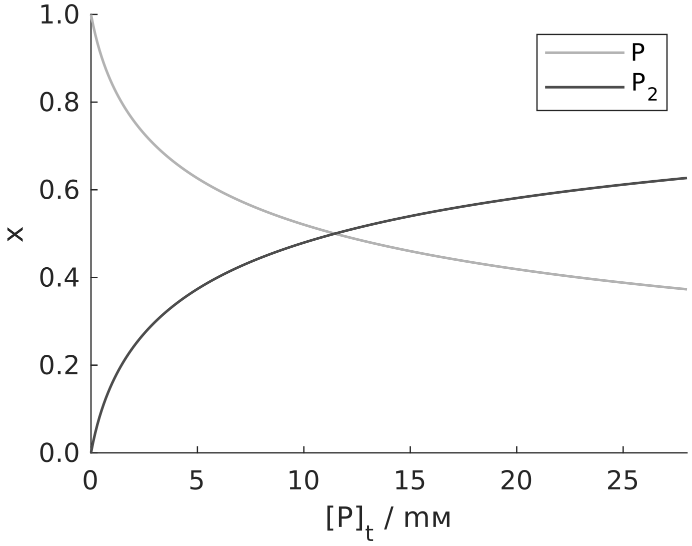

Figure S6: The molar fractions for the equilibrium model EM-P1 derived by the chemical shift fitting procedure at 300 K.

Table S10: Fitted proton chemical shifts for monomeric (δ_{P}) and dimeric peptide (δ_{P_2}) for the equilibrium model EM-P1 at the best fit solution. Shifts at 300 K.

Proton j	$\delta_{\mathrm{P},j}$ / ppm	$\delta_{\mathrm{P}_2,j}$ / ppm	Proton j	$\delta_{\mathrm{P},j}$ / ppm	$\delta_{\mathrm{P}_2,j}$ / ppm
H7	6.562 ± 0.022	8.573 ± 0.029	H14ax	1.171 ± 0.010	1.278 ± 0.013
H16	6.031 ± 0.020	7.381 ± 0.026	H15ax	0.751 ± 0.010	0.902 ± 0.013
H25	5.120 ± 0.025	7.859 ± 0.033	H15eq	1.715 ± 0.018	1.827 ± 0.022
H31	5.134 ± 0.020	6.336 ± 0.025	H19a	1.979 ± 0.010	2.237 ± 0.013
H28	6.868 ± 0.018	7.118 ± 0.023	H19b	1.778 ± 0.018	2.215 ± 0.022
H29	7.006 ± 0.030	7.339 ± 0.029	H3a	3.068 ± 0.010	3.190 ± 0.013
H2	4.880 ± 0.018	5.010 ± 0.023	H3b	2.879 ± 0.010	3.124 ± 0.013
H8	4.578 ± 0.018	4.945 ± 0.023	H22a	1.339 ± 0.010	1.578 ± 0.014
H26	3.996 ± 0.019	4.747 ± 0.024	H22b	1.281 ± 0.010	1.469 ± 0.014
H10	1.348 ± 0.017	1.528 ± 0.017	H9a	1.799 ± 0.010	1.856 ± 0.014
H11ax	0.832 ± 0.010	0.956 ± 0.013	H9b	1.553 ± 0.018	1.758 ± 0.022
H11eq	1.669 ± 0.018	1.832 ± 0.022	H1	3.251 ± 0.010	3.355 ± 0.013
H12ax	1.209 ± 0.010	1.327 ± 0.014	H30	2.863 ± 0.010	3.128 ± 0.013
H13ax	1.068 ± 0.010	1.161 ± 0.013	H32	1.384 ± 0.010	1.411 ± 0.013
H13eq	1.570 ± 0.018	1.652 ± 0.020			

3.3.2 Peptide Self-Association (EM-P2, isodesmic model)

In the isodesmic model or equal-K model, the number of monomers increases stepwise by 1 in the corresponding oligomers. All equilibrium steps exhibit the same equilibrium constant K.

$$\mathrm{P}_{i-1} + \mathrm{P} \overset{K}{\rightleftharpoons} \mathrm{P}_i \qquad i = 2 \ldots \infty$$

An analytical solution can also be found for this equilibrium model by series expansion. Equation 17, that defines all weight fractions directly, was taken from Reference 31.

$$\alpha_{\mathrm{P}_i} = \frac{i\,[\mathrm{P}_i]}{[\mathrm{P}]_t} = i\,(K\,[\mathrm{P}]_t)^{i-1} \left(\frac{2K\,[\mathrm{P}]_t + 1 - \sqrt{1 + 4K[\mathrm{P}]_t}}{2K^2\,[\mathrm{P}]_t^2} \right)^i \tag{17}$$

Dimers and higher oligomers are grouped together to P_ξ that exhibit one averaged observable $\delta_{\mathrm{P}_\xi,j}$ for each proton.

$$\alpha_{\mathrm{P}_\xi} = \sum_{i=2}^{\infty} \alpha_{\mathrm{P}_i} = 1 - \alpha_{\mathrm{P}} \tag{18}$$

The result of the fit with this model also leads to a small RMSD (2.614×10^{-2} ppm). Enthalpy and entropy for each association step were $\Delta H = (-41.82 \pm 4.03)\,\mathrm{kJ\,mol^{-1}}$ and $\Delta S = (-94.50 \pm 13.45)\,\mathrm{J\,K^{-1}\,mol^{-1}}$, respectively. Figure S7 shows the fit for proton $^{\mathrm{P}}$H16 (amide) and Figure S8 shows the resulting molar fractions x of the peptide monomer and oligomers depending on the total peptide concentration $[\mathrm{P}]_t$. The RMSD is slightly higher, but the estimated uncertainties on ΔH and ΔS are smaller, compared to the other equilibrium model (EM-P1). This is also reflected in smaller errors of chemical shifts obtained for this model (as compared to EM-P1). (Table S11).

Only by analyzing the chemical shifts (compare Figure S5 and S7) it is thus not possible to distinguish whether the data is better represented by the simple monomer-dimer model (EM-P1) or the isodesmic model (EM-P2). The data can be fitted with the same accuracy to both models as the RMSD's point out. The models are nevertheless spectroscopically distinguishable since the diffusion coefficient represents an absolute reference (see section 4).

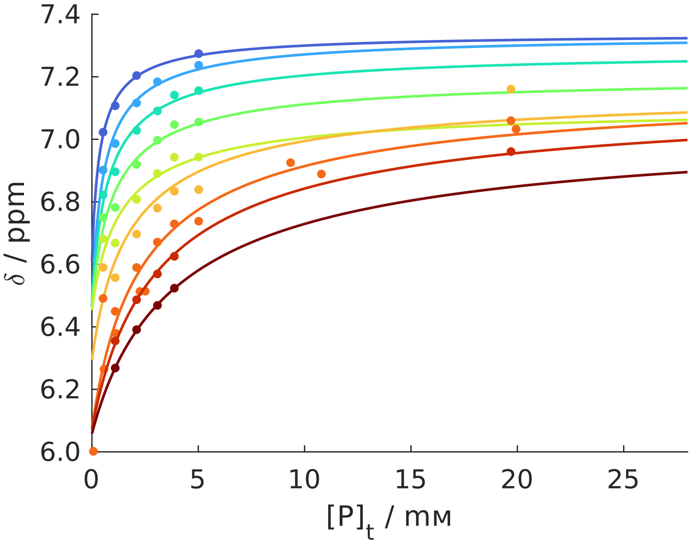

Figure S7: Fitted chemical shifts for ^{P}H16 by the global chemical shift fitting procedure with equilibrium model EM-P2. The measured temperature range from 270 K (blue) to 310 K (dark red) in 5 K steps and the total peptide concentration $[P]_t$ range from 0 mM up to 20 mM is shown. Bullets (●) represent measured data points, while the solid lines (—) represents the fit.

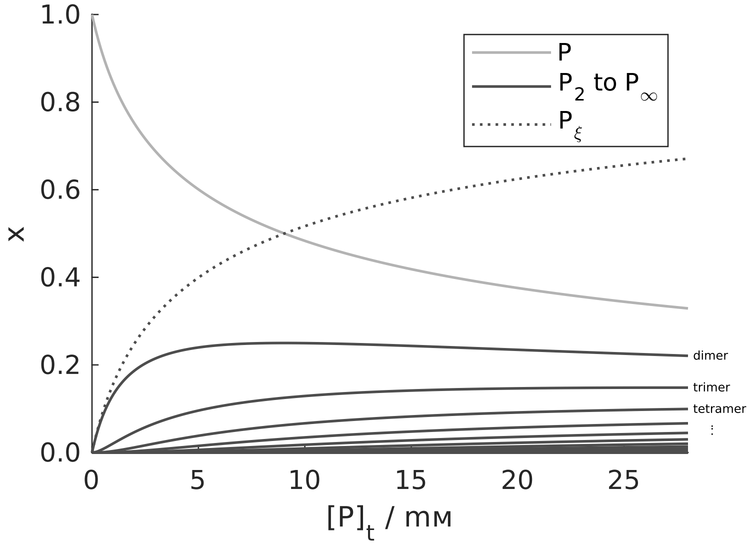

Figure S8: The molar fractions derived for the equilibrium model EM-P2 by the chemical shift fitting procedure at 300 K. Dimers and higher oligomers are grouped together to P_ξ. The black dotted line represents the sum of all black solid lines, that is also equal to $1 - x_P$.

Table S11: Fitted proton chemical shifts for monomeric (δ_{P}) and oligomeric peptide (δ_{P_ξ}) for the equilibrium model EM-P2 at the best fit solution. Shifts at 300 K.

Proton j	$\delta_{\mathrm{P},j}$ / ppm	$\delta_{\mathrm{P}_\xi,j}$ / ppm	Proton j	$\delta_{\mathrm{P},j}$ / ppm	$\delta_{\mathrm{P}_\xi,j}$ / ppm
H7	6.622 ± 0.021	8.262 ± 0.022	H14ax	1.175 ± 0.014	1.262 ± 0.014
H16	6.073 ± 0.020	7.171 ± 0.020	H15ax	0.756 ± 0.014	0.880 ± 0.014
H25	5.203 ± 0.023	7.435 ± 0.025	H15eq	1.720 ± 0.024	1.810 ± 0.024
H31	5.171 ± 0.019	6.150 ± 0.020	H19a	1.987 ± 0.014	2.198 ± 0.014
H28	6.876 ± 0.018	7.080 ± 0.019	H19b	1.796 ± 0.024	2.145 ± 0.024
H29	7.019 ± 0.029	7.287 ± 0.023	H3a	3.072 ± 0.014	3.172 ± 0.014
H2	4.885 ± 0.018	4.990 ± 0.019	H3b	2.887 ± 0.014	3.087 ± 0.014
H8	4.590 ± 0.018	4.889 ± 0.019	H22a	1.347 ± 0.014	1.542 ± 0.015
H26	4.019 ± 0.019	4.631 ± 0.019	H22b	1.288 ± 0.014	1.441 ± 0.015
H10	1.356 ± 0.022	1.500 ± 0.017	H9a	1.801 ± 0.014	1.848 ± 0.015
H11ax	0.837 ± 0.014	0.937 ± 0.014	H9b	1.562 ± 0.024	1.725 ± 0.024
H11eq	1.676 ± 0.024	1.806 ± 0.024	H1	3.255 ± 0.014	3.340 ± 0.014
H12ax	1.213 ± 0.014	1.309 ± 0.015	H30	2.871 ± 0.014	3.087 ± 0.014
H13ax	1.071 ± 0.014	1.147 ± 0.014	H32	1.386 ± 0.014	1.408 ± 0.014
H13eq	1.574 ± 0.024	1.639 ± 0.021			

3.3.3 Diol Self-Association (EM-D1, stepwise trimerization)

It is known from previous studies that *trans*-cyclohexane-1,2-diol (**2**) mainly forms trimers in apolar solvents.[32] Thus, the stepwise assembly of the trimer (via the dimer) can be formulated, with each step associated with its own equilibrium constant (in contrast to EM-D2, see below). The laws of mass action are given in Eqs. 20 and 21. The weight fractions for this equilibrium model are defined in Equation 19.

$$2\,\mathrm{D} \xrightleftharpoons{K_1} \mathrm{D_2}$$
$$\mathrm{D} + \mathrm{D_2} \xrightleftharpoons{K_2} \mathrm{D_3}$$

$$\alpha_{\mathrm{D}_i} = \frac{i[\mathrm{D}_i]}{[\mathrm{D}]_t} \qquad i = 1,2,3 \tag{19}$$

$$[\mathrm{D_2}] = K_1[\mathrm{D}]^2 \tag{20}$$
$$[\mathrm{D_3}] = K_2[\mathrm{D}][\mathrm{D_2}] \tag{21}$$
$$[\mathrm{D}]_t = 3\,[\mathrm{D_3}] + 2\,[\mathrm{D_2}] + [\mathrm{D}] \tag{22}$$
$$0 = 3\,K_1K_2[\mathrm{D}]^3 + 2\,K_1[\mathrm{D}]^2 + [\mathrm{D}] - [\mathrm{D}]_t \tag{23}$$

The cubic Equation 23 can be solved analytically. Of the three theoretical solutions, however, only one is physically meaningful (real and positive concentration), which is described in Equation 24. From the parameters p (Equation 25) and q (Equation 26), the determinant Δ (Equation 27) of the cubic equation can be determined, which determines the case to be applied in Equation 24.

$$[\mathrm{D}] = \begin{cases} -\frac{2}{9K_2} + \sqrt[3]{-\frac{q}{2} + \sqrt{-\Delta}} + \sqrt[3]{-\frac{q}{2} - \sqrt{-\Delta}} & \text{if } \Delta < 0 \\ -\frac{2}{9K_2} + \sqrt{-\frac{4}{3}p}\,\cos\left(\frac{1}{3}\,\mathrm{acos}\left(-\frac{q}{2}\sqrt{-\frac{27}{p^3}}\right)\right) & \text{if } \Delta \geq 0 \end{cases} \tag{24}$$

$$p = \frac{27K_1K_2 - 12K_1^2}{81K_1^2K_2^2} \tag{25}$$

$$q = -\frac{[\mathrm{D}]_t}{3K_1K_2} - \frac{2}{27K_1K_2^2} + \frac{16}{729K_2^3} \tag{26}$$

$$\varDelta = -\frac{q^2}{4} - \frac{p^3}{27} \tag{27}$$

For this model, the best fitting solution with small RMSD (2.132×10^{-3} ppm) is physically unreasonable (fit not shown here): The shifts of D_2 however showed negative values. The chemical shifts have therefore been narrowed down into ranges and fitted again. The ranges are 0.7 to 4 ppm for the protons at positions 2 and 3 and 1 to 7 ppm for proton $^{\mathrm{D}}$H1. With these constraints, the RMSD is only slightly higher (2.151×10^{-3} ppm). Figure S9 shows the fit for proton $^{\mathrm{D}}$H1 at temperatures between 270 K and 300 K and Figure S10 shows the determined molar fractions x in equilibrium depending on the total diol concentration $[\mathrm{D}]_t$.

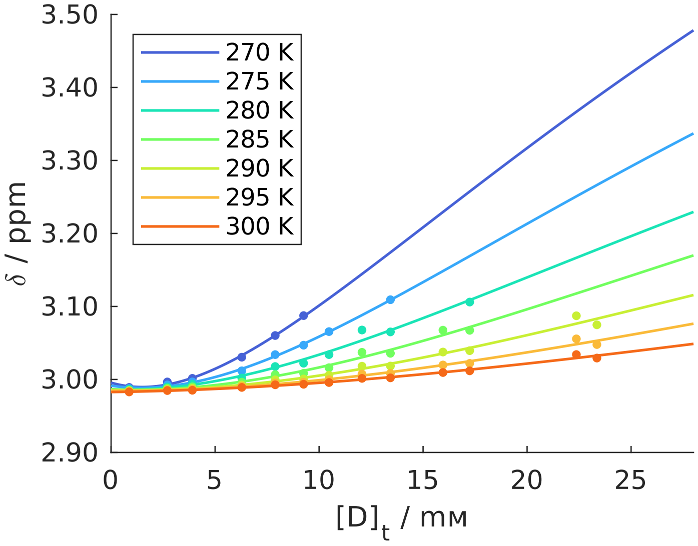

Figure S9: Fitted chemical shifts for $^{\mathrm{D}}$H1 by the global chemical shift fitting procedure with equilibrium model EM-D1. The measured temperature range from 270 K (blue) to 300 K (red) in 5 K steps and the total diol concentration $[\mathrm{D}]_t$ range from 0 mM up to 23 mM is shown. Bullets (•) represent measured data points, while the solid lines (—) represents the fit.

Nevertheless, the uncertainties on the obtained fit parameters are enormous. Enthalpy and entropy for the first step (dimer formation) were $\varDelta H_1 = (-82.52 \pm 116.08)\,\mathrm{kJ\,mol^{-1}}$ and $\varDelta S_1 = (-287.61 \pm 436.75)\,\mathrm{J\,K^{-1}\,mol^{-1}}$, respectively. For the second step (trimer formation) both quantities were $\varDelta H_2 = (35.58 \pm 126.38)\,\mathrm{kJ\,mol^{-1}}$ and $\varDelta S_2 = (160.15 \pm 466.26)\,\mathrm{J\,K^{-1}\,mol^{-1}}$, respectively. This is also reflected in the errors of chemical shifts determined (Table S12), especially those of the dimer, but also those of the trimer.

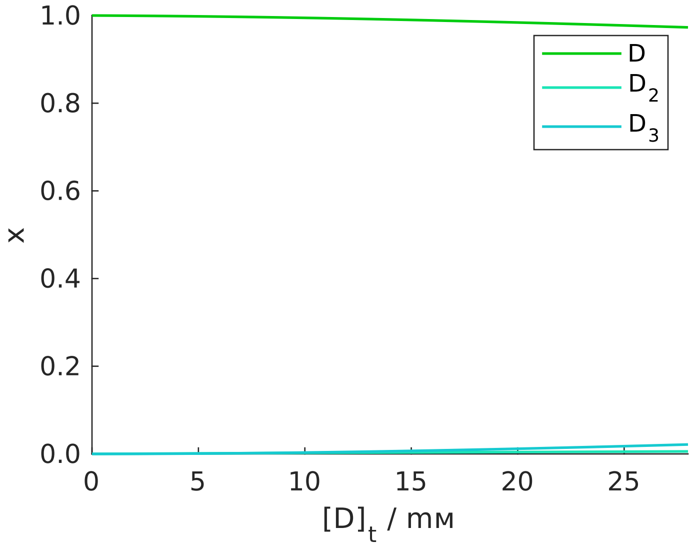

Figure S10: The molar fractions derived for the equilibrium model EM-D1 by the chemical shift fitting procedure at 300 K.

Table S12: Fitted proton chemical shifts for monomeric (δ_{D}), dimeric ($\delta_{\mathrm{D_2}}$), and timeric diol ($\delta_{\mathrm{D_3}}$) for the equilibrium model EM-D1 at the best fit solution. Shifts at 300 K.

Proton j	$\delta_{\mathrm{D},j}$ / ppm	$\delta_{\mathrm{D_2},j}$ / ppm	$\delta_{\mathrm{D_3},j}$ / ppm
H3ax	0.935 ± 0.002	1.085 ± 1.417	1.212 ± 0.337
H3eq	1.004 ± 0.002	1.390 ± 2.825	1.619 ± 0.657
H2ax	1.371 ± 0.002	1.537 ± 1.484	1.568 ± 0.271
H2eq	1.686 ± 0.002	2.036 ± 2.619	2.298 ± 0.657
H1	2.983 ± 0.002	3.930 ± 6.426	3.893 ± 0.946

Furthermore, the chemical shifts of the dimer and the trimer diverged at low temperatures (Table S13), at which the concentration range becomes smaller due to solubility issues, and therefore fewer data points were available.

Table S13: Fitted proton chemical shifts of proton $^{\mathrm{D}}$H1 for monomeric (δ_{D}), dimeric ($\delta_{\mathrm{D_2}}$), and timeric diol ($\delta_{\mathrm{D_3}}$) for the equilibrium model EM-D1 at the best fit solution.

T / K	$\delta_{\mathrm{D,H1}}$ / ppm	$\delta_{\mathrm{D_2,H1}}$ / ppm	$\delta_{\mathrm{D_3,H1}}$ / ppm
270	2.996 ± 0.006	2.516 ± 0.927	6.562 ± 9.592
275	2.991 ± 0.004	2.542 ± 1.121	5.576 ± 5.447
280	2.986 ± 0.003	2.775 ± 0.652	4.843 ± 3.034
285	2.986 ± 0.003	2.602 ± 1.471	4.684 ± 2.195
290	2.986 ± 0.003	2.601 ± 1.896	4.431 ± 1.468
295	2.984 ± 0.002	2.924 ± 0.820	4.176 ± 1.129
300	2.983 ± 0.002	3.930 ± 6.426	3.893 ± 0.946

Narrowing down the range of chemical shifts further in a meaningful way did not reduce the uncertainties of the fit parameters, so a slightly simplified model (EM-D2) was applied to describe the data, omitting the dimerization step.

3.3.4 Diol Self-Association (EM-D2, simultaneous trimerization)

This equilibrium model describes the simultaneous trimerization of 3 monomers *trans*-cyclohexane-1,2-diol (**2**). Here, only one equilibrium constant exists. The law of mass action is given in Equation 29. The weight fractions for this equilibrium model are defined in Equation 28.

$$3\,\mathrm{D} \xrightleftharpoons{K} \mathrm{D}_3$$

$$\alpha_{\mathrm{D}_i} = \frac{i[\mathrm{D}_i]}{[\mathrm{D}]_t} \qquad i = 1,3 \tag{28}$$

$$[\mathrm{D}_3] = K[\mathrm{D}]^3 \tag{29}$$

$$[\mathrm{D}]_t = 3\,[\mathrm{D}_3] + [\mathrm{D}] \tag{30}$$

$$0 = 3\,K[\mathrm{D}]^3 + [\mathrm{D}] - [\mathrm{D}]_t \tag{31}$$

The cubic Equation 31 is also analytically solvable and only one physically meaningful solution exists (Equation 32). Compared to model EM-D1, there comes no determinant of the cubic equation into play.

$$[\mathrm{D}] = \frac{1}{3}\left(\frac{\sqrt[3]{\sqrt{81\,K^4[\mathrm{D}]_t^2 + 4\,K^3} + 9\,K^2[\mathrm{D}]_t}}{\sqrt[3]{2}\,K} - \frac{\sqrt[3]{2}}{\sqrt[3]{\sqrt{81\,K^4[\mathrm{D}]_t^2 + 4\,K^3} + 9\,K^2[\mathrm{D}]_t}}\right) \tag{32}$$

The best fit solution had an RMSD of 2.221×10^{-3} ppm. Enthalpy and entropy for the trimer formation were $\Delta H = (-25.17 \pm 12.97)\,\mathrm{kJ\,mol^{-1}}$ and $\Delta S = (-53.69 \pm 45.63)\,\mathrm{J\,K^{-1}\,mol^{-1}}$, respectively. The uncertainties were significantly smaller than those of model EM-D1 with a roughly equal RMSD. Table S14 contains the determined chemical shifts at 300 K. Figure S11 shows the fit for proton $^{\mathrm{D}}$H1 at temperatures between 270 K and 300 K and Figure S12 shows the determined molar fractions x in equilibrium depending on the total diol concentration $[\mathrm{D}]_t$.

Table S14: Fitted proton chemical shifts for monomeric (δ_{D}) and timeric diol (δ_{D_3}) for the equilibrium model EM-D2 at the best fit solution. Shifts at 300 K.

Proton j	$\delta_{\mathrm{D},j}$ / ppm	$\delta_{\mathrm{D}_3,j}$ / ppm
H3ax	0.936 ± 0.001	1.196 ± 0.085
H3eq	1.005 ± 0.001	1.592 ± 0.173
H2ax	1.371 ± 0.001	1.566 ± 0.069
H2eq	1.687 ± 0.001	2.265 ± 0.170
H1	2.985 ± 0.001	3.910 ± 0.268

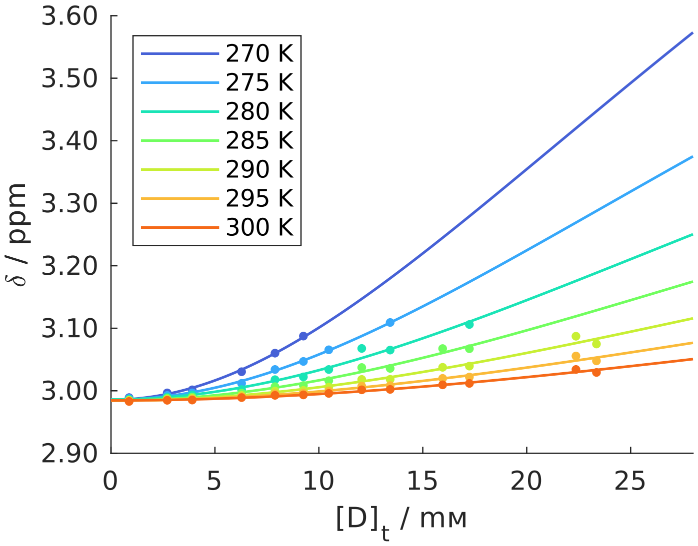

Figure S11: Fitted chemical shifts for ^{D}H1 by the global chemical shift fitting procedure with equilibrium model EM-D2. The measured temperature range from 270 K (blue) to 300 K (red) in 5 K steps and the total diol concentration $[D]_t$ range from 0 mM up to 23 mM is shown. Bullets (•) represent measured data points, while the solid lines (—) represents the fit.

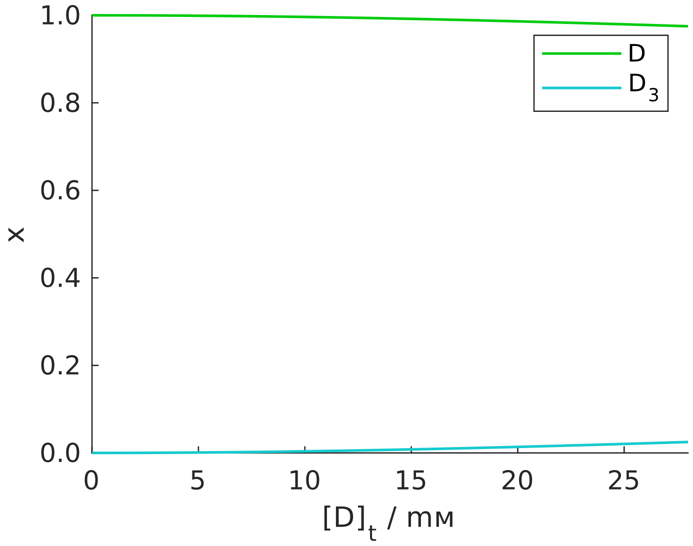

Figure S12: The molar fractions derived by the chemical shift fitting procedure at 300 K.

3.3.5 Preamble Peptide-Diol Mixtures

Several models were set up to investigate the interactions of peptide **1** and *trans*-cyclohexane-1,2-diol **2**. The models were kept as simple as possible (few equilibrium steps). Since **1** and **2** are self-associating in the concentration range observed, the models determined above were included in the considerations. As the mixture models are generally not analytically solvable, the self-association of peptide **1** was modelled here with model EM-P1, because EM-P2 contains an infinite number of peptide oligomers and the method employed in this section requires a finite number of occurring species. The chemical shifts can be described well with model EM-P1 but the chemical information value is compromised, which has to be kept in mind when evaluating the values determined. As a consistency check we required that the associated Gibbs energies of self-association of peptide and diol (models EM-P1 and EM-D2) were represented in the upcoming models. In all peptide-diol models a chemical shift range was employed as restraint. The ranges were 4 to 14 ppm for the peptide amide protons (^{P}H7, ^{P}H16, ^{P}H25, ^{P}H31), 2 to 6 ppm for the peptide α-protons (^{P}H2, ^{P}H8, ^{P}H26), 6 to 10 ppm for the peptide imidazole protons (^{P}H28, ^{P}H29), 0.7 to 4 ppm for ^{D}H2 and ^{D}H3, and 1 to 7 ppm for proton ^{D}H1. Each model was then tested against data obtained from separate mixtures of peptide **1** with both enantiomers of **2**, using the chemical shifts of peptide and diol simultaneously. The numbers of experimental data points (extracted chemical shifts) used in the fitting method were 458 and 240 for mixtures of **1** with (*R*,*R*)-**2** and (*S*,*S*)-**2**, respectively. As an extension of Hess' law,[33,34] it must be further considered that the pathways by which equilibria occur are not elementary reactions. The associations to the individual supramolecular species do not have to proceed like this in reality. Different pathways leading to the same species have to be avoided, since in these cases redundant equilibrium constants are obtained.

In the Figures in the following sections, the chemical shifts of the protons ^{P}H16 and ^{D}H1 are shown with the corresponding fitted values for each model. In addition, the molar fractions of the occurring species are shown with the equilibrium reached. As the estimated uncertainties of the Gibbs energies are less than $5\,\mathrm{J\,mol^{-1}}$ in any mixture model, a more realistic estimate is assumed to be $1\,\mathrm{kJ\,mol^{-1}}$, otherwise the accuracy of the method is overestimated. This value is based on the difference between the energies obtained from the mixture models and the energies known from the previously determined models.

To assess the models, the RMSD and the number of chemical shift restraints exceeding the range limits (shift violation) are listed in each case. A short overview of the peptide-diol models is given in Table S15 in section 3.3.6. As can be seen in the following, different results are obtained for the equilibrium compositions of mixtures of the peptide with the two respective enantiomers of the diol (*R*,*R* vs. *S*,*S*). The implications of these findings are discussed in detail in the main text.

3.3.6 Peptide-Diol Mixture Models Overview

Table S15: Overview of the peptide-diol equilibrium models described below in detail. Ticks (✓) at the corresponding equilibrium constants K_i denote the equilibria present in the equilibrium models. The equilibria are given below. Also the RMSD's and chemical shift violations at the best fit of the models against the experimental chemical shift data are given. The row of model EM-PD8 highlights the best fitting solution with the smallest RMSD's and no chemical shift violations for both mixtures.

Models	K_1	K_2	K_3	K_4	K_5	K_6	K_7	**1** + (*R*,*R*)-**2**		**1** + (*S*,*S*)-**2**	
								RMSD / ppm	violations	RMSD / ppm	violations
EM-PD1	✓	✓	✓					9.402×10^{-3}	1	6.575×10^{-3}	1
EM-PD2	✓	✓		✓				2.874×10^{-2}	14	6.378×10^{-3}	36
EM-PD3	✓	✓	✓	✓				9.275×10^{-3}	0	1.097×10^{-2}	3
EM-PD4	✓	✓	✓		✓			9.610×10^{-3}	3	3.838×10^{-3}	1
EM-PD5	✓	✓	✓	✓	✓			9.123×10^{-3}	6	2.490×10^{-3}	1
EM-PD6	✓	✓	✓	✓		✓		8.633×10^{-3}	2	3.994×10^{-3}	2
EM-PD7	✓	✓	✓	✓			✓	8.593×10^{-3}	0	2.405×10^{-3}	1
EM-PD8	✓	✓	✓	✓	✓		✓	6.487×10^{-3}	0	2.124×10^{-3}	0
EM-PD9	✓	✓	✓	✓		✓	✓	9.477×10^{-3}	10	2.125×10^{-3}	0

$$2\,\mathrm{P} \xrightleftharpoons{K_1} \mathrm{P}_2$$

$$3\,\mathrm{D} \xrightleftharpoons{K_2} \mathrm{D}_3$$

$$\mathrm{P} + \mathrm{D} \xrightleftharpoons{K_3} \mathrm{PD}$$

$$\mathrm{P}_2 + \mathrm{D} \xrightleftharpoons{K_4} \mathrm{P}_2\mathrm{D}$$

$$\mathrm{PD} + \mathrm{D} \xrightleftharpoons{K_5} \mathrm{PD}_2$$

$$\mathrm{P} + \mathrm{D}_3 \xrightleftharpoons{K_6} \mathrm{PD}_3$$

$$\mathrm{P}_2\mathrm{D} + \mathrm{D} \xrightleftharpoons{K_7} \mathrm{P}_2\mathrm{D}_2$$

3.3.7 Peptide-Diol Mixture (EM-PD1)

The simplest model consists of the combination of self-associations of both peptide and diol and a 1:1 peptide-diol interaction. The solved differential equation is given in Equation 33 and the Gibbs energies at the best fit solution are shown in Table S16.

$$2\,\mathrm{P} \xrightleftharpoons{K_1} \mathrm{P}_2$$
$$3\,\mathrm{D} \xrightleftharpoons{K_2} \mathrm{D}_3$$
$$\mathrm{P} + \mathrm{D} \xrightleftharpoons{K_3} \mathrm{PD}$$

$$\frac{\mathrm{d}}{\mathrm{d}t}\begin{pmatrix}[\mathrm{P}]\\ [\mathrm{P}_2]\\ [\mathrm{D}]\\ [\mathrm{D}_3]\\ [\mathrm{PD}]\end{pmatrix} = \begin{pmatrix}-2 & 2 & 0 & 0 & -1 & 1\\ 1 & -1 & 0 & 0 & 0 & 0\\ 0 & 0 & -3 & 3 & -1 & 1\\ 0 & 0 & 1 & -1 & 0 & 0\\ 0 & 0 & 0 & 0 & 1 & -1\end{pmatrix} \cdot \begin{pmatrix}k_{1,f}[\mathrm{P}]^2\\ k_{1,b}[\mathrm{P}_2]\\ k_{2,f}[\mathrm{D}]^3\\ k_{2,b}[\mathrm{D}_3]\\ k_{3,f}[\mathrm{P}][\mathrm{D}]\\ k_{3,b}[\mathrm{PD}]\end{pmatrix}^T \tag{33}$$

Table S16: Best fit solution for mixtures of peptide **1** with both enantiomers of diol **2** at 300 K.

Mixture	**1** + (*R*,*R*)-**2**	**1** + (*S*,*S*)-**2**
RMSD / ppm	9.402×10^{-3}	6.575×10^{-3}
shift violations	1	1
ΔG_1 / kJ mol^{-1}	−11.40	−8.23
ΔG_2 / kJ mol^{-1}	−9.60	−9.75
ΔG_3 / kJ mol^{-1}	−6.42	−4.66

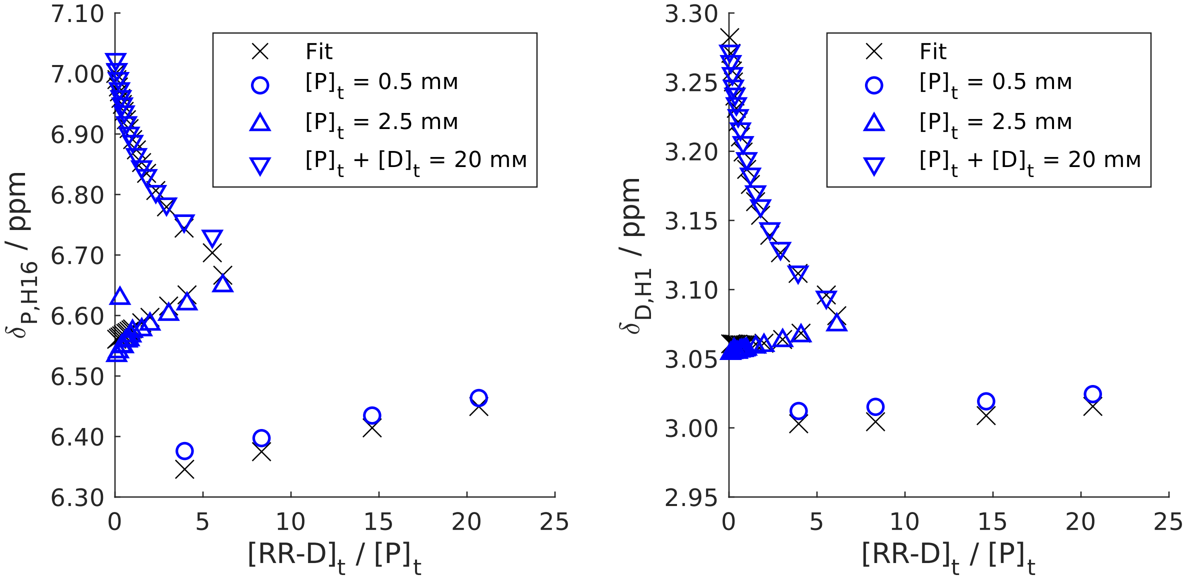

(a) (b)

Figure S13: Fitted chemical shifts versus ratio of total concentration of (*R*,*R*)-diol $[\text{RR-D}]_t$ and total peptide concentration $[\text{P}]_t$ for $^{\text{P}}$H16 (left) and $^{\text{D}}$H1 (right) by the global chemical shift fitting procedure with equilibrium model EM-PD1 at 300 K.

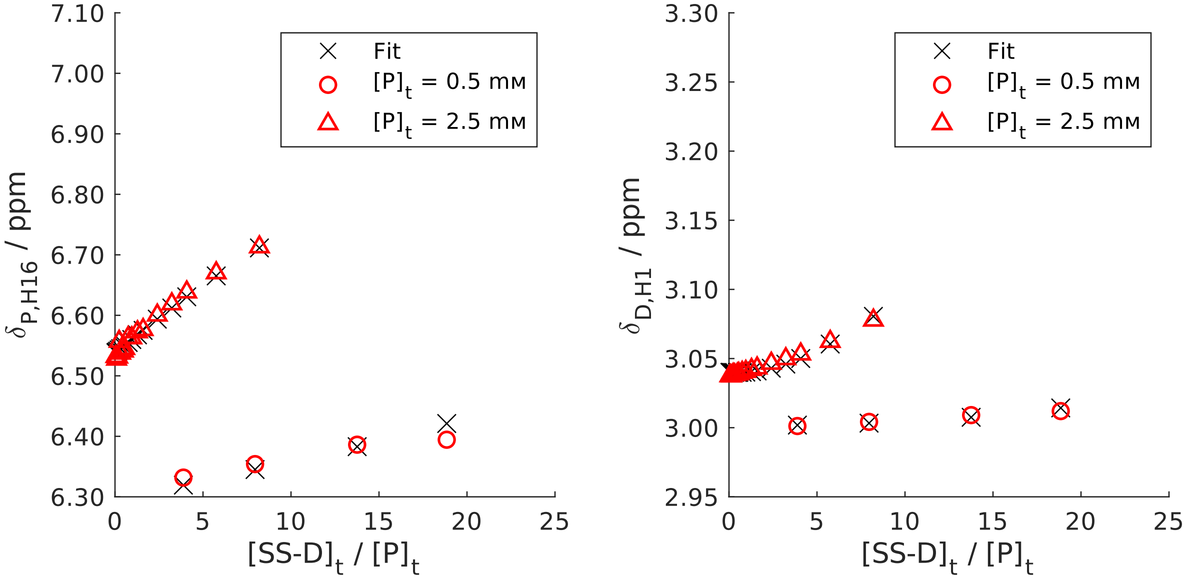

(a) (b)

Figure S14: Fitted chemical shifts versus ratio of total concentration of (*S*,*S*)-diol $[\text{SS-D}]_t$ and total peptide concentration $[\text{P}]_t$ for $^{\text{P}}$H16 (left) and $^{\text{D}}$H1 (right) by the global chemical shift fitting procedure with equilibrium model EM-PD1 at 300 K.

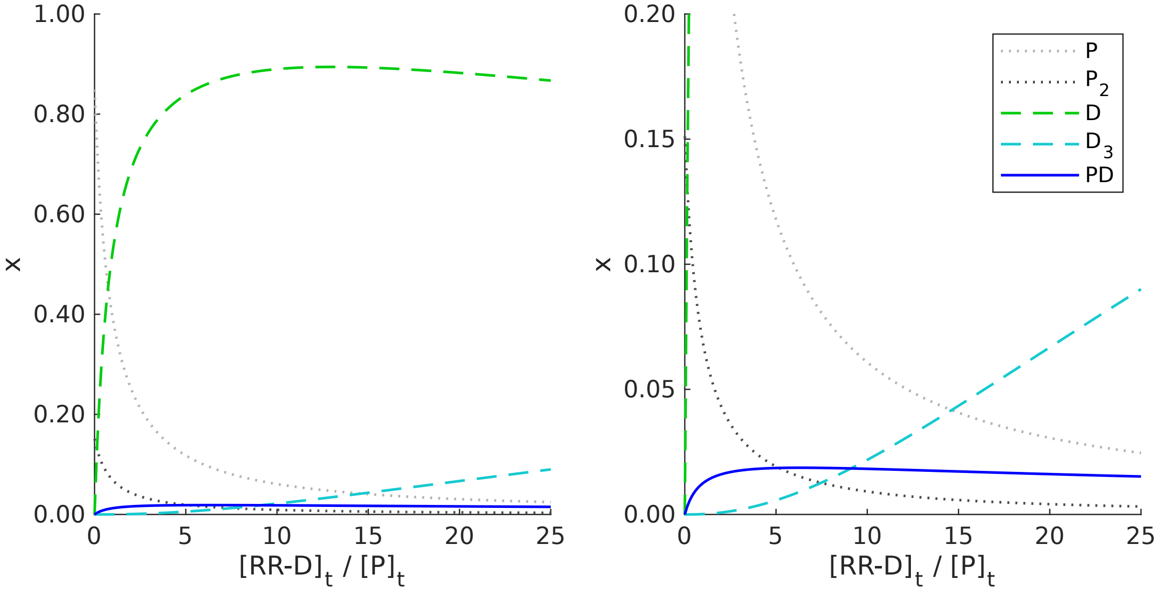

Figure S15: The molar fractions of P, P_2, D, D_3, and PD versus ratio of total concentration of (*R*,*R*)-diol $[\text{RR-D}]_t$ and total peptide concentration $[\text{P}]_t$ derived by the chemical shift fitting procedure at 300 K. The peptide concentration was kept constant at 2.5 mM. Right: zoom of the bottom 20 % area of the figure to the left.

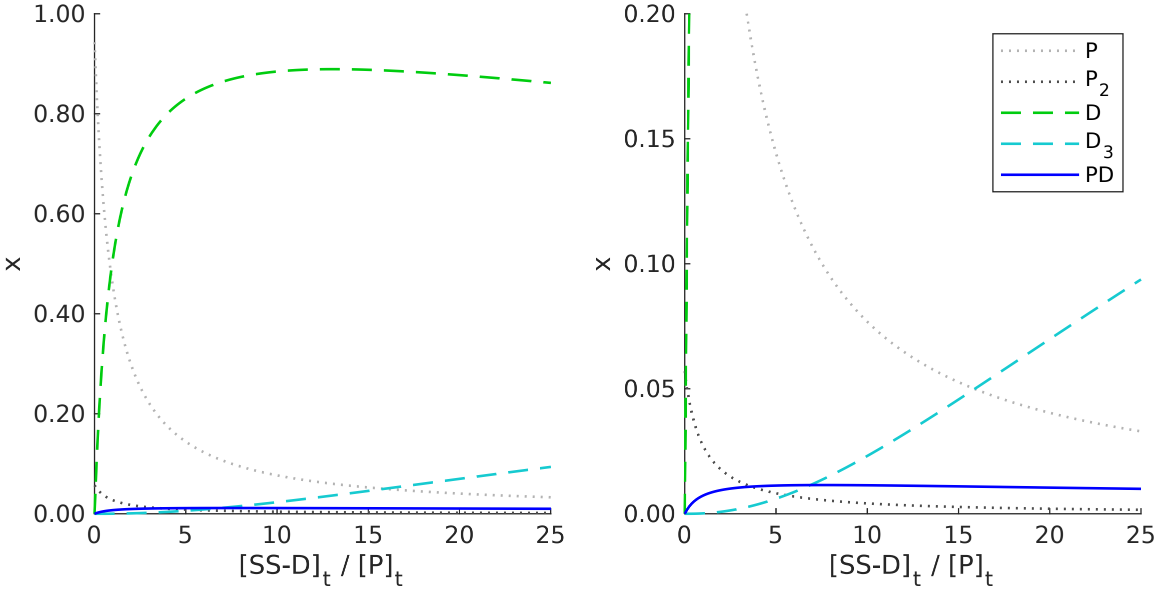

Figure S16: The molar fractions of P, P_2, D, D_3, and PD versus ratio of total concentration of (*S*,*S*)-diol $[\text{SS-D}]_t$ and total peptide concentration $[\text{P}]_t$ derived by the chemical shift fitting procedure at 300 K. The peptide concentration was kept constant at 2.5 mM. Right: zoom of the bottom 20 % area of the figure to the left.

3.3.8 Peptide-Diol Mixture (EM-PD2)

$$2\,\mathrm{P} \xrightleftharpoons{K_1} \mathrm{P_2}$$
$$3\,\mathrm{D} \xrightleftharpoons{K_2} \mathrm{D_3}$$
$$\mathrm{P_2} + \mathrm{D} \xrightleftharpoons{K_4} \mathrm{P_2D}$$

$$\frac{\mathrm{d}}{\mathrm{d}t}\begin{pmatrix}[\mathrm{P}]\\ [\mathrm{P_2}]\\ [\mathrm{D}]\\ [\mathrm{D_3}]\\ [\mathrm{P_2D}]\end{pmatrix} = \begin{pmatrix}-2 & 2 & 0 & 0 & 0 & 0\\ 1 & -1 & 0 & 0 & -1 & 1\\ 0 & 0 & -3 & 3 & -1 & 1\\ 0 & 0 & 1 & -1 & 0 & 0\\ 0 & 0 & 0 & 0 & 1 & -1\end{pmatrix} \cdot \begin{pmatrix}k_{1,f}[\mathrm{P}]^2\\ k_{1,b}[\mathrm{P_2}]\\ k_{2,f}[\mathrm{D}]^3\\ k_{2,b}[\mathrm{D_3}]\\ k_{4,f}[\mathrm{P_2}][\mathrm{D}]\\ k_{4,b}[\mathrm{P_2D}]\end{pmatrix}^T \tag{34}$$

Table S17: Best fit solution for mixtures of peptide **1** with both enantiomers of diol **2** at 300 K.

Mixture	**1** + (*R*,*R*)-**2**	**1** + (*S*,*S*)-**2**
RMSD / ppm	2.874×10^{-2}	6.378×10^{-3}
shift violations	14	36
ΔG_1 / kJ mol^{-1}	−11.01	−14.54
ΔG_2 / kJ mol^{-1}	−9.20	−7.25
ΔG_4 / kJ mol^{-1}	−4.20	−8.25

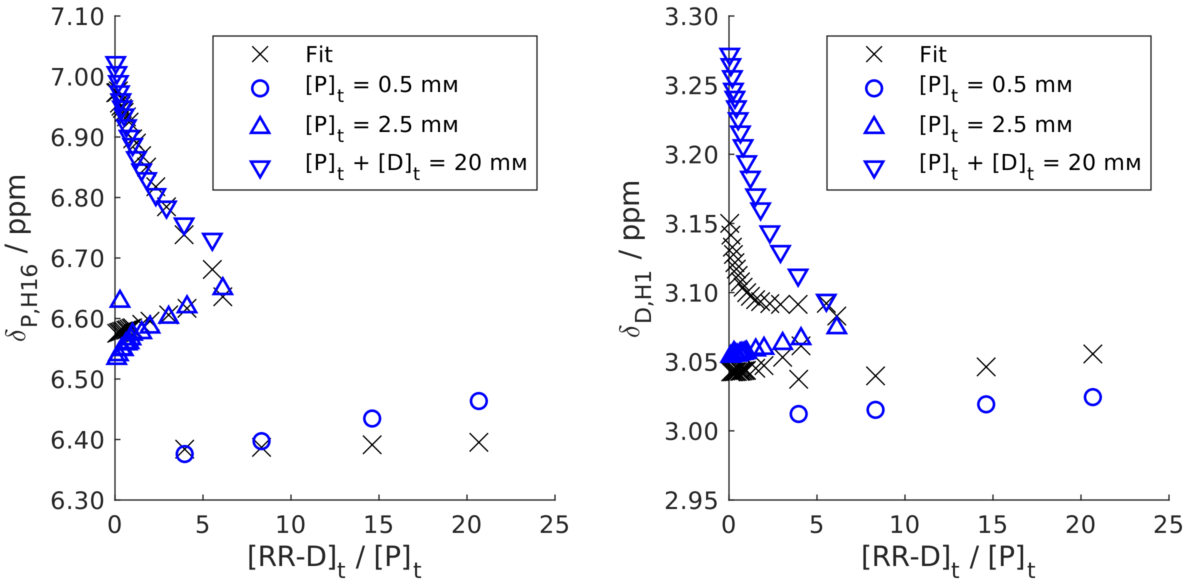

(a) (b)

Figure S17: Fitted chemical shifts versus ratio of total concentration of (*R*,*R*)-diol $[\text{RR-D}]_t$ and total peptide concentration $[\text{P}]_t$ for ^{P}H16 (left) and ^{D}H1 (right) by the global chemical shift fitting procedure with equilibrium model EM-PD2 at 300 K.

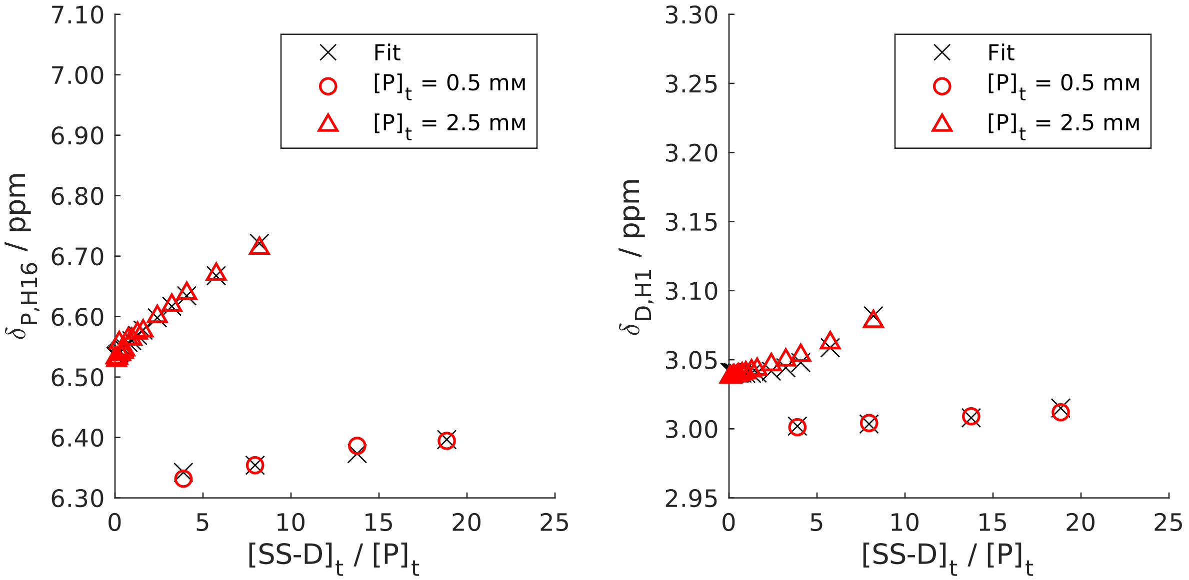

(a) (b)

Figure S18: Fitted chemical shifts versus ratio of total concentration of (*S*,*S*)-diol $[\text{SS-D}]_t$ and total peptide concentration $[\text{P}]_t$ for ^{P}H16 (left) and ^{D}H1 (right) by the global chemical shift fitting procedure with equilibrium model EM-PD2 at 300 K.

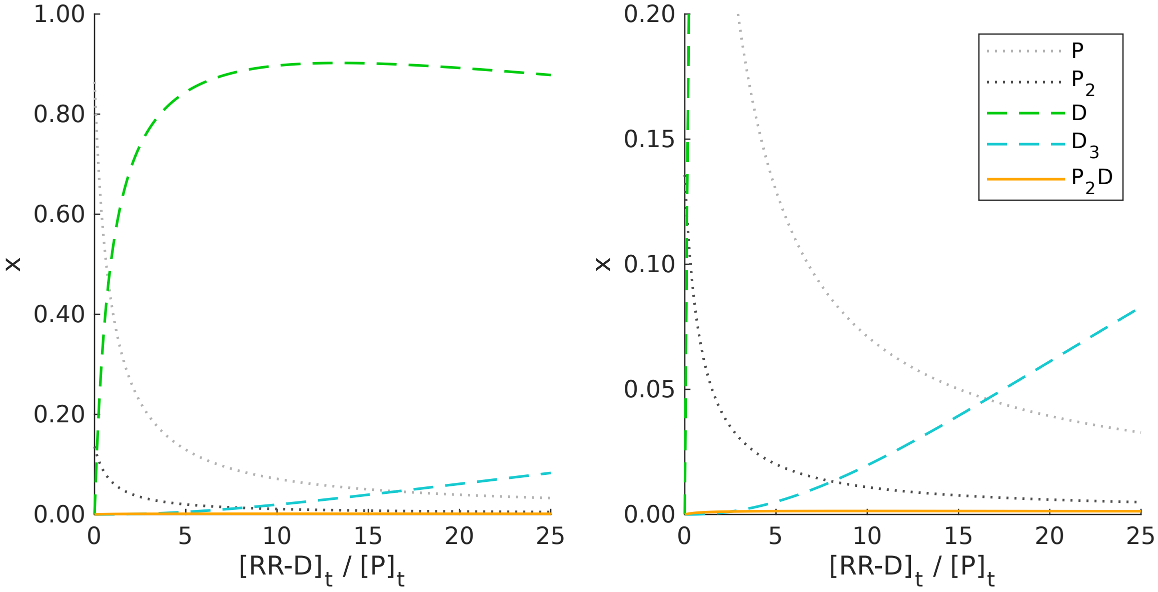

Figure S19: The molar fractions of P, P_2, D, D_3, and P_2D versus ratio of total concentration of (*R*,*R*)-diol $[\text{RR-D}]_t$ and total peptide concentration $[\text{P}]_t$ derived by the chemical shift fitting procedure at 300 K. The peptide concentration was kept constant at 2.5 mM. Right: zoom of the bottom 20 % area of the figure to the left.

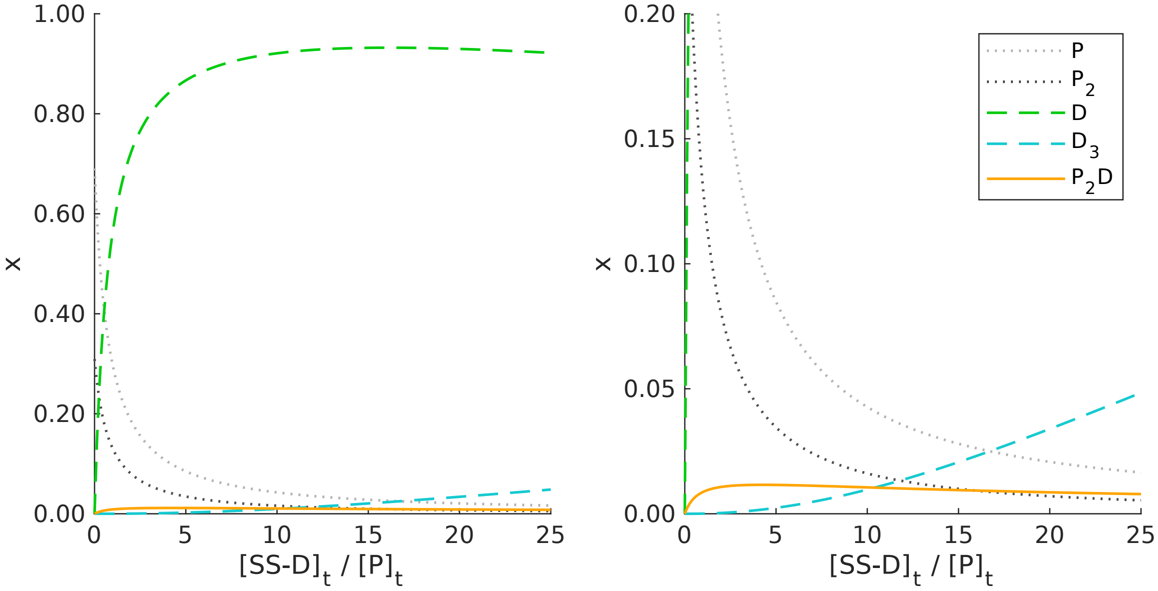

Figure S20: The molar fractions of P, P_2, D, D_3, and P_2D versus ratio of total concentration of (*S*,*S*)-diol $[\text{SS-D}]_t$ and total peptide concentration $[\text{P}]_t$ derived by the chemical shift fitting procedure at 300 K. The peptide concentration was kept constant at 2.5 mM. Right: zoom of the bottom 20 % area of the figure to the left.

3.3.9 Peptide-Diol Mixture (EM-PD3)

$$
\begin{aligned}
2\,\mathrm{P} &\xrightleftharpoons{K_1} \mathrm{P_2}\\
3\,\mathrm{D} &\xrightleftharpoons{K_2} \mathrm{D_3}\\
\mathrm{P}+\mathrm{D} &\xrightleftharpoons{K_3} \mathrm{PD}\\
\mathrm{P_2}+\mathrm{D} &\xrightleftharpoons{K_4} \mathrm{P_2D}
\end{aligned}
$$

$$
\frac{\mathrm{d}}{\mathrm{d}t}\begin{pmatrix}[\mathrm{P}]\\ [\mathrm{P_2}]\\ [\mathrm{D}]\\ [\mathrm{D_3}]\\ [\mathrm{PD}]\\ [\mathrm{P_2D}]\end{pmatrix} = \begin{pmatrix} -2 & 2 & 0 & 0 & -1 & 1 & 0 & 0\\ 1 & -1 & 0 & 0 & 0 & 0 & -1 & 1\\ 0 & 0 & -3 & 3 & -1 & 1 & -1 & 1\\ 0 & 0 & 1 & -1 & 0 & 0 & 0 & 0\\ 0 & 0 & 0 & 0 & 1 & -1 & 0 & 0\\ 0 & 0 & 0 & 0 & 0 & 0 & 1 & -1 \end{pmatrix} \cdot \begin{pmatrix} k_{1,f}[\mathrm{P}]^2\\ k_{1,b}[\mathrm{P_2}]\\ k_{2,f}[\mathrm{D}]^3\\ k_{2,b}[\mathrm{D_3}]\\ k_{3,f}[\mathrm{P}][\mathrm{D}]\\ k_{3,b}[\mathrm{PD}]\\ k_{4,f}[\mathrm{P_2}][\mathrm{D}]\\ k_{4,b}[\mathrm{P_2D}] \end{pmatrix}^{T} \tag{35}
$$

Table S18: Best fit solution for mixtures of peptide **1** with both enantiomers of diol **2** at 300 K.

Mixture	**1** + (R,R)-**2**	**1** + (S,S)-**2**
RMSD / ppm	9.275×10^{-3}	1.097×10^{-2}
shift violations	0	3
ΔG_1 / kJ mol^{-1}	−10.97	−8.43
ΔG_2 / kJ mol^{-1}	−9.38	−9.89
ΔG_3 / kJ mol^{-1}	−6.55	−8.56
ΔG_4 / kJ mol^{-1}	−8.23	−18.62

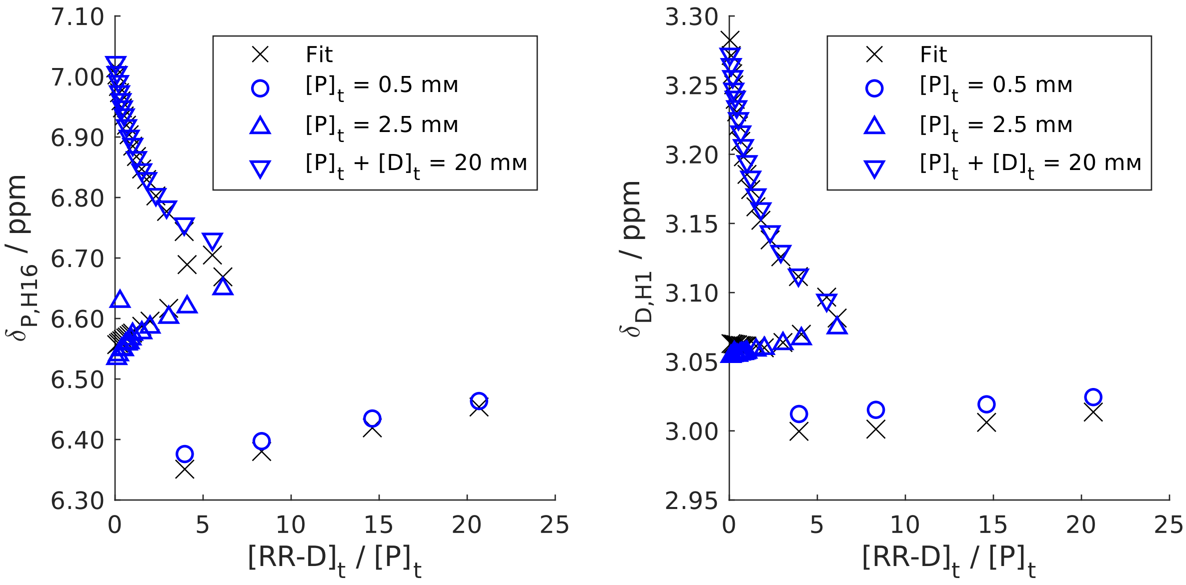

(a) (b)

Figure S21: Fitted chemical shifts versus ratio of total concentration of (*R*,*R*)-diol $[\text{RR-D}]_t$ and total peptide concentration $[\text{P}]_t$ for $^{\text{P}}$H16 (left) and $^{\text{D}}$H1 (right) by the global chemical shift fitting procedure with equilibrium model EM-PD3 at 300 K.

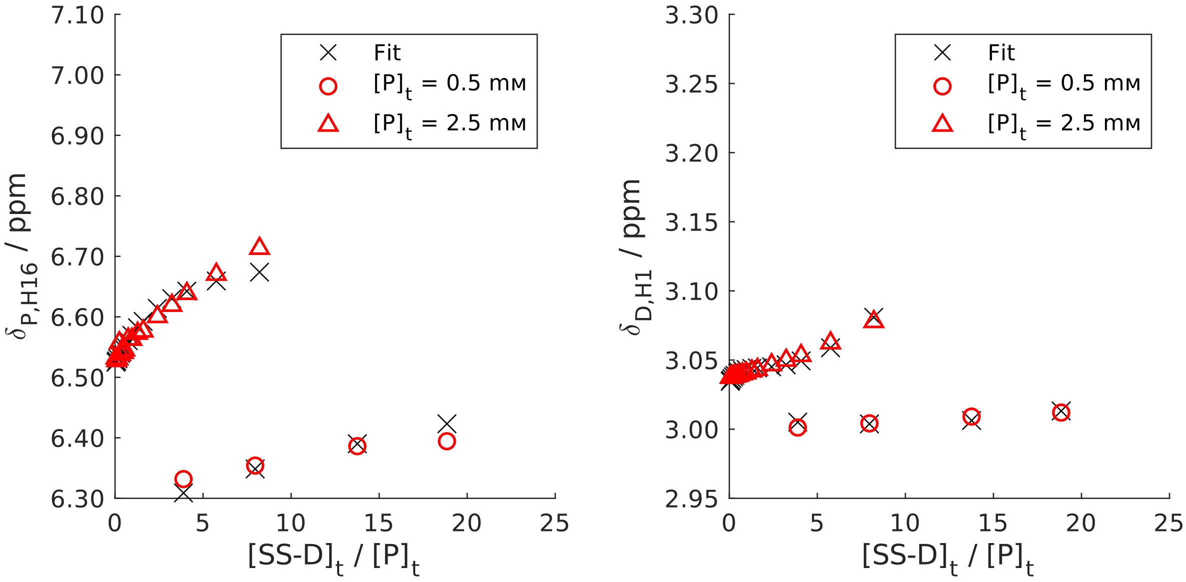

(a) (b)

Figure S22: Fitted chemical shifts versus ratio of total concentration of (*S*,*S*)-diol $[\text{SS-D}]_t$ and total peptide concentration $[\text{P}]_t$ for $^{\text{P}}$H16 (left) and $^{\text{D}}$H1 (right) by the global chemical shift fitting procedure with equilibrium model EM-PD3 at 300 K.

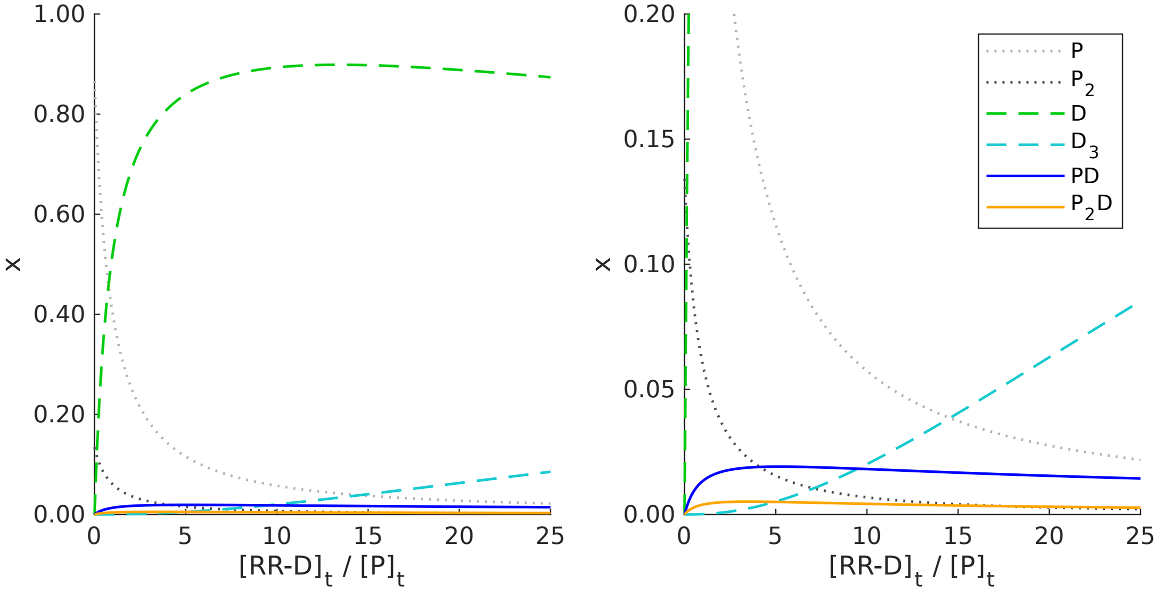

Figure S23: The molar fractions of P, P_2, D, D_3, PD, and P_2D versus ratio of total concentration of (*R*,*R*)-diol $[\mathrm{RR\text{-}D}]_t$ and total peptide concentration $[\mathrm{P}]_t$ derived by the chemical shift fitting procedure at 300 K. The peptide concentration was kept constant at 2.5 mM. Right: zoom of the bottom 20 % area of the figure to the left.

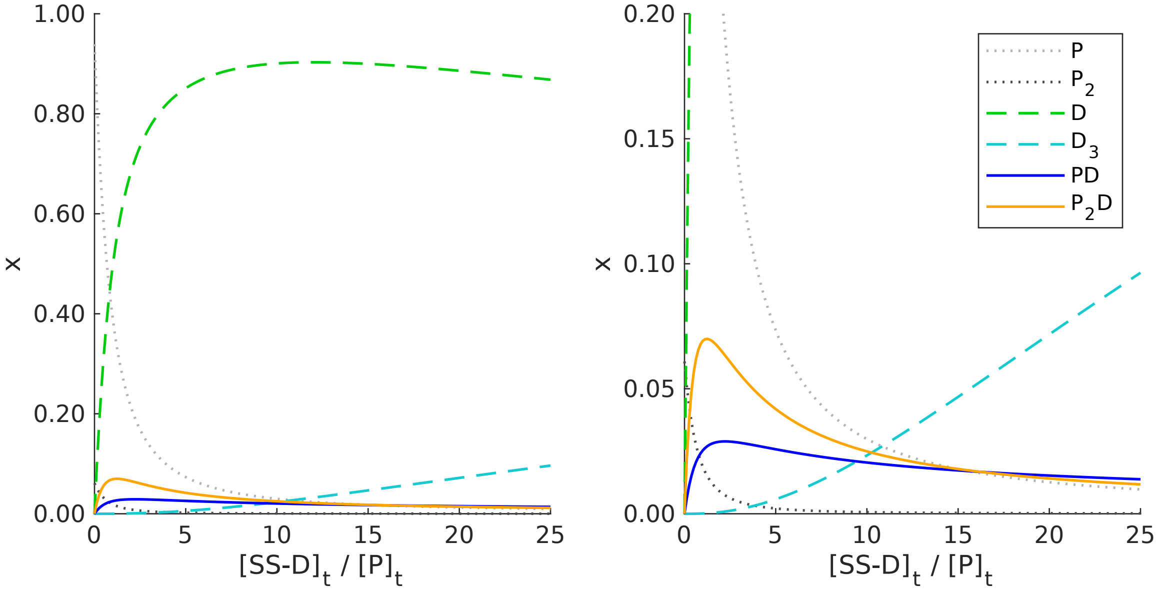

Figure S24: The molar fractions of P, P_2, D, D_3, PD, and P_2D versus ratio of total concentration of (*S*,*S*)-diol $[\mathrm{SS\text{-}D}]_t$ and total peptide concentration $[\mathrm{P}]_t$ derived by the chemical shift fitting procedure at 300 K. The peptide concentration was kept constant at 2.5 mM. Right: zoom of the bottom 20 % area of the figure to the left.

3.3.10 Peptide-Diol Mixture (EM-PD4)

$$2\,\mathrm{P} \xrightleftharpoons{K_1} \mathrm{P}_2$$
$$3\,\mathrm{D} \xrightleftharpoons{K_2} \mathrm{D}_3$$
$$\mathrm{P} + \mathrm{D} \xrightleftharpoons{K_3} \mathrm{PD}$$
$$\mathrm{PD} + \mathrm{D} \xrightleftharpoons{K_5} \mathrm{PD}_2$$

$$\frac{\mathrm{d}}{\mathrm{d}t}\begin{pmatrix}[\mathrm{P}]\\ [\mathrm{P}_2]\\ [\mathrm{D}]\\ [\mathrm{D}_3]\\ [\mathrm{PD}]\\ [\mathrm{PD}_2]\end{pmatrix} = \begin{pmatrix}-2 & 2 & 0 & 0 & -1 & 1 & 0 & 0\\ 1 & -1 & 0 & 0 & 0 & 0 & 0 & 0\\ 0 & 0 & -3 & 3 & -1 & 1 & -1 & 1\\ 0 & 0 & 1 & -1 & 0 & 0 & 0 & 0\\ 0 & 0 & 0 & 0 & 1 & -1 & -1 & 1\\ 0 & 0 & 0 & 0 & 0 & 0 & 1 & -1\end{pmatrix} \cdot \begin{pmatrix}k_{1,f}[\mathrm{P}]^2\\ k_{1,b}[\mathrm{P}_2]\\ k_{2,f}[\mathrm{D}]^3\\ k_{2,b}[\mathrm{D}_3]\\ k_{3,f}[\mathrm{P}][\mathrm{D}]\\ k_{3,b}[\mathrm{PD}]\\ k_{5,f}[\mathrm{PD}][\mathrm{D}]\\ k_{5,b}[\mathrm{PD}_2]\end{pmatrix}^T \tag{36}$$

Table S19: Best fit solution for mixtures of peptide **1** with both enantiomers of diol **2** at 300 K.

Mixture	**1** + (*R*,*R*)-**2**	**1** + (*S*,*S*)-**2**
RMSD / ppm	9.610×10^{-3}	3.838×10^{-3}
shift violations	3	1
ΔG_1 / kJ mol^{-1}	−11.31	−7.74
ΔG_2 / kJ mol^{-1}	−11.76	−10.73
ΔG_3 / kJ mol^{-1}	−5.91	−4.48
ΔG_5 / kJ mol^{-1}	−5.25	−8.01

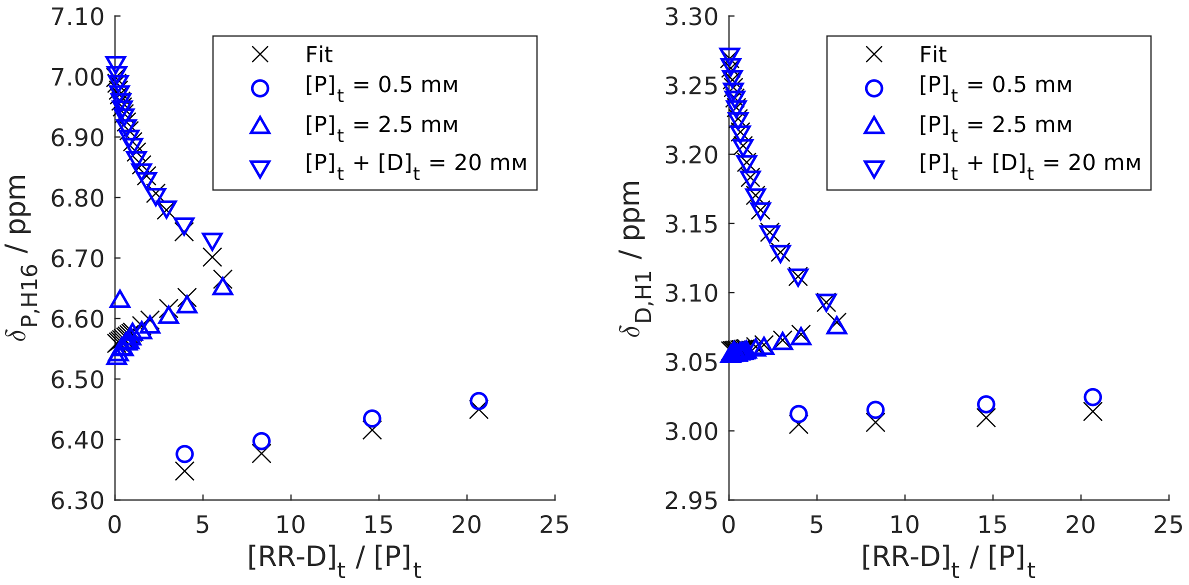

(a) (b)

Figure S25: Fitted chemical shifts versus ratio of total concentration of (*R*,*R*)-diol $[\text{RR-D}]_t$ and total peptide concentration $[\text{P}]_t$ for $^{\text{P}}$H16 (left) and $^{\text{D}}$H1 (right) by the global chemical shift fitting procedure with equilibrium model EM-PD4 at 300 K.

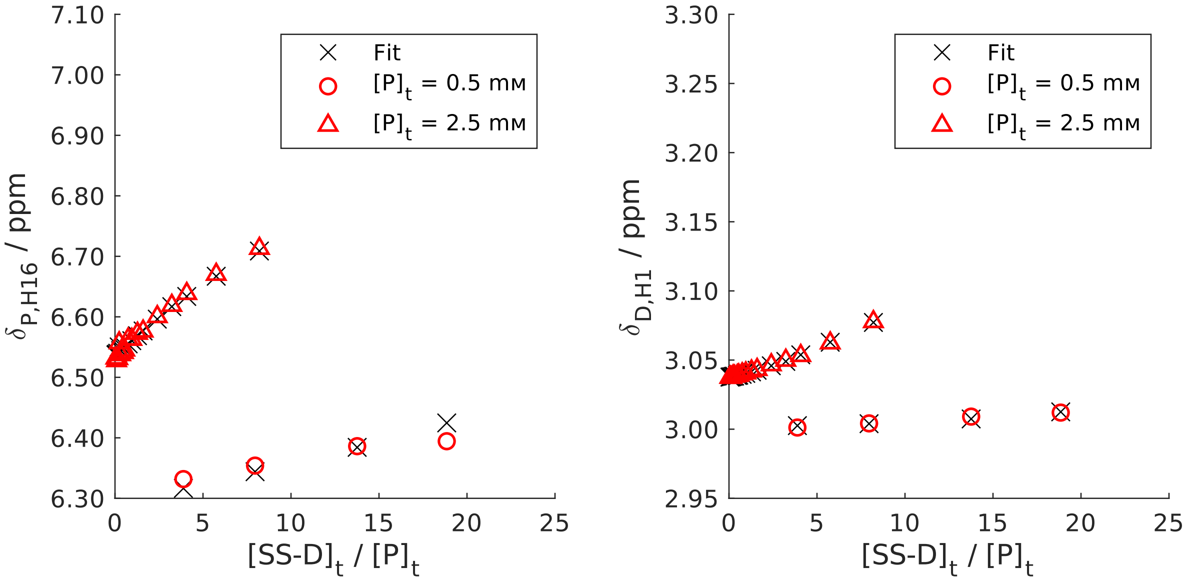

(a) (b)

Figure S26: Fitted chemical shifts versus ratio of total concentration of (*S*,*S*)-diol $[\text{SS-D}]_t$ and total peptide concentration $[\text{P}]_t$ for $^{\text{P}}$H16 (left) and $^{\text{D}}$H1 (right) by the global chemical shift fitting procedure with equilibrium model EM-PD4 at 300 K.

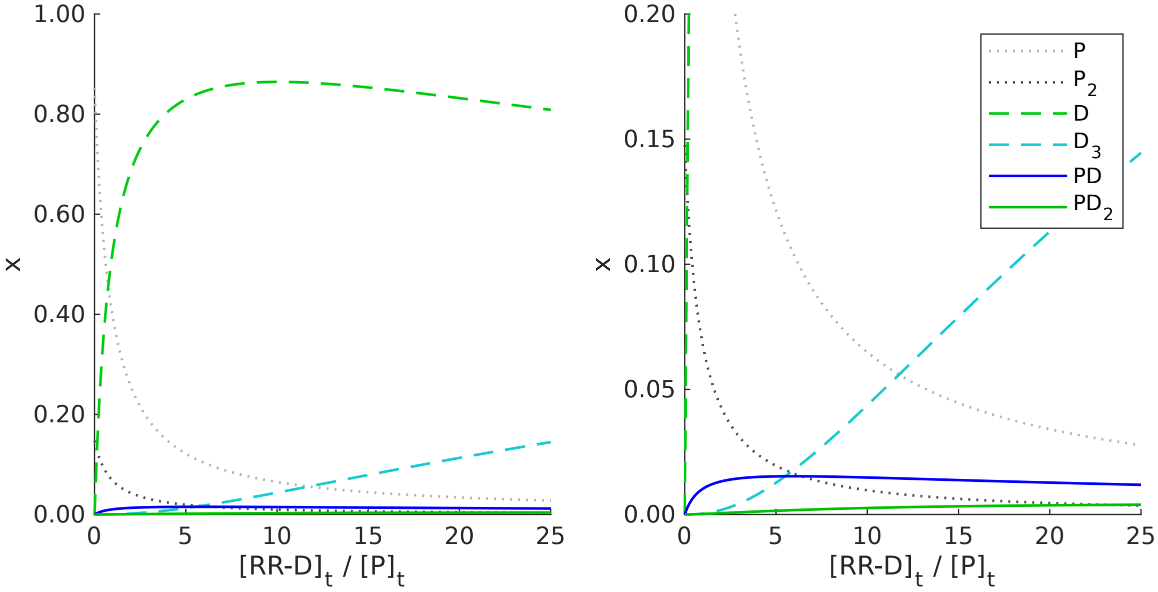

Figure S27: The molar fractions of P, P$_2$, D, D$_3$, PD, and PD$_2$ versus ratio of total concentration of (*R*,*R*)-diol [RR-D]$_t$ and total peptide concentration [P]$_t$ derived by the chemical shift fitting procedure at 300 K. The peptide concentration was kept constant at 2.5 mM. Right: zoom of the bottom 20 % area of the figure to the left.

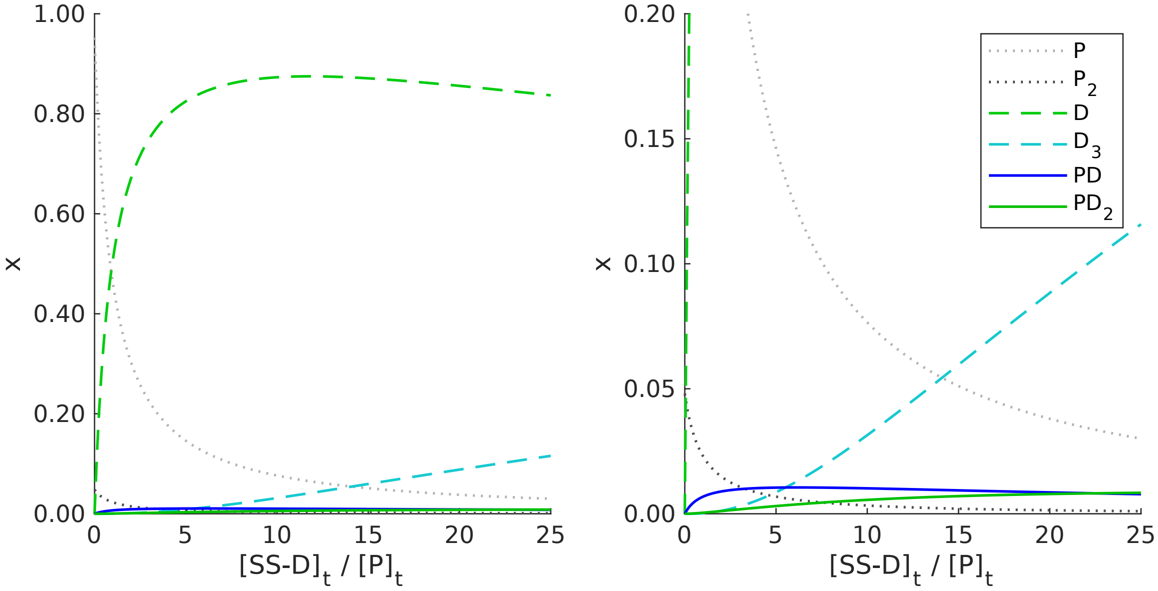

Figure S28: The molar fractions of P, P$_2$, D, D$_3$, PD, and PD$_2$ versus ratio of total concentration of (*S*,*S*)-diol [SS-D]$_t$ and total peptide concentration [P]$_t$ derived by the chemical shift fitting procedure at 300 K. The peptide concentration was kept constant at 2.5 mM. Right: zoom of the bottom 20 % area of the figure to the left.

3.3.11 Peptide-Diol Mixture (EM-PD5)

$$
\begin{aligned}
2\,\mathrm{P} &\xrightleftharpoons{K_1} \mathrm{P_2}\\
3\,\mathrm{D} &\xrightleftharpoons{K_2} \mathrm{D_3}\\
\mathrm{P} + \mathrm{D} &\xrightleftharpoons{K_3} \mathrm{PD}\\
\mathrm{P_2} + \mathrm{D} &\xrightleftharpoons{K_4} \mathrm{P_2D}\\
\mathrm{PD} + \mathrm{D} &\xrightleftharpoons{K_5} \mathrm{PD_2}
\end{aligned}
$$

$$
\frac{\mathrm{d}}{\mathrm{d}t}\begin{pmatrix}[\mathrm{P}]\\ [\mathrm{P_2}]\\ [\mathrm{D}]\\ [\mathrm{D_3}]\\ [\mathrm{PD}]\\ [\mathrm{P_2D}]\\ [\mathrm{PD_2}]\end{pmatrix} = \begin{pmatrix}-2 & 2 & 0 & 0 & -1 & 1 & 0 & 0 & 0 & 0\\ 1 & -1 & 0 & 0 & 0 & 0 & -1 & 1 & 0 & 0\\ 0 & 0 & -3 & 3 & -1 & 1 & -1 & 1 & -1 & 1\\ 0 & 0 & 1 & -1 & 0 & 0 & 0 & 0 & 0 & 0\\ 0 & 0 & 0 & 0 & 1 & -1 & 0 & 0 & -1 & 1\\ 0 & 0 & 0 & 0 & 0 & 0 & 1 & -1 & 0 & 0\\ 0 & 0 & 0 & 0 & 0 & 0 & 0 & 0 & 1 & -1\end{pmatrix} \cdot \begin{pmatrix}k_{1,f}[\mathrm{P}]^2\\ k_{1,b}[\mathrm{P_2}]\\ k_{2,f}[\mathrm{D}]^3\\ k_{2,b}[\mathrm{D_3}]\\ k_{3,f}[\mathrm{P}][\mathrm{D}]\\ k_{3,b}[\mathrm{PD}]\\ k_{4,f}[\mathrm{P_2}][\mathrm{D}]\\ k_{4,b}[\mathrm{P_2D}]\\ k_{5,f}[\mathrm{PD}][\mathrm{D}]\\ k_{5,b}[\mathrm{PD_2}]\end{pmatrix}^T \qquad (37)
$$

Table S20: Best fit solution for mixtures of peptide **1** with both enantiomers of diol **2** at 300 K.

Mixture	**1** + (*R*,*R*)-**2**	**1** + (*S*,*S*)-**2**
RMSD / ppm	9.123×10^{-3}	2.490×10^{-3}
shift violations	6	1
ΔG_1 / kJ mol^{-1}	−10.93	−9.28
ΔG_2 / kJ mol^{-1}	−9.33	−10.88
ΔG_3 / kJ mol^{-1}	−6.44	−5.56
ΔG_4 / kJ mol^{-1}	−8.36	−12.14
ΔG_5 / kJ mol^{-1}	−5.19	−7.90

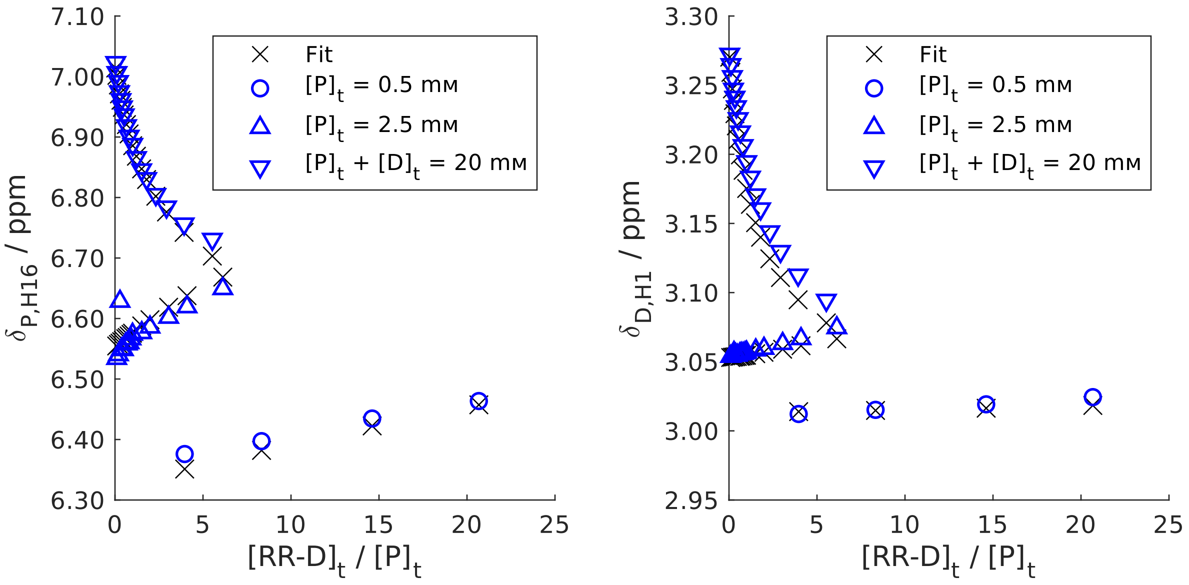

(a) (b)

Figure S29: Fitted chemical shifts versus ratio of total concentration of (*R*,*R*)-diol $[\text{RR-D}]_t$ and total peptide concentration $[\text{P}]_t$ for ${}^{\text{P}}$H16 (left) and ${}^{\text{D}}$H1 (right) by the global chemical shift fitting procedure with equilibrium model EM-PD5 at 300 K.

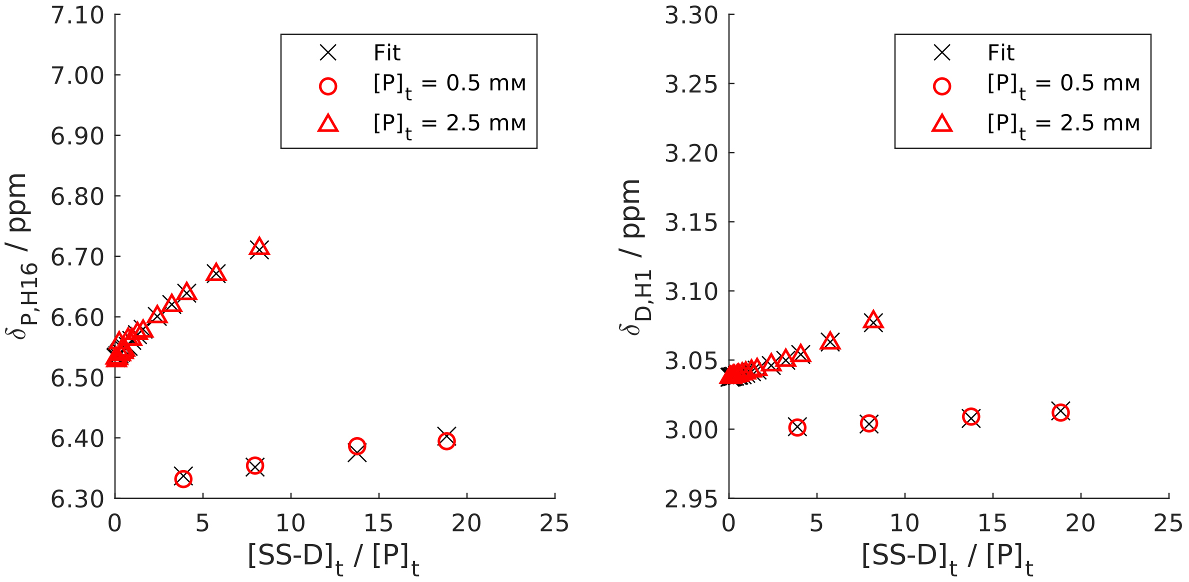

(a) (b)

Figure S30: Fitted chemical shifts versus ratio of total concentration of (*S*,*S*)-diol $[\text{SS-D}]_t$ and total peptide concentration $[\text{P}]_t$ for ${}^{\text{P}}$H16 (left) and ${}^{\text{D}}$H1 (right) by the global chemical shift fitting procedure with equilibrium model EM-PD5 at 300 K.

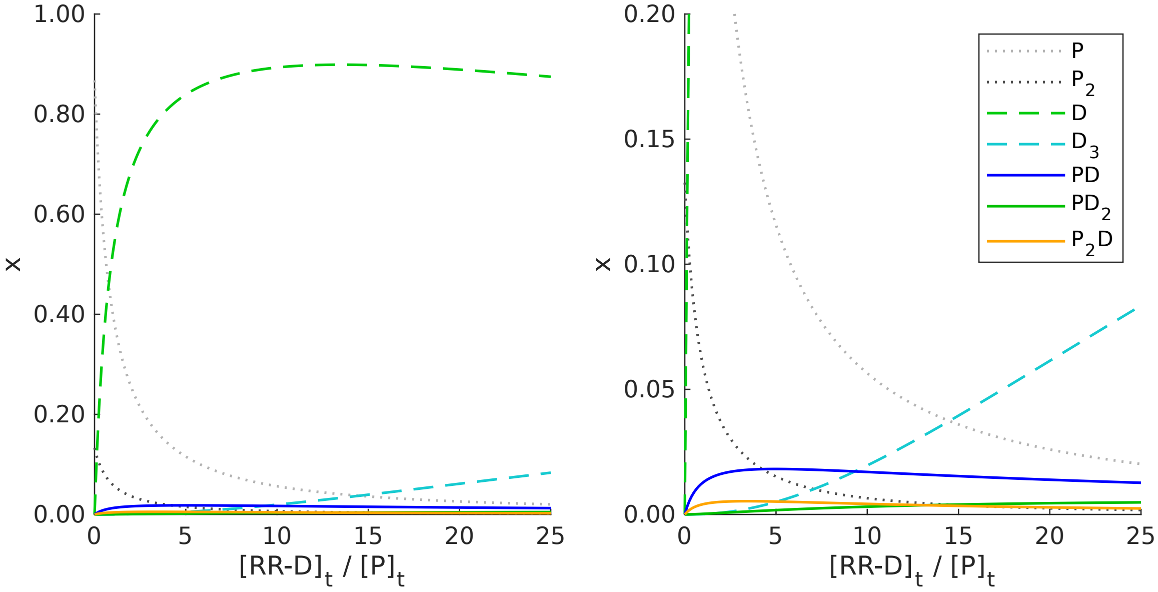

Figure S31: The molar fractions of P, P_2, D, D_3, PD, PD_2, and P_2D versus ratio of total concentration of (*R*,*R*)-diol $[\mathrm{RR\text{-}D}]_t$ and total peptide concentration $[\mathrm{P}]_t$ derived by the chemical shift fitting procedure at 300 K. The peptide concentration was kept constant at 2.5 mM. Right: zoom of the bottom 20 % area of the figure to the left.

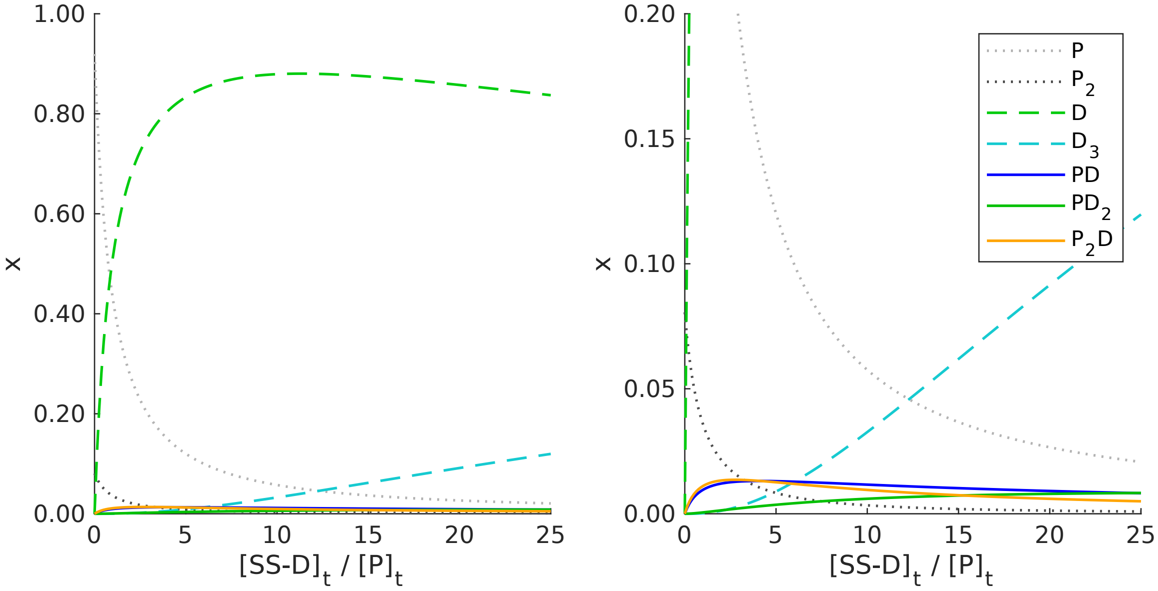

Figure S32: The molar fractions of P, P_2, D, D_3, PD, PD_2, and P_2D versus ratio of total concentration of (*S*,*S*)-diol $[\mathrm{SS\text{-}D}]_t$ and total peptide concentration $[\mathrm{P}]_t$ derived by the chemical shift fitting procedure at 300 K. The peptide concentration was kept constant at 2.5 mM. Right: zoom of the bottom 20 % area of the figure to the left.

3.3.12 Peptide-Diol Mixture (EM-PD6)

$$
\begin{aligned}
2\,\mathrm{P} &\xrightleftharpoons{K_1} \mathrm{P_2}\\
3\,\mathrm{D} &\xrightleftharpoons{K_2} \mathrm{D_3}\\
\mathrm{P} + \mathrm{D} &\xrightleftharpoons{K_3} \mathrm{PD}\\
\mathrm{P_2} + \mathrm{D} &\xrightleftharpoons{K_4} \mathrm{P_2D}\\
\mathrm{P} + \mathrm{D_3} &\xrightleftharpoons{K_6} \mathrm{PD_3}
\end{aligned}
$$

$$
\frac{\mathrm{d}}{\mathrm{d}t}\begin{pmatrix}[\mathrm{P}]\\ [\mathrm{P_2}]\\ [\mathrm{D}]\\ [\mathrm{D_3}]\\ [\mathrm{PD}]\\ [\mathrm{P_2D}]\\ [\mathrm{PD_3}]\end{pmatrix} = \begin{pmatrix}-2 & 2 & 0 & 0 & -1 & 1 & 0 & 0 & -1 & 1\\ 1 & -1 & 0 & 0 & 0 & 0 & -1 & 1 & 0 & 0\\ 0 & 0 & -3 & 3 & -1 & 1 & -1 & 1 & 0 & 0\\ 0 & 0 & 1 & -1 & 0 & 0 & 0 & 0 & -1 & 1\\ 0 & 0 & 0 & 0 & 1 & -1 & 0 & 0 & 0 & 0\\ 0 & 0 & 0 & 0 & 0 & 0 & 1 & -1 & 0 & 0\\ 0 & 0 & 0 & 0 & 0 & 0 & 0 & 0 & 1 & -1\end{pmatrix} \cdot \begin{pmatrix} k_{1,f}[\mathrm{P}]^2\\ k_{1,b}[\mathrm{P_2}]\\ k_{2,f}[\mathrm{D}]^3\\ k_{2,b}[\mathrm{D_3}]\\ k_{3,f}[\mathrm{P}][\mathrm{D}]\\ k_{3,b}[\mathrm{PD}]\\ k_{4,f}[\mathrm{P_2}][\mathrm{D}]\\ k_{4,b}[\mathrm{P_2D}]\\ k_{6,f}[\mathrm{P}][\mathrm{D_3}]\\ k_{6,b}[\mathrm{PD_3}]\end{pmatrix}^T \tag{38}
$$

Table S21: Best fit solution for mixtures of peptide **1** with both enantiomers of diol **2** at 300 K.

Mixture	**1** + (*R*,*R*)-**2**	**1** + (*S*,*S*)-**2**
RMSD / ppm	8.633×10^{-3}	3.994×10^{-3}
shift violations	2	2
ΔG_1 / kJ mol^{-1}	−10.82	−11.33
ΔG_2 / kJ mol^{-1}	−9.49	−9.78
ΔG_3 / kJ mol^{-1}	−7.75	−9.03
ΔG_4 / kJ mol^{-1}	−11.07	−16.65
ΔG_6 / kJ mol^{-1}	−18.78	−18.12

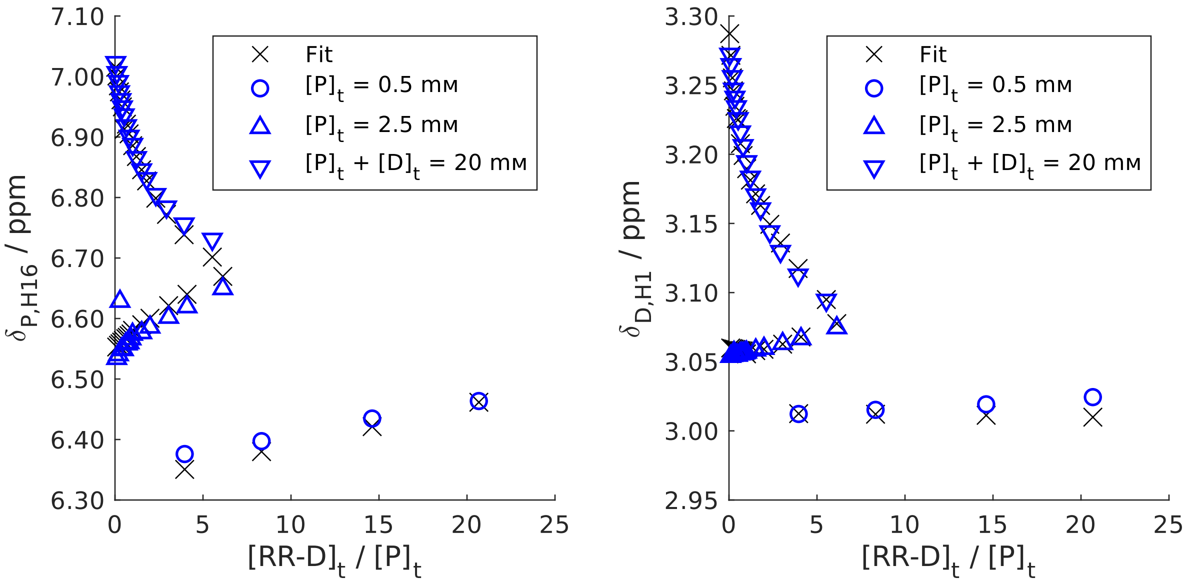

(a) (b)

Figure S33: Fitted chemical shifts versus ratio of total concentration of (*R*,*R*)-diol $[\text{RR-D}]_t$ and total peptide concentration $[\text{P}]_t$ for $^{\text{P}}$H16 (left) and $^{\text{D}}$H1 (right) by the global chemical shift fitting procedure with equilibrium model EM-PD6 at 300 K.

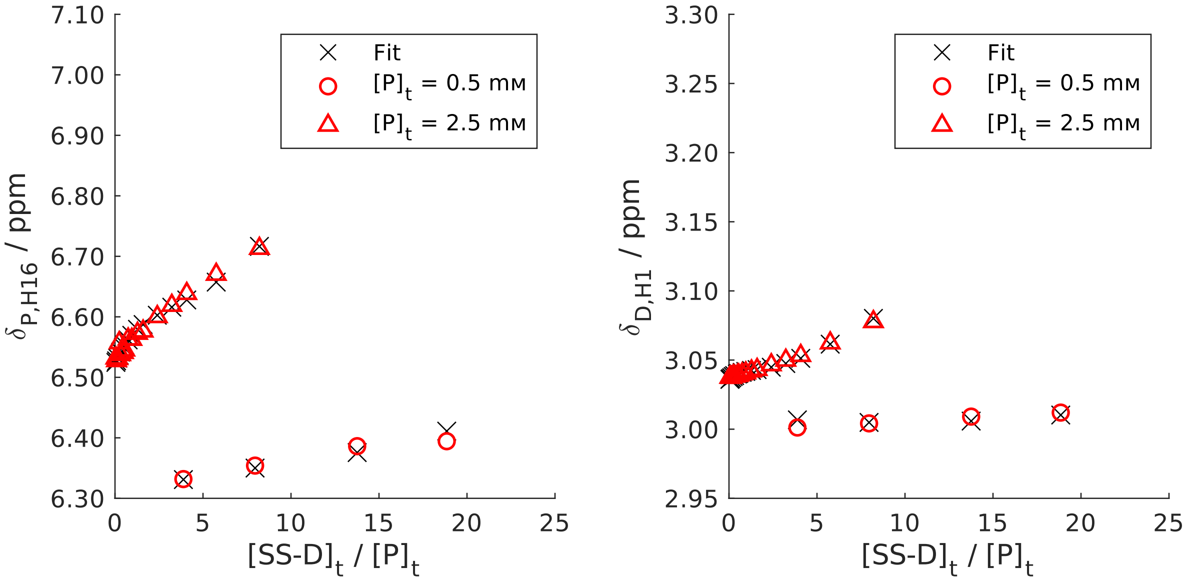

(a) (b)

Figure S34: Fitted chemical shifts versus ratio of total concentration of (*S*,*S*)-diol $[\text{SS-D}]_t$ and total peptide concentration $[\text{P}]_t$ for $^{\text{P}}$H16 (left) and $^{\text{D}}$H1 (right) by the global chemical shift fitting procedure with equilibrium model EM-PD6 at 300 K.

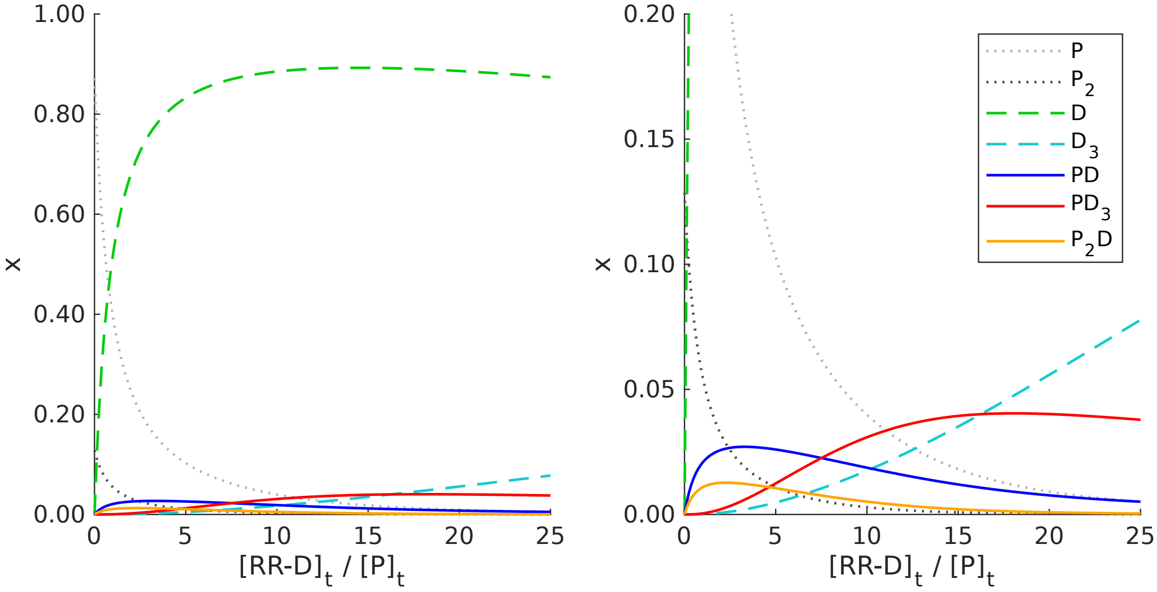

Figure S35: The molar fractions of P, P_2, D, D_3, PD, PD_3, and P_2D versus ratio of total concentration of (*R*,*R*)-diol $[RR\text{-}D]_t$ and total peptide concentration $[P]_t$ derived by the chemical shift fitting procedure at 300 K. The peptide concentration was kept constant at 2.5 mM. Right: zoom of the bottom 20 % area of the figure to the left.

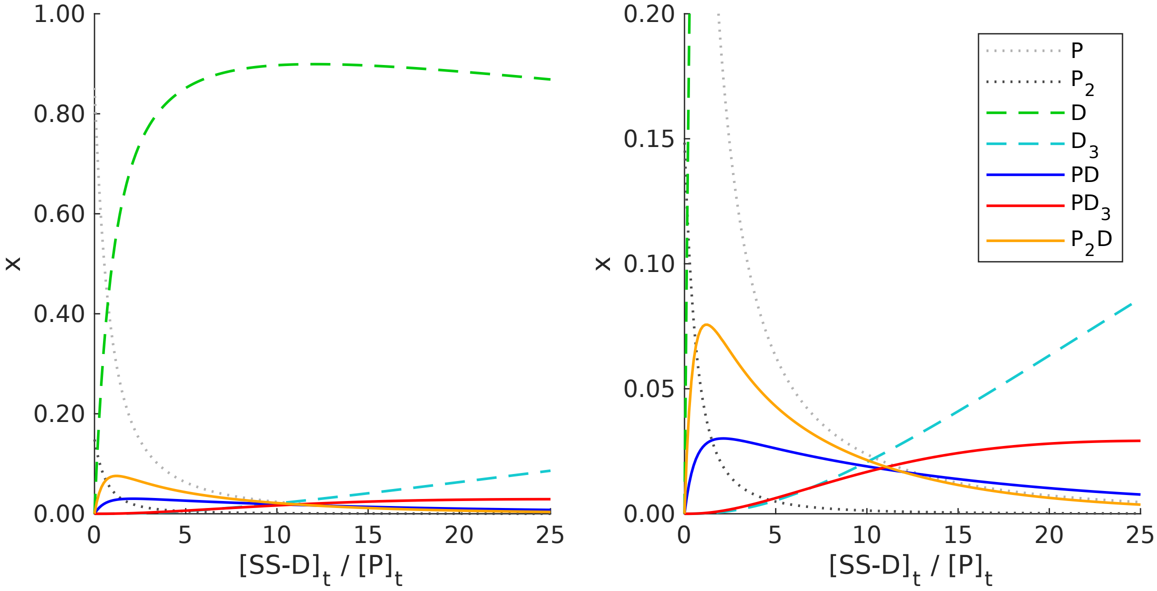

Figure S36: The molar fractions of P, P_2, D, D_3, PD, PD_3, and P_2D versus ratio of total concentration of (*S*,*S*)-diol $[SS\text{-}D]_t$ and total peptide concentration $[P]_t$ derived by the chemical shift fitting procedure at 300 K. The peptide concentration was kept constant at 2.5 mM. Right: zoom of the bottom 20 % area of the figure to the left.

3.3.13 Peptide-Diol Mixture (EM-PD7)

$$2\,\mathrm{P} \overset{K_1}{\rightleftharpoons} \mathrm{P_2}$$
$$3\,\mathrm{D} \overset{K_2}{\rightleftharpoons} \mathrm{D_3}$$
$$\mathrm{P} + \mathrm{D} \overset{K_3}{\rightleftharpoons} \mathrm{PD}$$
$$\mathrm{P_2} + \mathrm{D} \overset{K_4}{\rightleftharpoons} \mathrm{P_2D}$$
$$\mathrm{P_2D} + \mathrm{D} \overset{K_7}{\rightleftharpoons} \mathrm{P_2D_2}$$

$$\frac{\mathrm{d}}{\mathrm{d}t}\begin{pmatrix}[\mathrm{P}]\\ [\mathrm{P_2}]\\ [\mathrm{D}]\\ [\mathrm{D_3}]\\ [\mathrm{PD}]\\ [\mathrm{P_2D}]\\ [\mathrm{P_2D_2}]\end{pmatrix} = \begin{pmatrix} -2 & 2 & 0 & 0 & -1 & 1 & 0 & 0 & 0 & 0\\ 1 & -1 & 0 & 0 & 0 & 0 & -1 & 1 & 0 & 0\\ 0 & 0 & -3 & 3 & -1 & 1 & -1 & 1 & -1 & 1\\ 0 & 0 & 1 & -1 & 0 & 0 & 0 & 0 & 0 & 0\\ 0 & 0 & 0 & 0 & 1 & -1 & 0 & 0 & 0 & 0\\ 0 & 0 & 0 & 0 & 0 & 0 & 1 & -1 & -1 & 1\\ 0 & 0 & 0 & 0 & 0 & 0 & 0 & 0 & 1 & -1 \end{pmatrix} \cdot \begin{pmatrix} k_{1,f}[\mathrm{P}]^2\\ k_{1,b}[\mathrm{P_2}]\\ k_{2,f}[\mathrm{D}]^3\\ k_{2,b}[\mathrm{D_3}]\\ k_{3,f}[\mathrm{P}][\mathrm{D}]\\ k_{3,b}[\mathrm{PD}]\\ k_{4,f}[\mathrm{P_2}][\mathrm{D}]\\ k_{4,b}[\mathrm{P_2D}]\\ k_{7,f}[\mathrm{P_2D}][\mathrm{D}]\\ k_{7,b}[\mathrm{P_2D_2}] \end{pmatrix}^T \tag{39}$$

Table S22: Best fit solution for mixtures of peptide **1** with both enantiomers of diol **2** at 300 K.

Mixture	**1** + (*R*,*R*)-**2**	**1** + (*S*,*S*)-**2**
RMSD / ppm	8.593×10^{-3}	2.405×10^{-3}
shift violations	0	1
ΔG_1 / kJ mol^{-1}	−11.07	−11.11
ΔG_2 / kJ mol^{-1}	−13.10	−9.50
ΔG_3 / kJ mol^{-1}	−9.89	−8.10
ΔG_4 / kJ mol^{-1}	−10.31	−11.80
ΔG_7 / kJ mol^{-1}	−10.41	−8.65

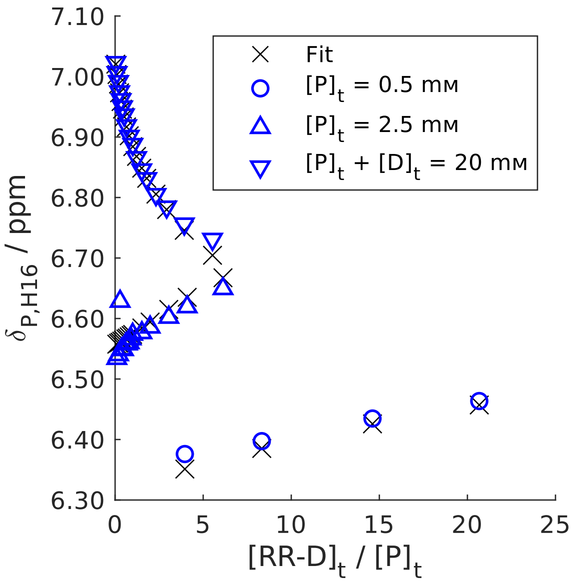

(a) (b)

Figure S37: Fitted chemical shifts versus ratio of total concentration of (*R*,*R*)-diol $[RR\text{-}D]_t$ and total peptide concentration $[P]_t$ for ^{P}H16 (left) and ^{D}H1 (right) by the global chemical shift fitting procedure with equilibrium model EM-PD7 at 300 K.

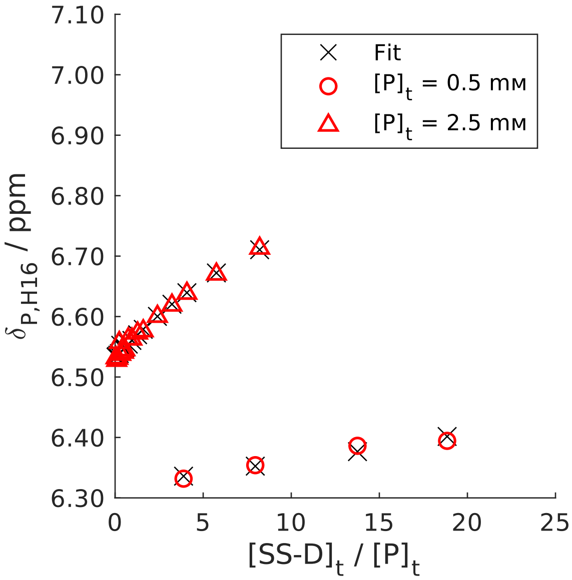

(a) (b)

Figure S38: Fitted chemical shifts versus ratio of total concentration of (*S*,*S*)-diol $[SS\text{-}D]_t$ and total peptide concentration $[P]_t$ for ^{P}H16 (left) and ^{D}H1 (right) by the global chemical shift fitting procedure with equilibrium model EM-PD7 at 300 K.

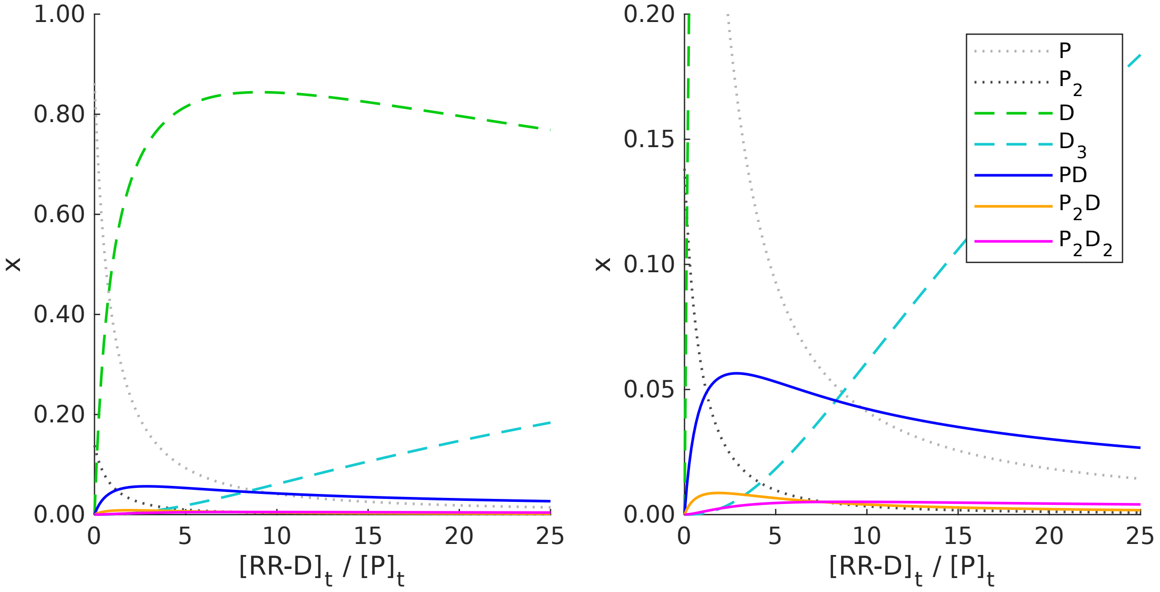

Figure S39: The molar fractions of P, P_2, D, D_3, PD, PD_2, P_2D, and P_2D_2 versus ratio of total concentration of (*R*,*R*)-diol $[\text{RR-D}]_t$ and total peptide concentration $[\text{P}]_t$ derived by the chemical shift fitting procedure at 300 K. The peptide concentration was kept constant at 2.5 mM. Right: zoom of the bottom 20 % area of the figure to the left.

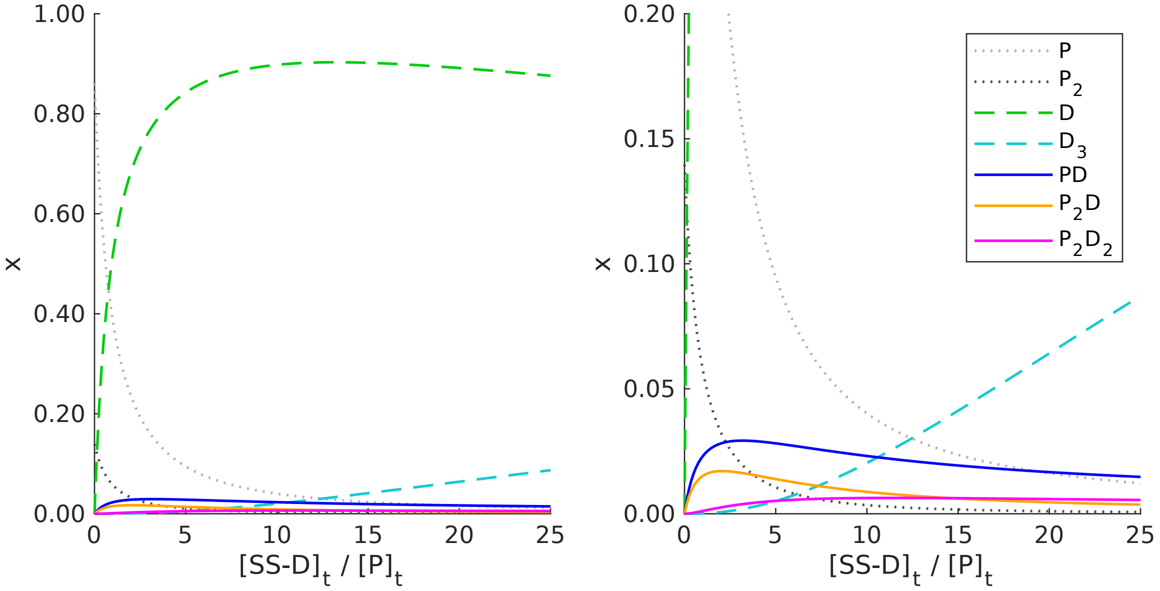

Figure S40: The molar fractions of P, P_2, D, D_3, PD, PD_2, P_2D, and P_2D_2 versus ratio of total concentration of (*S*,*S*)-diol $[\text{SS-D}]_t$ and total peptide concentration $[\text{P}]_t$ derived by the chemical shift fitting procedure at 300 K. The peptide concentration was kept constant at 2.5 mM. Right: zoom of the bottom 20 % area of the figure to the left.

3.3.14 Peptide-Diol Mixture (EM-PD8)

$$2\,\mathrm{P} \xrightleftharpoons{K_1} \mathrm{P_2}$$
$$3\,\mathrm{D} \xrightleftharpoons{K_2} \mathrm{D_3}$$
$$\mathrm{P} + \mathrm{D} \xrightleftharpoons{K_3} \mathrm{PD}$$
$$\mathrm{P_2} + \mathrm{D} \xrightleftharpoons{K_4} \mathrm{P_2D}$$
$$\mathrm{PD} + \mathrm{D} \xrightleftharpoons{K_5} \mathrm{PD_2}$$
$$\mathrm{P_2D} + \mathrm{D} \xrightleftharpoons{K_7} \mathrm{P_2D_2}$$

$$\frac{\mathrm{d}}{\mathrm{d}t}\begin{pmatrix}[\mathrm{P}]\\ [\mathrm{P_2}]\\ [\mathrm{D}]\\ [\mathrm{D_3}]\\ [\mathrm{PD}]\\ [\mathrm{P_2D}]\\ [\mathrm{PD_2}]\\ [\mathrm{P_2D_2}]\end{pmatrix} = \begin{pmatrix} -2 & 2 & 0 & 0 & -1 & 1 & 0 & 0 & 0 & 0 & 0 & 0\\ 1 & -1 & 0 & 0 & 0 & 0 & -1 & 1 & 0 & 0 & 0 & 0\\ 0 & 0 & -3 & 3 & -1 & 1 & -1 & 1 & -1 & 1 & -1 & 1\\ 0 & 0 & 1 & -1 & 0 & 0 & 0 & 0 & 0 & 0 & 0 & 0\\ 0 & 0 & 0 & 0 & 1 & -1 & 0 & 0 & -1 & 1 & 0 & 0\\ 0 & 0 & 0 & 0 & 0 & 0 & 1 & -1 & 0 & 0 & -1 & 1\\ 0 & 0 & 0 & 0 & 0 & 0 & 0 & 0 & 1 & -1 & 0 & 0\\ 0 & 0 & 0 & 0 & 0 & 0 & 0 & 0 & 0 & 0 & 1 & -1 \end{pmatrix} \cdot \begin{pmatrix} k_{1,f}[\mathrm{P}]^2\\ k_{1,b}[\mathrm{P_2}]\\ k_{2,f}[\mathrm{D}]^3\\ k_{2,b}[\mathrm{D_3}]\\ k_{3,f}[\mathrm{P}][\mathrm{D}]\\ k_{3,b}[\mathrm{PD}]\\ k_{4,f}[\mathrm{D}][\mathrm{P_2}]\\ k_{4,b}[\mathrm{P_2D}]\\ k_{5,f}[\mathrm{D}][\mathrm{PD}]\\ k_{5,b}[\mathrm{PD_2}]\\ k_{7,f}[\mathrm{D}][\mathrm{P_2D}]\\ k_{7,b}[\mathrm{P_2D_2}] \end{pmatrix}^{T} \tag{40}$$

Table S23: Best fit solution for mixtures of peptide **1** with both enantiomers of diol **2** at 300 K.

Mixture	**1** + (*R*,*R*)-**2**	**1** + (*S*,*S*)-**2**
RMSD / ppm	6.487×10^{-3}	2.124×10^{-3}
shift violations	0	0
ΔG_1 / kJ mol^{-1}	−10.79	−11.42
ΔG_2 / kJ mol^{-1}	−9.17	−9.20
ΔG_3 / kJ mol^{-1}	−14.62	−11.31
ΔG_4 / kJ mol^{-1}	−16.84	−19.50
ΔG_5 / kJ mol^{-1}	−4.93	−6.31
ΔG_7 / kJ mol^{-1}	−12.41	−5.99

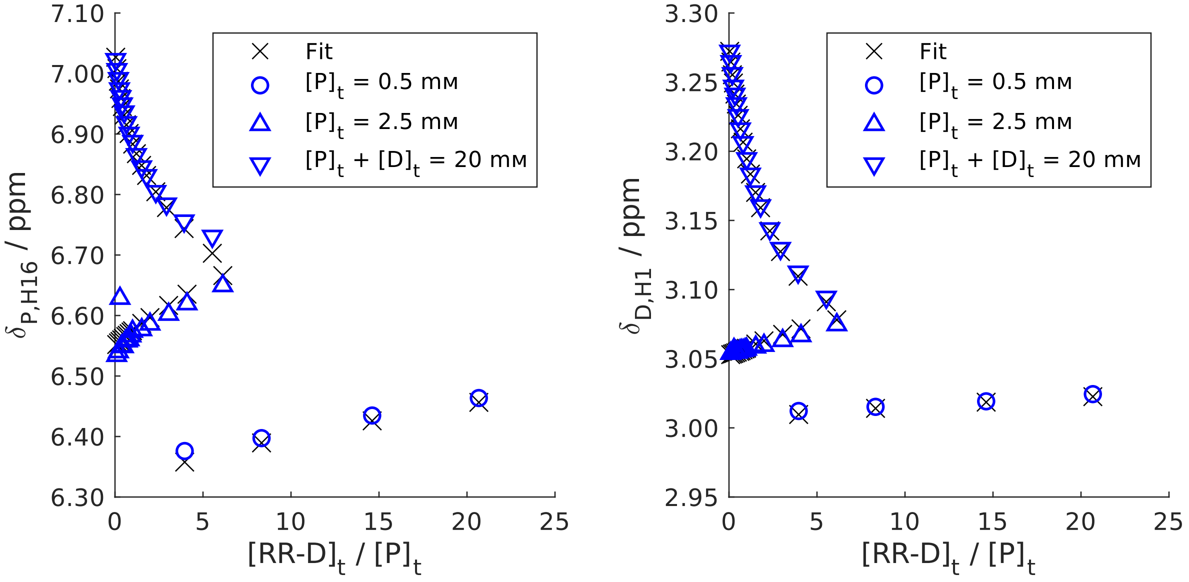

(a) (b)

Figure S41: Fitted chemical shifts versus ratio of total concentration of (*R*,*R*)-diol $[\text{RR-D}]_t$ and total peptide concentration $[\text{P}]_t$ for $^{\text{P}}$H16 (left) and $^{\text{D}}$H1 (right) by the global chemical shift fitting procedure with equilibrium model EM-PD8 at 300 K.

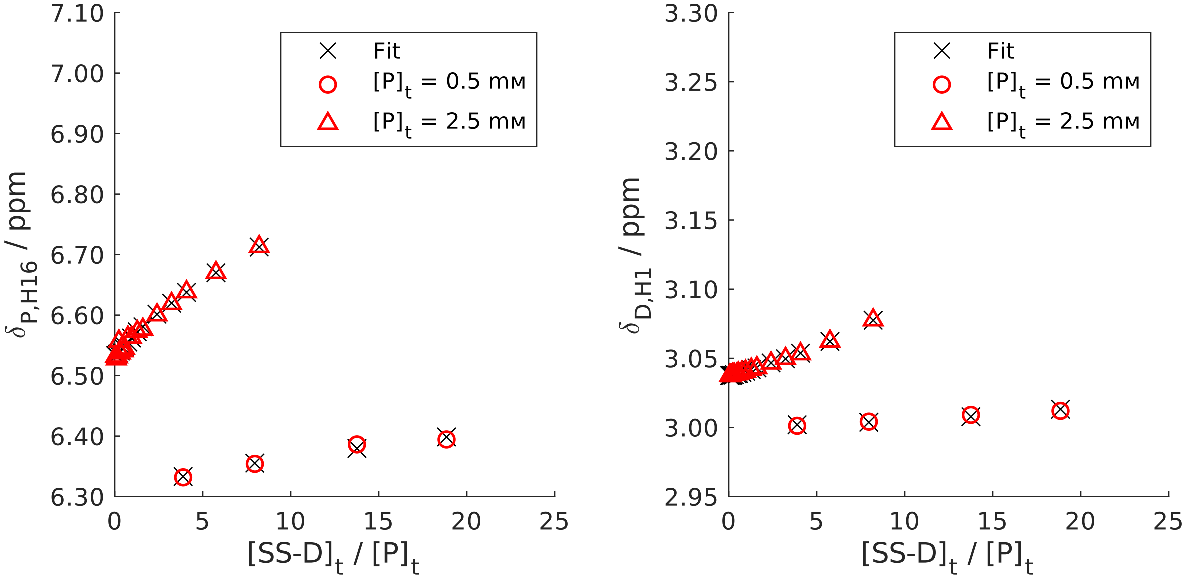

(a) (b)

Figure S42: Fitted chemical shifts versus ratio of total concentration of (*S*,*S*)-diol $[\text{SS-D}]_t$ and total peptide concentration $[\text{P}]_t$ for $^{\text{P}}$H16 (left) and $^{\text{D}}$H1 (right) by the global chemical shift fitting procedure with equilibrium model EM-PD8 at 300 K.

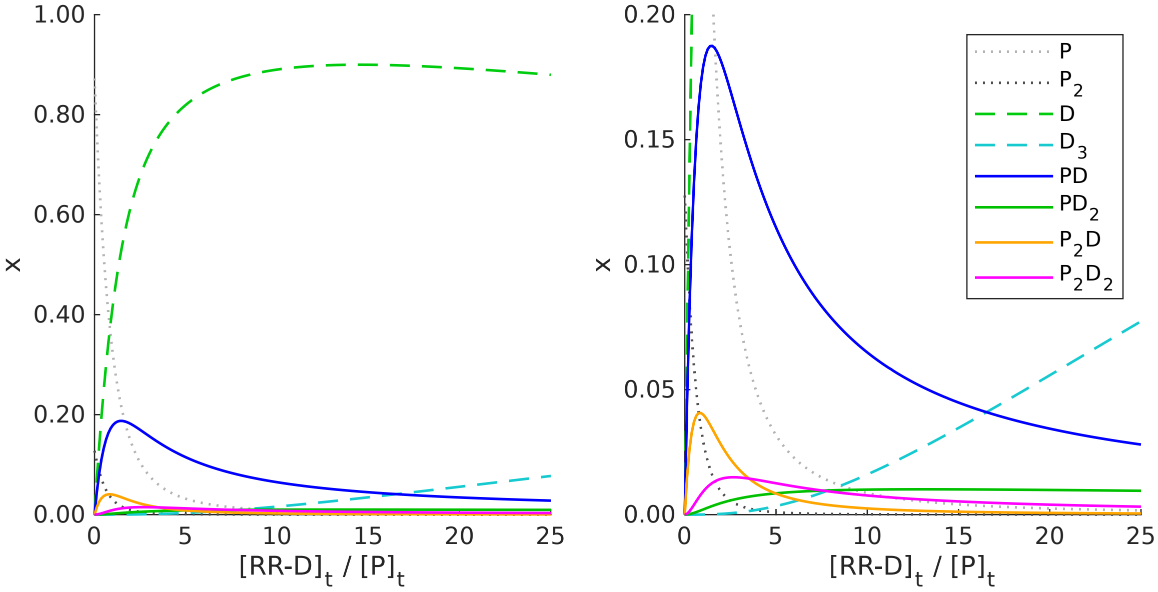

Figure S43: The molar fractions of P, P$_2$, D, D$_3$, PD, PD$_2$, P$_2$D, and P$_2$D$_2$ versus ratio of total concentration of (*R*,*R*)-diol [RR-D]$_t$ and total peptide concentration [P]$_t$ derived by the chemical shift fitting procedure at 300 K. The peptide concentration was kept constant at 2.5 mM. Right: zoom of the bottom 20 % area of the figure to the left.

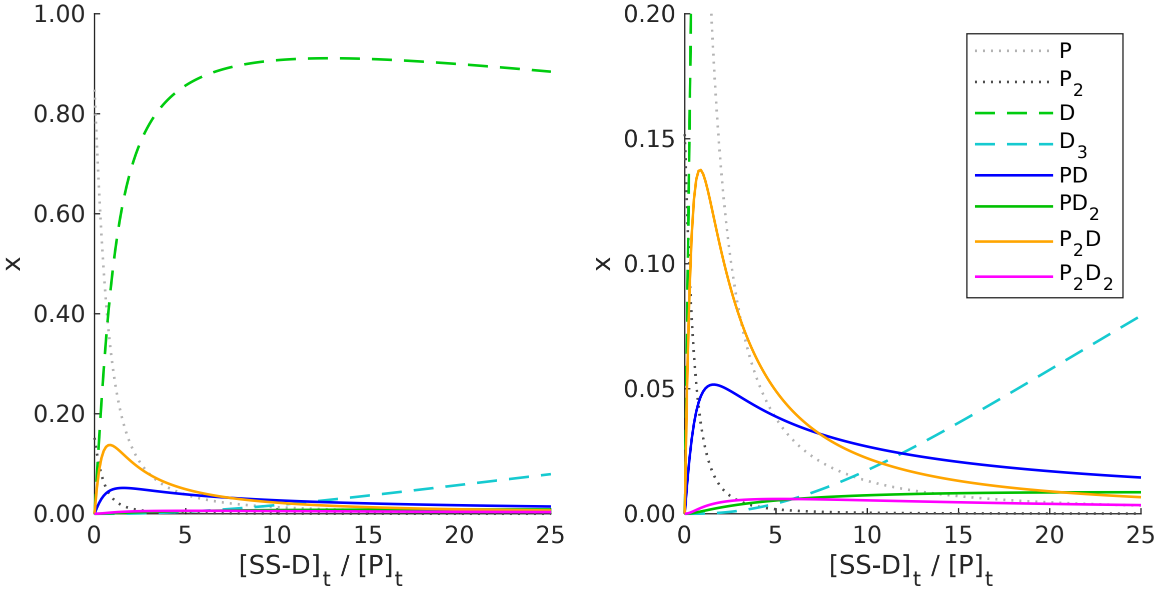

Figure S44: The molar fractions of P, P$_2$, D, D$_3$, PD, PD$_2$, P$_2$D, and P$_2$D$_2$ versus ratio of total concentration of (*S*,*S*)-diol [SS-D]$_t$ and total peptide concentration [P]$_t$ derived by the chemical shift fitting procedure at 300 K. The peptide concentration was kept constant at 2.5 mM. Right: zoom of the bottom 20 % area of the figure to the left.

3.3.15 Peptide-Diol Mixture (EM-PD9)

$$
\begin{aligned}
2\,\mathrm{P} &\xrightleftharpoons{K_1} \mathrm{P_2}\\
3\,\mathrm{D} &\xrightleftharpoons{K_2} \mathrm{D_3}\\
\mathrm{P} + \mathrm{D} &\xrightleftharpoons{K_3} \mathrm{PD}\\
\mathrm{P_2} + \mathrm{D} &\xrightleftharpoons{K_4} \mathrm{P_2D}\\
\mathrm{P} + \mathrm{D_3} &\xrightleftharpoons{K_6} \mathrm{PD_3}\\
\mathrm{P_2D} + \mathrm{D} &\xrightleftharpoons{K_7} \mathrm{P_2D_2}
\end{aligned}
$$

$$
\frac{\mathrm{d}}{\mathrm{d}t}\begin{pmatrix}[\mathrm{P}]\\ [\mathrm{P_2}]\\ [\mathrm{D}]\\ [\mathrm{D_3}]\\ [\mathrm{PD}]\\ [\mathrm{P_2D}]\\ [\mathrm{PD_3}]\\ [\mathrm{P_2D_2}]\end{pmatrix} = \begin{pmatrix} -2 & 2 & 0 & 0 & -1 & 1 & 0 & 0 & -1 & 1 & 0 & 0\\ 1 & -1 & 0 & 0 & 0 & 0 & -1 & 1 & 0 & 0 & 0 & 0\\ 0 & 0 & -3 & 3 & -1 & 1 & -1 & 1 & 0 & 0 & -1 & 1\\ 0 & 0 & 1 & -1 & 0 & 0 & 0 & 0 & -1 & 1 & 0 & 0\\ 0 & 0 & 0 & 0 & 1 & -1 & 0 & 0 & 0 & 0 & 0 & 0\\ 0 & 0 & 0 & 0 & 0 & 0 & 1 & -1 & 0 & 0 & -1 & 1\\ 0 & 0 & 0 & 0 & 0 & 0 & 0 & 0 & 1 & -1 & 0 & 0\\ 0 & 0 & 0 & 0 & 0 & 0 & 0 & 0 & 0 & 0 & 1 & -1 \end{pmatrix} \cdot \begin{pmatrix} k_{1,f}[\mathrm{P}]^2\\ k_{1,b}[\mathrm{P_2}]\\ k_{2,f}[\mathrm{D}]^3\\ k_{2,b}[\mathrm{D_3}]\\ k_{3,f}[\mathrm{P}][\mathrm{D}]\\ k_{3,b}[\mathrm{PD}]\\ k_{4,f}[\mathrm{P_2}][\mathrm{D}]\\ k_{4,b}[\mathrm{P_2D}]\\ k_{6,f}[\mathrm{P}][\mathrm{D_3}]\\ k_{6,b}[\mathrm{PD_3}]\\ k_{7,f}[\mathrm{P_2D}][\mathrm{D}]\\ k_{7,b}[\mathrm{P_2D_2}] \end{pmatrix}^T \tag{41}
$$

Table S24: Best fit solution for mixtures of peptide **1** with both enantiomers of diol **2** at 300 K.

Mixture	**1** + (*R*,*R*)-**2**	**1** + (*S*,*S*)-**2**
RMSD / ppm	9.477×10^{-3}	2.125×10^{-3}
shift violations	10	0
ΔG_1 / kJ mol^{-1}	−11.08	−11.05
ΔG_2 / kJ mol^{-1}	−9.26	−9.18
ΔG_3 / kJ mol^{-1}	−8.69	−12.27
ΔG_4 / kJ mol^{-1}	−5.32	−16.13
ΔG_6 / kJ mol^{-1}	−10.84	−15.82
ΔG_7 / kJ mol^{-1}	−15.06	−8.19

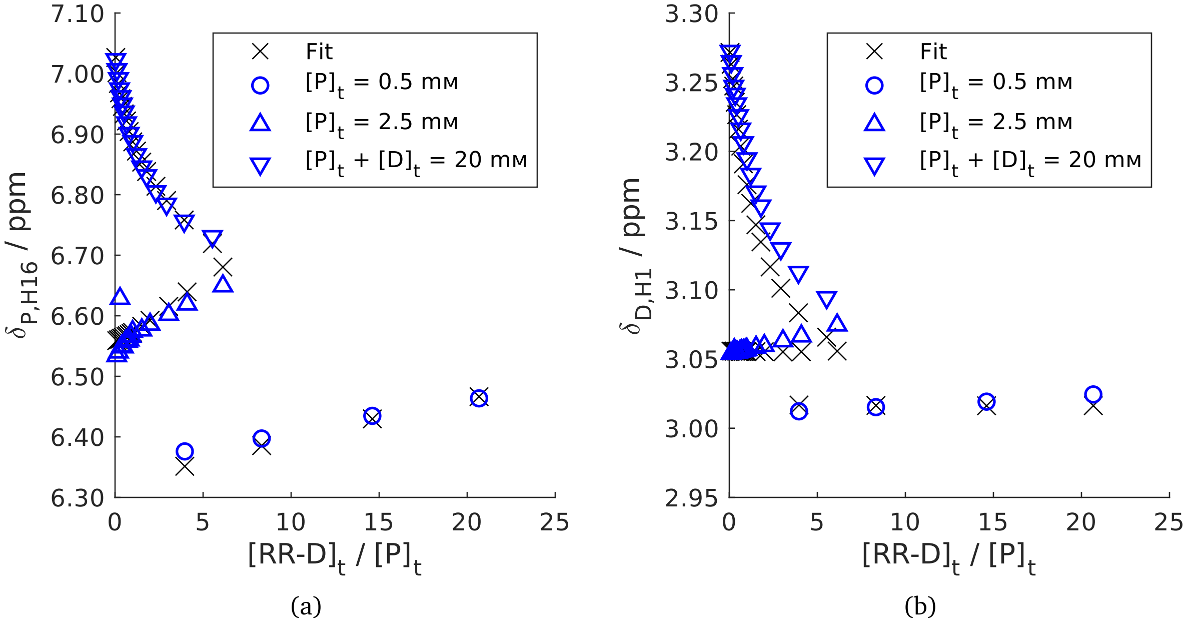

(a) (b)

Figure S45: Fitted chemical shifts versus ratio of total concentration of (*R*,*R*)-diol $[RR\text{-}D]_t$ and total peptide concentration $[P]_t$ for ^{P}H16 (left) and ^{D}H1 (right) by the global chemical shift fitting procedure with equilibrium model EM-PD9 at 300 K.

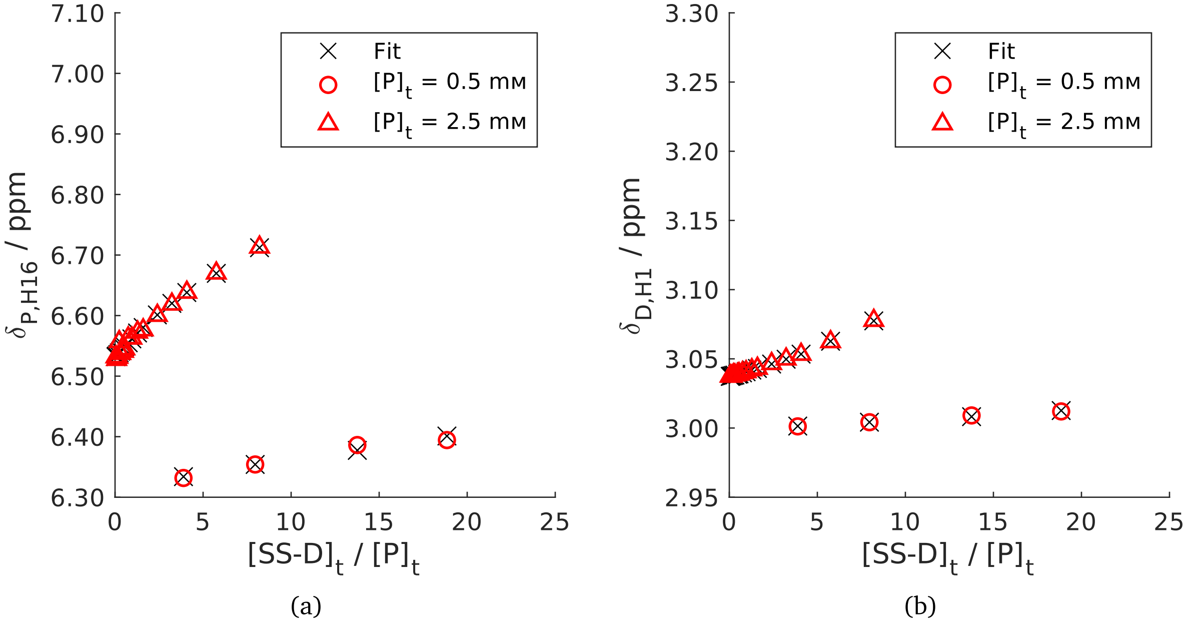

(a) (b)

Figure S46: Fitted chemical shifts versus ratio of total concentration of (*S*,*S*)-diol $[SS\text{-}D]_t$ and total peptide concentration $[P]_t$ for ^{P}H16 (left) and ^{D}H1 (right) by the global chemical shift fitting procedure with equilibrium model EM-PD9 at 300 K.

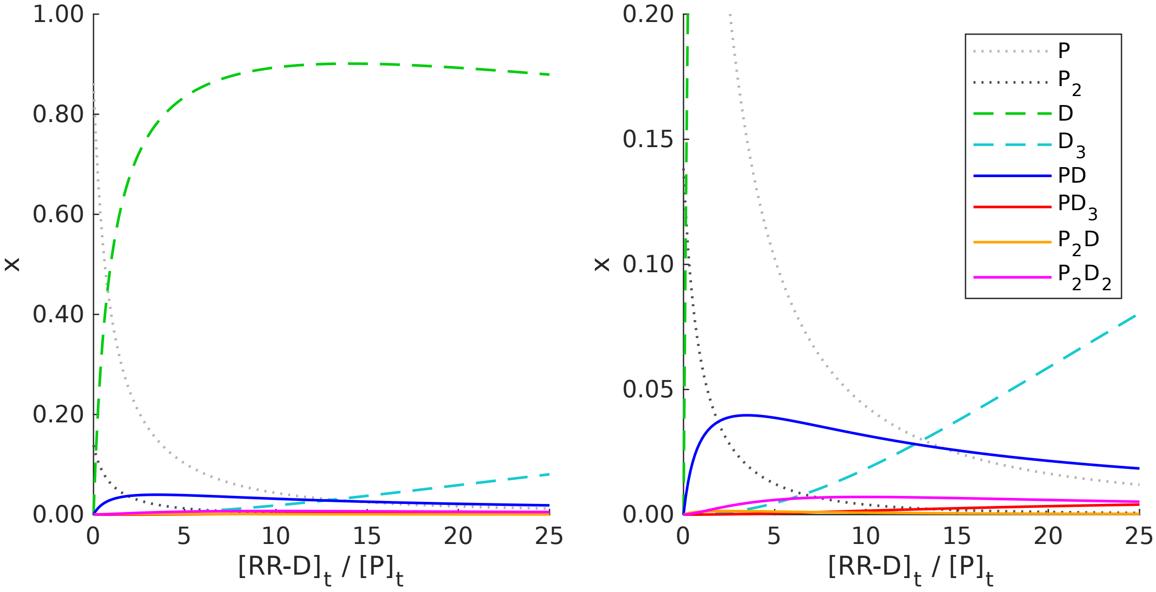

Figure S47: The molar fractions of P, P_2, D, D_3, PD, PD_3, P_2D, and P_2D_2 versus ratio of total concentration of (*R*,*R*)-diol $[\mathrm{RR\text{-}D}]_t$ and total peptide concentration $[\mathrm{P}]_t$ derived by the chemical shift fitting procedure at 300 K. The peptide concentration was kept constant at 2.5 mM. Right: zoom of the bottom 20 % area of the figure to the left.

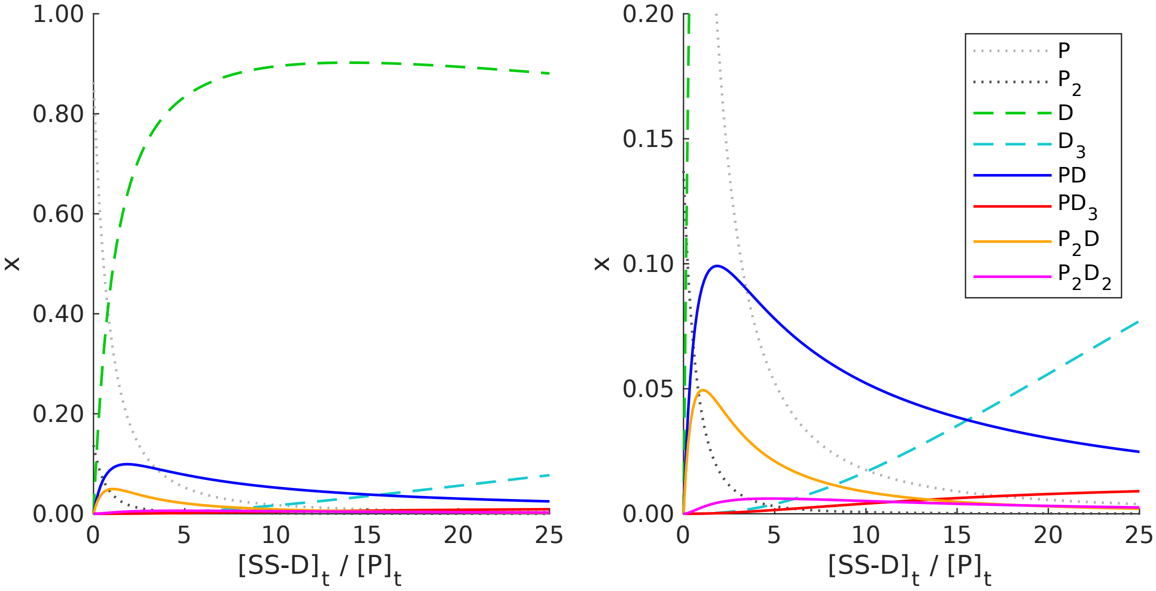

Figure S48: The molar fractions of P, P_2, D, D_3, PD, PD_3, P_2D, and P_2D_2 versus ratio of total concentration of (*S*,*S*)-diol $[\mathrm{SS\text{-}D}]_t$ and total peptide concentration $[\mathrm{P}]_t$ derived by the chemical shift fitting procedure at 300 K. The peptide concentration was kept constant at 2.5 mM. Right: zoom of the bottom 20 % area of the figure to the left.

4 Diffusion Coefficient Peptide 1

Pulsed Field Gradient NMR with Spin Echos or Stimulated Echos allows the measurement of the molecular self-diffusion coefficient D.[35–37] The Stokes-Einstein equation[38] (Equation 42) connects the diffusion coefficient with the size of a sphere with a hydrodynamic radius r_h. Furthermore, D depends on the absolute temperature T, viscosity of the solvent η, and k_b (Boltzmann constant).

$$D = \frac{k_b T}{6\pi\eta r_h} \tag{42}$$

Thus, the diffusion coefficient is a direct reporter of the size on the diffusing species. Equation 42 is strictly valid for spherical particles, but also qualitatively applies to non-spherical behavior. Molecules, that occupy a larger hydrodynamic volume, exhibit a smaller diffusion coefficient than smaller molecules. Additionally, effects like association affect the value observed (see section 4.2 for mathematical description of diffusion within the isodesmic model). Upon aggregation or binding a compound increases in size and thus it diffuses slower as long as it is the bound state. In the case of fast exchange, the binding event happens several times during the NMR experiment, resulting in an averaged observable. The magnitude of the D-value gives an indication of the location of the equilibrium.

The NMR experiment used herein employed z-gradients with increasing gradient strength. According to the modified Stejskal-Tanner equation[21,36] (Equation 43) to account for the chosen type of pulse sequence and gradient shapes (`SMSQ10.100`), the signal intensity $I(g)$ experiences an attenuation on increasing gradient strengths g. The diffusion coefficient D was obtained by a linear fit. Apart from the initial intensity I_0, the other quantities are either constants or known parameters, where γ_H is the gyromagnetic ratio for protons, δ is the pulsed field-gradient duration for diffusion en- and decoding, Δ is the diffusion time, and τ_1 and τ_2 are time spans defined by the pulse sequence (see Figure S49). The intergradient delay τ_1 includes the duration of a 180° pulse and the gradient recovery delay d_{16}, while the delay τ_2 only equals d_{16}. Note that δ is not to be confused with chemical shifts in other sections.

$$I(g) = I_0 \exp\left(-g^2\gamma_H^2\delta^2 D \frac{81}{100}\left[\Delta - \frac{6344\pi^2 - 207}{9720\pi^2}\delta - \frac{\tau_1 + \tau_2}{2}\right]\right) \tag{43}$$

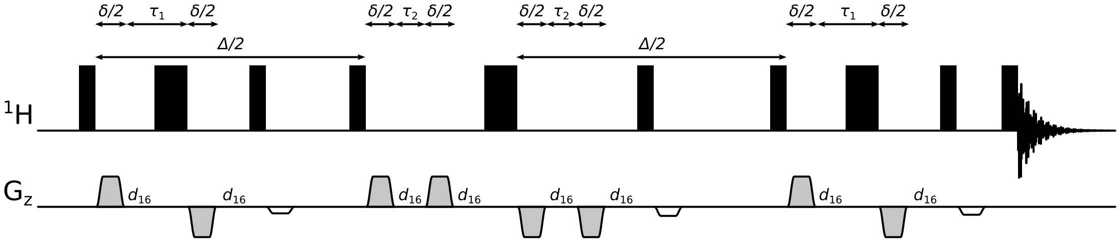

Figure S49: Graphical depiction of the `dstebpgp3s` pulse sequence[11,21] used herein. Narrow and wide rectangles represent hard 90° and 180° pulses, respectively. The gradients relevant for the definition of both intergradient delays τ_1 and τ_2 are shaded in grey, while the white gradients are spoil gradients.

The diffusion coefficient of peptide **1** was extracted from the integrated intensities of the methoxy group $^{\mathrm{P}}$H1, as it is an isolated, well-separated signal and not prone to chemical exchange. A further advantage is that the signal is a singlet and 3 protons contribute to it, making integration less error-prone. The attenuated signal fits well with the single Gaussian decay as given in Equation 43, being in line with an averaged diffusion coefficient over all associating species. An exemplary decay is shown in Figure S50 with the used and extracted parameters in Table S25. All other attenuation curves behave accordingly, regardless of whether *trans*-cyclohexane-1,2-diol (**2**) is present or not.

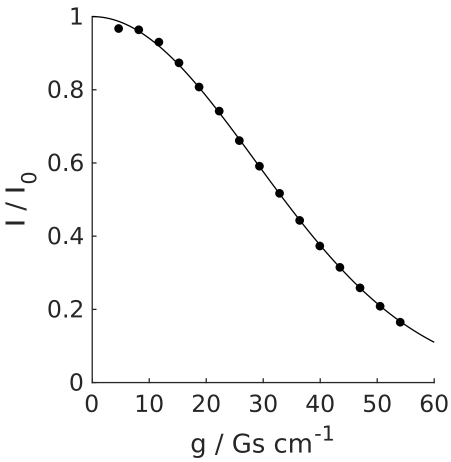

Figure S50: Gaussian decay function (Equation 43) fitted against the measured signal attenuation of methoxy group ^{P}H1 in 0.52 mM peptide **1** at 300 K (jn-122). The corresponding experimental conditions are given in Table S25.

Table S25: Fitparameter for the fit of the measured signal attenuation of methoxy group ^{P}H1 in 0.52 mM peptide **1** at 300 K (jn-122) in Figure S50.

quantity	value
Δ / ms	50
δ / ms	2
τ_1 / µs	213.85
τ_2 / µs	200
D_P / 10^{-10} m^2 s^{-1}	5.45 ± 0.10
I_0 / 10^5	7.788 ± 0.059

4.1 Estimation of Monomeric Peptide Diffusion

To get an estimate how large the diffusion coefficient of monomeric peptide (D_P) of catalyst **1** would be, we consult Equation 44.[39]

$$D = K\,M^{\alpha} \tag{44}$$

Here, M is the molecular weight, K is a compound specific constant, and α depends highly on the shape of the particle. K and α are empirically determined parameters. Based on Reference 39, we classified the shape of peptide **1** as dissipated sphere and ellipsoid, for which the calibration curve in toluene-d_8 has the parameters $K = 10^{-7.5197}$ and $\alpha = -0.6098$.[39] With the molecular weight of $M = 760.98\,\mathrm{g\,mol^{-1}}$ the diffusion coefficient of monomeric **1** at 298 K is predicted to be $D_P = (5.29 \pm 0.48) \times 10^{-10}\,\mathrm{m^2\,s^{-1}}$. It follows from the Stokes-Einstein relation (Equation 42) that $r_h = (7.48 \pm 0.74)\,\text{Å}$. For this a dynamic viscosity of $\eta = 0.553\,\mathrm{mPa\,s}$ was calculated for toluene-d_0 from Equation 45 with the corresponding parameters a to e in Table S26.[40]

$$\eta = e \cdot \exp\left[a\left(\frac{c-T}{T-d}\right)^{1/3} + b\left(\frac{c-T}{T-d}\right)^{4/3}\right] \tag{45}$$

Table S26: Coefficients for the temperature dependent calculation of dynamic viscosity η of toluene-d_0 with Equation 45 taken from Reference 40.

parameter	value	
a / K$^{-1/3}$	2.954 80	
b / K$^{-4/3}$	3.0	× 10^{-5}
c / K	1048.107	
d / K	137.144	
e / Pa s	3.97	× 10^{-6}

Table S27 gives an overview of the temperature dependency of the diffusion coefficient utilizing Eqs. 42 and 45 for selected temperatures under the assumption that the hydrodynamic radius of the diffusing species is constant. This leads to relation 46.

$$D(T_2) = D(T_1)\,\frac{T_2}{T_1}\,\frac{\eta(T_1)}{\eta(T_2)} \tag{46}$$

Table S27: Estimated diffusion coefficients of monomeric peptide **1** at selected temperatures obtained with Eqs. 44, 45, and 46.

T / K	η / mPa s	D_P / $10^{-10}\,\mathrm{m^2\,s^{-1}}$
270	0.817	3.24
275	0.757	3.56
280	0.703	3.90
285	0.655	4.26
290	0.613	4.63
295	0.574	5.03
298	0.553	5.29
300	0.540	5.44

The monomeric peptide diffusion coefficient would be theoretically measurable at infinite dilution. So, in a first approximation, the measurements at low concentrations are comparable to the values of the monomeric peptide diffusion coefficient. The predicted value $D_\mathrm{P} = (5.44 \pm 0.49) \times 10^{-10}\,\mathrm{m^2\,s^{-1}}$ matches the measured value $D_\mathrm{P} = (5.45 \pm 0.10) \times 10^{-10}\,\mathrm{m^2\,s^{-1}}$ of 0.52 mM peptide **1** at 300 K very well. But with lower temperatures the self-association dominates the diffusion coefficient and the discrepancy between prediction and measurement grows. Therefore, the value of the diffusion coefficient $D_\mathrm{P} = (2.84 \pm 0.02) \times 10^{-10}\,\mathrm{m^2\,s^{-1}}$ of the same sample at 270 K is lower than the predicted one for the monomeric species $D_\mathrm{P} = (3.24 \pm 0.29) \times 10^{-10}\,\mathrm{m^2\,s^{-1}}$. As all NMR observables, the measured values of the diffusion coefficient needs to be treated in the context of self-association as done in the next section.

4.2 Oligomeric Peptide Diffusion within the Isodesmic Model

Following the isodesmic model, low peptide concentrations and high temperatures approximate a condition where higher oligomers are disfavored and the peptide is present mainly in a monomeric form. The experimental diffusion coefficient at these conditions should therefore more closely resemble the values predicted for the monomeric species in the section above. For these conditions higher concentrations lead to a higher number of oligomers formed, which exhibit lower diffusion coefficients due to their increased molecular volumes. For the description of the concentration dependent diffusion coefficients of peptide catalyst **1** we employed the procedure from Reference 41, but without considering additional crowding effects. As the Stokes-Einstein relation (Equation 42) is only valid for diffusing spheres, Equation 47 also implies spherical behaviour of all i-mers. Therefore, every additional monomer increases the diffusion coefficient only by a factor to the power of $-\frac{1}{3}$. Additionally, the experimentally observed value is averaged over the weight fractions α_{P_i}. The sum over all species converges to a value between 0 and 1 and thus scales the diffusion coefficient observed down with respect to that of monomeric peptide D_P.

$$\langle D\rangle = D_\mathrm{P} \sum_{i=1}^{\infty} \alpha_{\mathrm{P}_i}\, i^{-1/3} \tag{47}$$

The enthalpy and entropy of the peptide self-association known from chemical shift fitting determine the weight fractions α_{P_i} according to Equation 17, leaving D_P for each temperature unknown. Equation 46 was used to convert D_P to other temperatures, so that only one diffusion coefficient at an arbitrarily chosen temperature remained unknown, which we chose to be at 300 K. This last coefficient ($D_\mathrm{P}(300\ \mathrm{K})$) was fitted against the data shown in Figure S51 in a least-square analysis. The data point at 19.7 mM was derived by revisiting the corresponding attenuation curve from Reference 1 with the same gradient calibration constant used for the measurements herein and applying Equation 43 for the fitting procedure.

That leads to $D_\mathrm{P}(300\ \mathrm{K}) = 5.68 \times 10^{-10}\,\mathrm{m^2\,s^{-1}}$, which matches well with the value predicted by the power law for monomeric peptide in section 4.1.

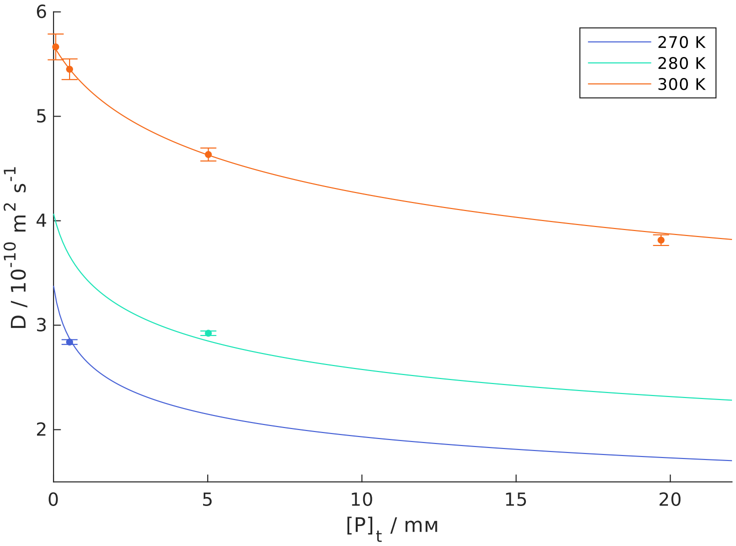

Figure S51: Experimental diffusion coefficients (●) of **1** in toluene-d_8 at different temperatures. The solid lines are the predicted trends for an isodesmic equilibrium model via Eqs. 5, 6, 17, 46, and 47 using the position in equilibrium determined via chemical shift fitting (sec. 3.3.2).

4.3 Comparison of Both Peptide Equilibrium Models

The models EM-P1 and EM-P2 fit equally well to the temperature dependent chemical shift data (see Figures S5 and S7). The diffusion coefficient D and the hydrodynamic radius r_h derived from it provide data complementary to the chemical shifts. To distinguish between models, it is therefore necessary to consider the fit parameters obtained. In the case of the isodesmic model (EM-P2), only the monomeric diffusion coefficient is obtained by fitting the experimental data, averaged by the oligomer distribution. In the monomer-dimer model (EM-P1), a diffusion coefficient per species was obtained by fitting. Comparing the diffusion coefficients for the monomer obtained from both models the physical meaning is identical. However, values obtained for the dimer differed. For the EM-P1 model, this value was much too small, about $2.04 \times 10^{-10}\,\mathrm{m^2\,s^{-1}}$ at 300 K, which corresponds to a hydrodynamic radius of 20.0 Å! Provided that spherical diffusion behavior can be assumed, the estimated diffusion coefficient of the dimer should be close to $4.56 \times 10^{-10}\,\mathrm{m^2\,s^{-1}}$ based on the monomeric diffusion coefficient. In addition, the diffusion coefficients at other temperatures could not be described consistently with the values obtained at 300 K using the monomer-dimer model (EM-P1). These issues are not present in the case of the isodesmic model (EM-P2) and the description of the diffusion coefficient with this model was consistent. Only the isodesmic model (EM-P2) described both temperature dependent chemical shift data and temperature and concentration dependent diffusion coefficients sufficiently accurate, while the monomer-dimer model (EM-P1) failed to produce consistent results. We therefore focused on applying only EM-P2 in the following analyses.

4.4 Diffusion Coefficients of Peptide 1 in Presence of Diol 2 in either (*R*,*R*) or (*S*,*S*) Configuration

The measured diffusion data of peptide **1** at two temperatures in presence and absence of both enantiomers of diol **2** is shown in Figure S52. These samples contained a peptide concentration of about 0.5 mM. The diol concentration was, if present, at about 10 mM (see samples jn-122, jn-112, jn-121 in Tables S5, S8, and S9, respectively, for precise concentrations). To account for the different acquisition parameters of the NMR measurements, Equation 43 is linearized and reordered to Equation 48 so that the slope is directly proportional to the diffusion coefficient.

$$\underbrace{\left(\gamma_H^2\delta^2\frac{81}{100}\left[\Delta-\frac{6344\pi^2-207}{9720\pi^2}\delta-\frac{\tau_1+\tau_2}{2}\right]\right)^{-1}}_{b^{-1}}\cdot\ln\left(\frac{I(g)}{I_0}\right)=-Dg^2 \tag{48}$$

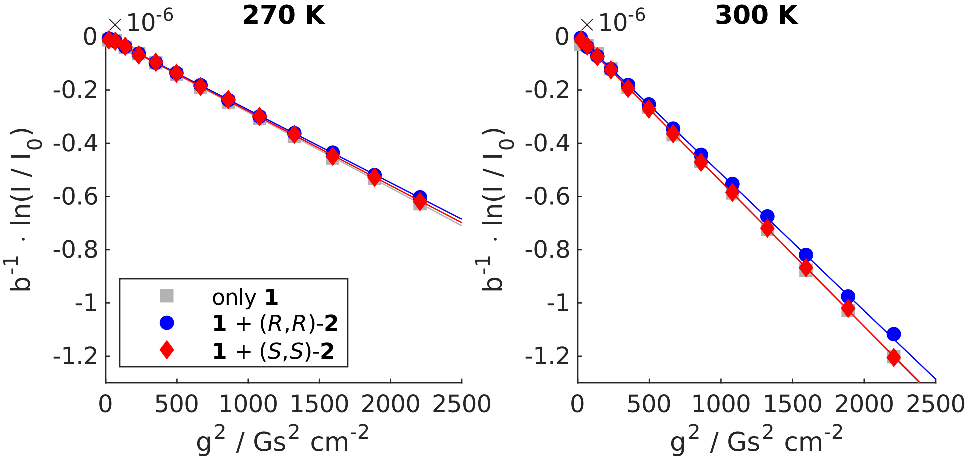

Figure S52: Diffusional intensity attenuation of peptide **1** (symbols) for varying gradient strengths at 270 K (left) and 300 K (right). Solid lines represent the fits employing Equation 48. The data of peptide **1** with (*S*,*S*)-**2** (red ♦) and without any diol (gray ■) overlap almost completely.

Diffusion coefficients and hydrodynamic radii for peptide **1** are given in Table S28. The data can be described well with a single Gaussian decay (linear trend in Figure S52), which verifies the complexation processes are fast compared to the NMR time scale. Figure S52 shows the overall decreased diffusion of tetrapeptide **1** at 270 K compared to the diffusion at 300 K. This is expected from Equation 42 and the various influences on its parameters discussed in part above: Firstly, a decreasing temperature decreases the resulting diffusion coefficient. Secondly, the viscosity (η) increases with lower temperature. Thirdly, the self-association behavior of peptide **1** as described in the prior sections is still present (increase in r_h), which further reduces the diffusion coefficient.

The influence of a 20-fold excess of (*R*,*R*)-**2** over **1** also decreases the diffusion coefficient, while (*S*,*S*)-**2** reproduces nearly the same diffusion coefficient of peptide **1** in absence of diols (more pronounced at 300 K). Therefore, this means that **1** shows a preference for (*R*,*R*)-**2**. A complex of **1** with (*R*,*R*)-**2** forms during the NMR experiment, which diffuses more slowly than **1** without **2**. While at 300 K peptide **1** is mainly present as monomer that can interact with diol (*R*,*R*)-**2**, at 270 K the peptide self-association is more pronouced. Thus, the heteromolecular interactions of **1** with (*R*,*R*)-**2** are overruled by the homomolecular interactions of **1** at 270 K. Still, a small decrease of the peptidic diffusion coefficient is present, meaning the peptide also recognizes (*R*,*R*)-**2** over (*S*,*S*)-**2** at 270 K but the peptide self-association nearly conceals any complexation of the diol.

Table S28: Diffusion coefficients and hydrodynamic radii of tetrapeptide **1** in toluene-d_8 in presence or absence of diols obtained from diffusion measurements at 270 K and 300 K. Hydrodynamic radii were calculated from diffusion coefficients via Equation 42.

T / K	diol	D_P / 10^{-10} m^2 s^{-1}	r_h / Å	sample
270	none	2.84 ± 0.02	8.5 ± 0.1	jn-122
	(*R*,*R*)-**2**	2.74 ± 0.02	8.8 ± 0.1	jn-112
	(*S*,*S*)-**2**	2.79 ± 0.03	8.7 ± 0.1	jn-121
300	none	5.45 ± 0.10	7.5 ± 0.1	jn-122
	(*R*,*R*)-**2**	5.15 ± 0.08	7.9 ± 0.1	jn-112
	(*S*,*S*)-**2**	5.44 ± 0.03	7.5 ± 0.1	jn-121

5 Temperature Coefficients of the Amide Protons in Tetrapeptide 1

For amide protons, the temperature dependency in organic solvents has been well studied and classifications have been made as to when an amide proton forms a hydrogen bond to an acceptor or not. For this purpose, we used the classification for organic non-polar solvents (including toluene) by Alex *et al.*.[42] Commonly, the chemical shift is determined as a function of temperature and the temperature coefficient is obtained from the slope of a linear regression. Since a self-association of the peptide is present here, the chemical shifts obtained from the fitting procedure with EM-P2 (section 3.3.2) were used to determine the temperature coefficients. This leads to the chemical shifts reported in Table S29 for the amide protons in peptide **1** as monomer (P) and in Table S30 for the same protons in the peptide as oligomers (P_ξ). The slopes of the linear regressions (Figure S53) give the temperature coefficients, which provide information about the accessibility of the proton under consideration for the solvent molecules. The plot of the temperature coefficients is shown in Figure S54 for the four amide protons present in tetrapeptide **1**. This shows that the protons ^{P}H7 and ^{P}H16 do not form an intramolecular H-bond. ^{P}H25 and ^{P}H31 show little temperature-dependent change and they are therefore each assigned an intramolecular H-bond in the peptide monomer. Upon self-association to the oligomer, little change is observed for ^{P}H7, and ^{P}H31. For ^{P}H25, the change observed indicates a weakening of the intramolecular H-bond.

The enthalpic energy gain of self-association of about $42\,\mathrm{kJ\,mol^{-1}}$ derived by chemical shift fitting (section 3.3.2) is in line with the energy gain by one newly formed H-bond ($16\,\mathrm{kJ\,mol^{-1}}$ to $60\,\mathrm{kJ\,mol^{-1}}$[43]). The only proton for which a potential H-bond can be assigned is ^{P}H16, since it undergoes the greatest change upon self-association. However, the value of the temperature coefficient for ^{P}H16 in the oligomer does not indicate an H-bond. This may be explained by an averaging of the chemical shift of ^{P}H16 in the oligomers from which the temperature coefficient is derived. While ^{P}H16 in the monomer is readily accessible to the solvent, in the oligomers some protons are accessible and others are not. At this point, a more detailed conclusion cannot be drawn using this method. Also, the acceptor of the intermolecular potential H-bond remains unknown.

Table S29: Fitted proton chemical shifts (from global chemical shift fitting) for monomeric peptide (P) for the equilibrium model EM-P2 at the best fit solution. These chemical shifts have been used for determination of the temperature coefficients.

T / K	$\delta_{\mathrm{P,H7}}$ / ppm	$\delta_{\mathrm{P,H16}}$ / ppm	$\delta_{\mathrm{P,H25}}$ / ppm	$\delta_{\mathrm{P,H31}}$ / ppm
270	6.850 ± 0.168	6.601 ± 0.110	5.324 ± 0.210	5.279 ± 0.123
275	6.841 ± 0.122	6.457 ± 0.089	5.279 ± 0.155	5.272 ± 0.093
280	6.862 ± 0.087	6.462 ± 0.068	5.302 ± 0.109	5.288 ± 0.070
285	6.890 ± 0.064	6.461 ± 0.055	5.325 ± 0.076	5.299 ± 0.057
290	6.901 ± 0.050	6.450 ± 0.047	5.346 ± 0.056	5.309 ± 0.048
295	6.763 ± 0.039	6.292 ± 0.037	5.329 ± 0.043	5.247 ± 0.037
300	6.622 ± 0.021	6.073 ± 0.020	5.203 ± 0.023	5.171 ± 0.019
305	6.665 ± 0.044	6.076 ± 0.041	5.389 ± 0.046	5.211 ± 0.041
310	6.663 ± 0.062	6.063 ± 0.061	5.331 ± 0.062	5.222 ± 0.061

Table S30: Fitted proton chemical shifts (from global chemical shift fitting) for oligomeric peptide (P_ξ) for the equilibrium model EM-P2 at the best fit solution. These chemical shifts have been used for determination of the temperature coefficients.

T / K	$\delta_{P_\xi,H7}$ / ppm	$\delta_{P_\xi,H16}$ / ppm	$\delta_{P_\xi,H25}$ / ppm	$\delta_{P_\xi,H31}$ / ppm
270	8.536 ± 0.038	7.332 ± 0.036	7.595 ± 0.041	6.256 ± 0.036
275	8.505 ± 0.037	7.328 ± 0.033	7.609 ± 0.041	6.248 ± 0.034
280	8.439 ± 0.036	7.276 ± 0.032	7.583 ± 0.041	6.222 ± 0.032
285	8.343 ± 0.038	7.197 ± 0.034	7.542 ± 0.043	6.184 ± 0.035
290	8.243 ± 0.040	7.103 ± 0.037	7.488 ± 0.044	6.138 ± 0.038
295	8.302 ± 0.030	7.159 ± 0.029	7.480 ± 0.032	6.169 ± 0.029
300	8.262 ± 0.022	7.171 ± 0.020	7.435 ± 0.025	6.150 ± 0.020
305	8.242 ± 0.042	7.144 ± 0.041	7.370 ± 0.043	6.136 ± 0.041
310	8.173 ± 0.114	7.065 ± 0.111	7.437 ± 0.120	6.084 ± 0.110

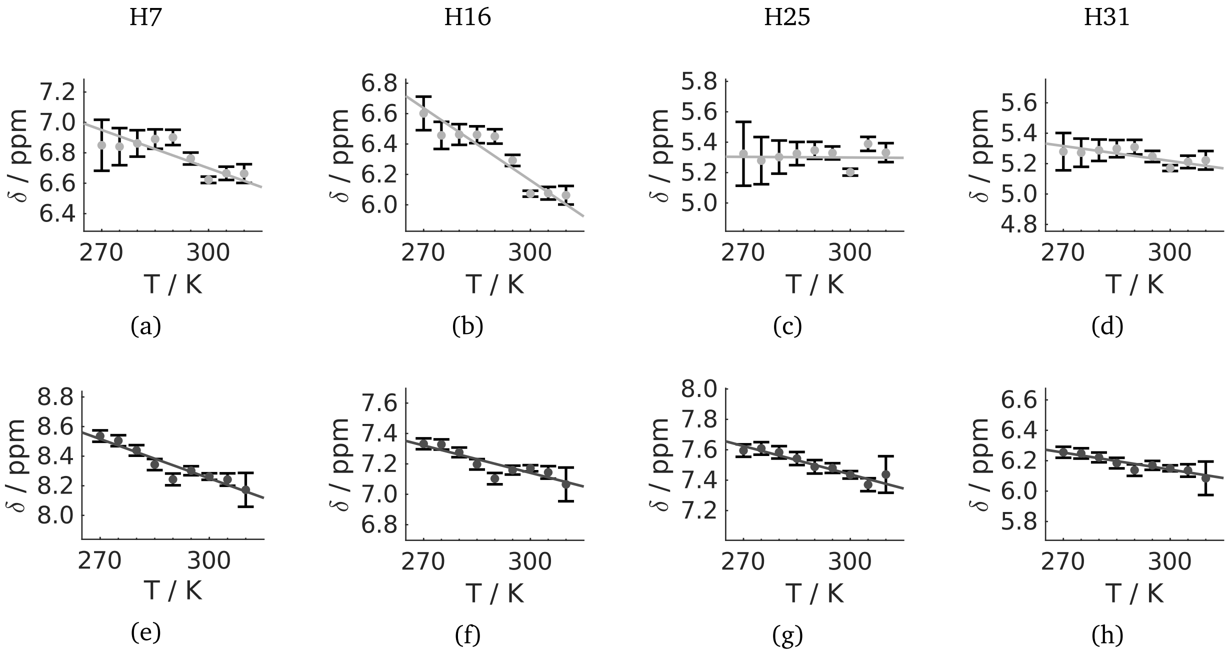

(a) (b) (c) (d)

(e) (f) (g) (h)

Figure S53: Plots of the chemical shifts derived with equilibrium model EM-P2 versus temperature, which visualizes the values given in Tables S29 and S30. Plots (a) to (d) show the proton chemical shifts of H7, H16, H25 and H31, respectively, in the monomer and plots (e) to (h) the same proton chemical shifts averaged in the oligomers. All plots are scaled equally in all axes. The slope is the temperature coefficient.

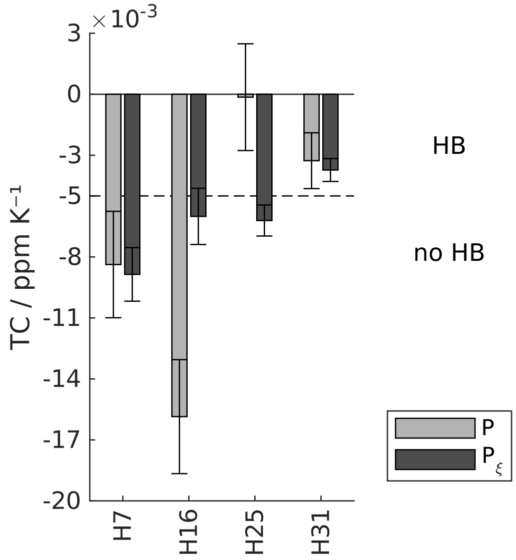

Figure S54: Temperature coefficients derived from the slope of the fits shown in Figure S53 for all amide protons in peptide **1**.

6 Tetrapeptide Self-Association in Different Solvents

The peptide self-association has been investigated in the three different organic solvents toluene, dichloromethane, and acetone. As the polarity increases from toluene to acetone we expected to observe decreasing peptide self-association in the polar solvents compared to toluene as hydrogen bond donors and acceptors may be better stabilized by the more polar solvent molecules. The observed chemical shifts of peptide **1** also depend on concentration in these solvents, but to a far lesser extent than in toluene. Therefore, the chemical shifts obtained in these solvents were also entered into the fitting procedure applying the isodesmic model (EM-P2) as described in section 3. This leads to enthalpies and entropies of association for each solvent as reported in Table S31 and a graphical depiction of these quantities in Figure S55. In all solvents, self-association decreased with increasing temperature and from toluene via dichloromethane to acetone (ΔG closer to zero). This is also impressively reflected by the equilibrium constant at one temperature (here 300 K). For an arbitrarily chosen concentration of 20 mM: only 14.1 % of the free peptide (α_P) is present in toluene, while the fraction in dichloromethane and acetone is 84.9 % and 93.8 %, respectively.

The proposed intermolecular hydrogen bond described for toluene in section 5 is assumed to be better saturated in the more polar solvents dichloromethane and acetone. Thus, an attractive interaction between two or more peptide monomers is in competition with an interaction with the solvent leading to a higher fraction of monomeric peptide.

Table S31: Extracted enthalpies and entropies of peptide **1** self-association in different solvents applying the isodesmic equilibrium model (EM-P2). The equilibrium constant at 300 K is determined with Eqs. 5 and 6. The fraction of free peptide at the same temperature is exemplarily calculated with Equation 17 for a total peptide concentration of 20 mM.

solvent	ΔH / kJ mol^{-1}	ΔS / J mol^{-1} K^{-1}	K_A(300 K) / M^{-1}	α_P(300 K, 20 mM) / %
toluene-d_8	-41.82 ± 4.03	-94.50 ± 13.45	221	14.1
dichloromethane-d_2	-20.97 ± 1.53	-57.16 ± 5.71	4.63	84.9
acetone-d_6	-14.39 ± 2.90	-43.67 ± 10.80	1.67	93.8

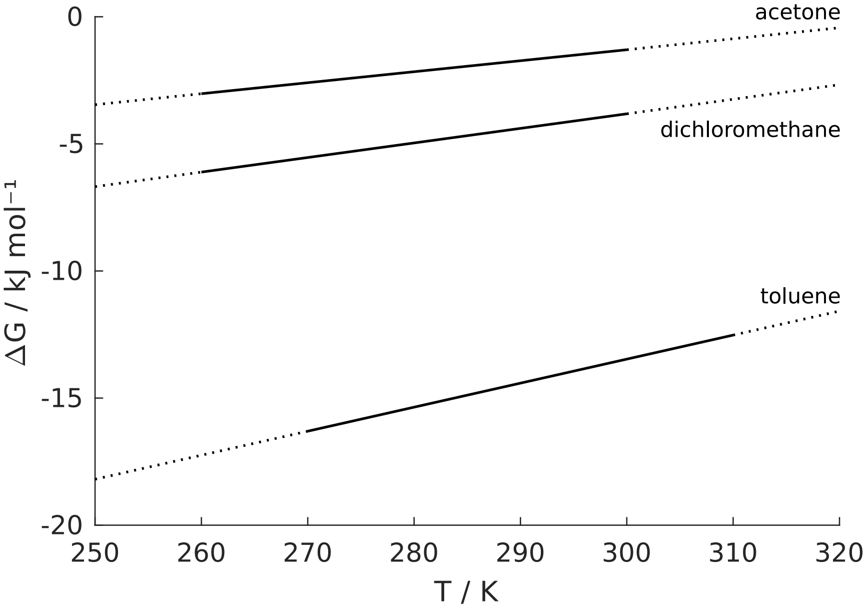

Figure S55: Variation of the Gibbs energy with temperature for the solvents toluene, dichloromethane and acetone. Note that all energies given are below zero, which means that self-association is present in all solvents in the temperature range investigated.

6.1 Self-Association in Relation to the Solvent Permittivity

A comparison between the solvents is possible by relating the association constant (K_A) with the relative permittivity of the solvent (ε_r). If it is assumed that the classical Born treatment[44] is suitable to account for the electrostatic contribution to the Gibbs energy change, the plot of the logarithm of the association constant ($\ln K_A$) versus the inverse of the dielectric constant ($1/\varepsilon_r$) should be linear. The relationship was originally developed to describe and quantify ion radii in water, but can also be qualitatively applied to acid-base equilibria in protic media[45] as well as homodimerizations[46,47] and heterodimerizations[48] in aprotic organic solvents. In all given cases a linear plot can be constructed from the provided data.

The temperature dependent relative permittivity of the solvents used is estimated by Equation 49 with the corresponding coefficients a, b and c, given in Table S32.[49]

$$\varepsilon_r = a + b \cdot T + c \cdot T^2 \tag{49}$$

Table S32: Coefficients for Equation 49 taken from Reference 49.

solvent	a	b / K^{-1}	c / K^{-2}
toluene-d_0	3.2584	-3.4410×10^{-3}	1.5937×10^{-6}
dichloromethane-d_0	4.0452×10^{1}	-1.7748×10^{-1}	2.3942×10^{-4}
acetone-d_0	8.8157×10^{1}	-3.4300×10^{-1}	3.8925×10^{-4}

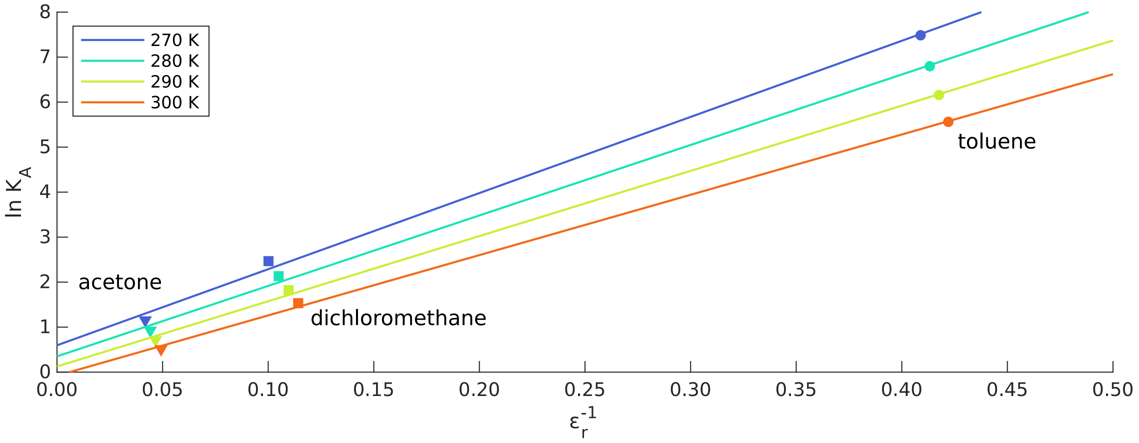

Figure S56: Variation of the association constant of the peptide self-association with the relative solvent permittivity at selected temperatures. Here, the peptide self-association is investigated in toluene (●), dichloromethane (■), and acetone (▼). The solid lines (—) are linear fits for each temperature.

7 Transverse Relaxation Rate Analysis of Diol 2 in the Presence of Peptide 1

To study intermolecular interactions, relaxation rates are a well established tool for the quantification of binding affinities.[24,50,51] A multitude of molecular interactions affect the relaxation behavior, with the transverse relaxation rate R_2 often being most sensitive to changes in association equilibria.[24] When a substrate is in close proximity to its binding partner, more efficient relaxation pathways become available than when it is surrounded only by deuterated solvent. Thereby, stronger interactions lead to an increased relaxation rate.[24] We therefore measured the transverse relaxation rate of proton ^{D}H1 in **2** in the presence of tetrapeptide **1** while varying its excesses ($[D]_t/[P]_t = \{4, 8, 14, 20\}$) using PROJECT[10] (section 2.2.15). Analysis was performed with Equation 2, which was fitted to the extracted signal intensities I to obtain the transverse relaxation rate R_2 using Equation 3 for the determination of the duration t. N is the repetition number of double spin echoes, τ the length of the interpulse delay defined in the pulse sequence, and P1 the length of the 90° proton pulse.

The determined transverse relaxation rates of proton ^{D}H1 of (*R*,*R*)-**2** and (*S*,*S*)-**2** are shown in Figure S57. For both enantiomers of **2**, R_2 remained about the same for increasing concentration and increased for decreasing temperatures. In most cases, the transverse relaxation rate higher for (*R*,*R*)-**2** as compared to (*S*,*S*)-**2** at the same concentration and temperature. At 300 K Kelvin, however, (*S*,*S*)-**2** showed increasing rates for increasing concentrations. In summary, the more efficient relaxation of (*R*,*R*)-**2** provides further evidence for the stronger interaction for (*R*,*R*)-**2** in the temperature range relevant for catalysis (273 K).

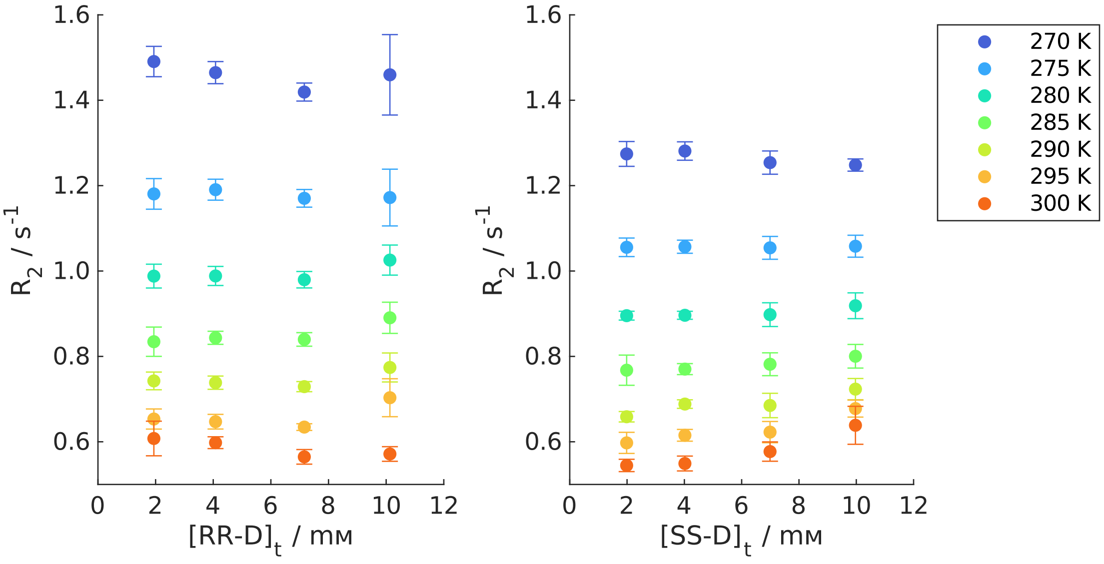

Figure S57: Proton transverse relaxation rates R_2 of ^{D}H1 for varying total diol concentration ($[RR\text{-}D]_t$ or $[SS\text{-}D]_t$) and temperature measured via PROJECT.[10] The left plot is obtained from a sample of **1** and (*R*,*R*)-**2**, while for the right plot (*S*,*S*)-**2** was used. The peptide concentration was constant at 0.5 mM.

8 Determination of STD Amplification Factors

The STD amplification factors were determined by fitting the obtained intensities of on- and off-resonance spectra of ^{D}H1 in cyclohexane-1,2-diol **2**. Exemplary difference spectra are given in section 8.1. The off-resonance spectrum is the reference spectrum for each pair, where irradiation was performed in a spectral region without signals. Therefore, no resonances were excited, which leads to the elimination of potential differences between on- and off-resonance spectra not originating from binding events (*e.g.*, sample heating). Selectively irradiating ^{P}H8 in peptide **1** led to a slightly reduced intensity on ^{D}H1 in **2** in the on-resonance case. By subtracting the on-resonance spectrum from the reference the difference spectrum was obtained (main text Figure 3). The STD amplification (I_{STD}) at a specific saturation time t_{sat} is defined as in Equation 50, where I_{on} and I_{off} are the intensities of ^{D}H1 in the on-resonance and reference spectrum, respectively. Alternatively, the intensity of ^{D}H1 in the difference spectrum (I_{diff}) can be used. The quantity was scaled by the concentration ratio of the binding partners ($r = [\mathrm{D}]_t/[\mathrm{P}]_t$).[52]

$$I_{\mathrm{STD}}(t_{\mathrm{sat}}) = \frac{I_{\mathrm{off}} - I_{\mathrm{on}}}{I_{\mathrm{off}}} \cdot r = \frac{I_{\mathrm{diff}}}{I_{\mathrm{off}}} \cdot r \tag{50}$$

Depending on the saturation time, the STD amplifications increase until saturation is reached. At this point relaxation and magnetization build-up are in equilibrium and the net magnetization does not change. The obtained intensities were fitted with Equation 51 to yield the STD coefficients I_{max} and k_{sat}, which are the maximum achievable intensity and the build-up rate constant, respectively.

$$I_{\mathrm{STD}}(t_{\mathrm{sat}}) = I_{\mathrm{max}}\left[1 - \exp(-k_{\mathrm{sat}} t_{\mathrm{sat}})\right] \tag{51}$$

The intensities of a sample with a 20-fold nominal excess of (*R*,*R*)-**2** over **1** (sample jn-112) are shown in Figure S58 together with the fitted saturation curves.

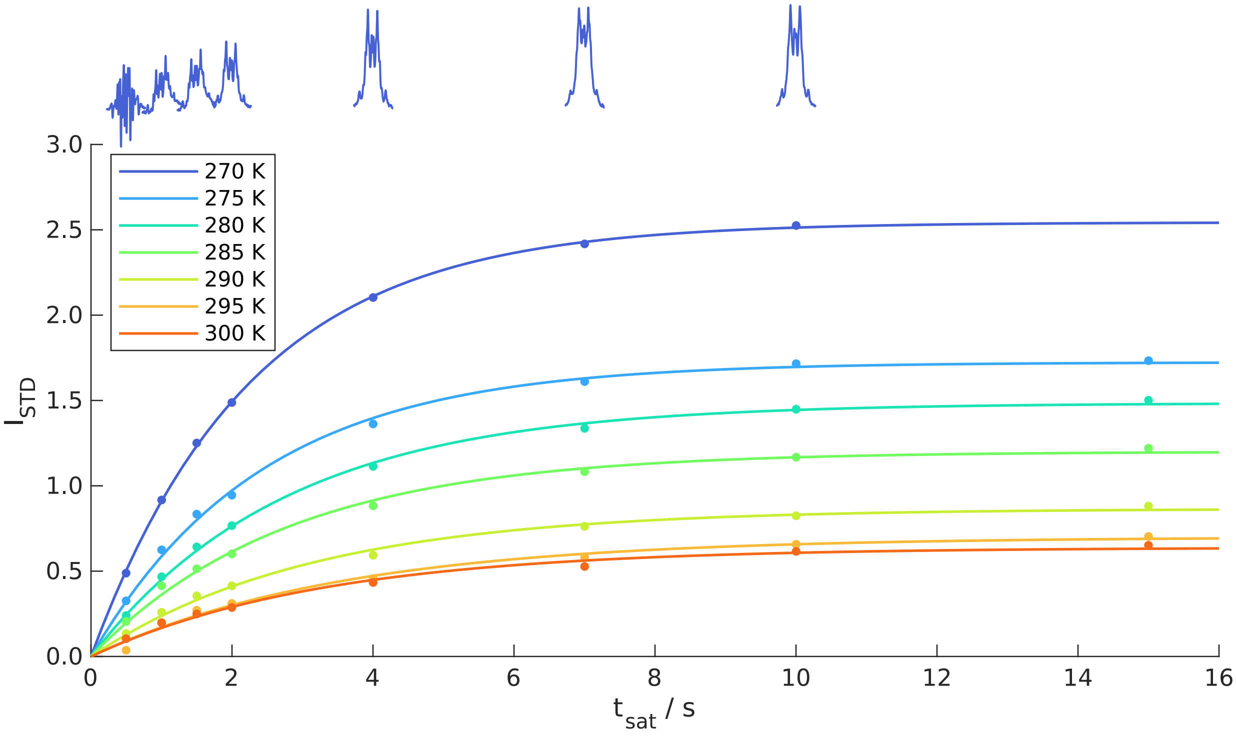

Figure S58: Saturation build-up curves of ^{D}H1 in (*R*,*R*)-**2** for a sample (jn-112) with 10 mM diol (*R*,*R*)-**2** and 0.5 mM peptide **1** upon irradiation of ^{P}H8 in **1** at different temperatures. The signals above the plot illustrate the STD response on ^{D}H1 at ca. 3.20 ppm in the difference spectra at 270 K.

All STD measurements on samples with either (R,R)-**2** or (S,S)-**2** show qualitatively the same saturation build-up. As will be seen below, there are, however, differences in the quantitative evaluation. The product of I_max and k_sat yields the initial slope of the corresponding build-up curve, which avoids potential obstructive effects on the accumulation of saturation. These effects may originate from different longitudinal relaxation times and rebinding processes.[53] This approach extrapolates to the build-up rate at $t_\mathrm{sat} = 0$ and links it with the macroscopic dissociation constant K_D^STD according to Equation 52 instead of STD amplifications at an arbitrarily chosen saturation time. Here, B is a scaling factor, that is the maximum initial build-up rate at infinite excess of diol, which depends on the longitudinal relaxation rate of the free diol and magnetization transfer rate from the peptide onto the diol in the bound case.[54] The equilibrium constant K_D^STD is associated with a simple 1:1 equilibrium of a peptide and diol molecule for the analysis of STD measurements.

$$I_\mathrm{max} \cdot k_\mathrm{sat} \approx B \frac{[\mathrm{D}]_t}{[\mathrm{D}]_t + K_D^\mathrm{STD}} \tag{52}$$

K_D^STD can also be expressed as Gibbs energy according to Equation 5 with the relation that $K_D = K_A^{-1}$. Therefore, ΔG and B were fitted against the initial slope $I_\mathrm{max} \cdot k_{sat}$ of the corresponding total diol concentration $[\mathrm{D}]_t$ for each temperature. All fit parameters are shown in Table S33 and the Gibbs energy is plotted against the temperature in Figure S59 (right plot) for all fits.

Table S33: Overview over the fitting parameters retrieved from fits of B and ΔG against $I_\mathrm{max} \cdot k_\mathrm{sat}$ for both diol enantiomers with different restraints.

diol	restraints	RMSD	$T/\mathrm{K} =$	270	275	280	285	290	295	300
(R,R)-**2**	none	0.02656	$K_D^\mathrm{STD}/\mathrm{mM} =$	9392	30	24	27	24	19	18
			$\Delta G/\mathrm{kJ\,mol^{-1}} =$	5.03	−7.99	−8.64	−8.57	−8.98	−9.70	−10.05
			$B/\mathrm{s^{-1}} =$	435.2	1.50	1.18	1.06	0.68	0.44	0.39
	$B \leq 3$	0.02872	$K_D^\mathrm{STD}/\mathrm{mM} =$	57	30	24	27	24	19	18
			$\Delta G/\mathrm{kJ\,mol^{-1}} =$	−6.43	−7.99	−8.64	−8.57	−8.98	−9.70	−10.05
			$B/\mathrm{s^{-1}} =$	3.00	1.50	1.18	1.06	0.68	0.44	0.39
	$B \leq 3$ ΔG	0.02888	$K_D^\mathrm{STD}/\mathrm{mM} =$	57	44	34	26	21	16	13
			$\Delta G/\mathrm{kJ\,mol^{-1}} =$	−6.43	−7.16	−7.89	−8.62	−9.34	−10.07	−10.80
			$B/\mathrm{s^{-1}} =$	3.00	2.01	1.52	1.05	0.61	0.39	0.32
(S,S)-**2**	none	0.01398	$K_D^\mathrm{STD}/\mathrm{mM} =$	32477	30	141	9857	11314	75	29589
			$\Delta G/\mathrm{kJ\,mol^{-1}} =$	7.81	−8.02	−4.56	5.42	5.85	−6.34	8.45
			$B/\mathrm{s^{-1}} =$	767.75	0.76	2.89	179.82	214.49	1.57	767.93
	$B \leq 3$	0.01511	$K_D^\mathrm{STD}/\mathrm{mM} =$	119	30	141	156	150	75	108
			$\Delta G/\mathrm{kJ\,mol^{-1}} =$	−4.78	−8.02	−4.56	−4.40	−4.57	−6.34	−5.56
			$B/\mathrm{s^{-1}} =$	3.00	0.76	2.89	3.00	3.00	1.57	3.00
	$B \leq 3$ ΔG	0.01525	$K_D^\mathrm{STD}/\mathrm{mM} =$	119	117	115	113	111	109	108
			$\Delta G/\mathrm{kJ\,mol^{-1}} =$	−4.78	−4.91	−5.04	−5.17	−5.30	−5.43	−5.56
			$B/\mathrm{s^{-1}} =$	3.00	2.51	2.39	2.21	2.26	2.22	3.00

A fit with no restraints on the data of (R,R)-**2** gave consistent parameters for all but one temperature (270 K), where both ΔG and B differ largely. As the value of B at 270 K seems unrealistic compared to the others and the initial build-up rate increases to a good extent linearly (the exact dependency is unknown) with decreasing temperature for the other isotherms, an upper limit for B was employed. From a linear fit of B against T in the range of 275 K to 300 K, we expected a value of around 1.7 $\mathrm{s^{-1}}$ at 270 K. So, 3 $\mathrm{s^{-1}}$ as an upper limit should give enough range for the fitting parameter, even if the temperature dependency of B is not linear. This led to a Gibbs energy that was consistent with those at the other temperatures, whereas B is essentially fixed to the upper limit at 270 K. Furthermore, we evaluated whether employing Equation 6 (implying a global fit, also entering a restraint on ΔG) in the final fit leads to different results. This reduces the number of fit parameters by 5 and results in a slight increase in RMSD, which also justifies the use of a global fit. This fit is shown in Figure S59 left.

The fits for the measurements with (*S*,*S*)-**2** largely scattered around 1.6 kJ mol^{-1}, if no restraints were applied. Again the initial build-up rates were unreasonably high for most temperatures, except that at 275 K. Furthermore, it is also inconsistent that the qualitatively worse binder should show a higher value in B. However, it is known that it nevertheless binds as there are chemical shift changes and measurable STD amplifications. When comparing the measured data points of all isotherms from (*S*,*S*)-**2** with those from (*R*,*R*)-**2** visually (Figure S59 left and middle), we noticed that all points of (*S*,*S*)-**2** were located between the isotherms at 285 K and 290 K for (*R*,*R*)-**2**. The only "outlier" of (*S*,*S*)-**2** at 275 K matched exactly the range defined by both isotherms of (*R*,*R*)-**2**. Therefore, the same restraints were also applied to the fits with (*S*,*S*)-**2**, which again led to a fixation of B to 3 s^{-1}. Enforcing a linear Gibbs energy, was also tried (last line in Table S33), but again did not significantly increase the RMSD.

In any case the dissociation constants or Gibbs energies derived by STD need to be critically evaluated and should only be interpreted as an upper bound. For (*S*,*S*)-**2** the values of the Gibbs energy match well with the energy derived by chemical shift fitting at 300 K. But for (*R*,*R*)-**2** a difference of about 3 kJ was observed (★ in Figure S59 right). The data points measured (Figure S59 left) at a 20-fold excess of (*R*,*R*)-**2** were systematically higher than the corresponding fit curves, meanwhile the points at 14-fold excess were systematically lower. This may originate from non-specific binding similar to the data shown in the SI of Reference 53. For the analysis of STD measurements a 1:1 peptide-diol equilibrium is assumed in Equation 52, which is in the majority a sufficient treatment for protein-substrate binding studies. Other binding events were thus not considered in this type of analysis. But if present, these processes lead to higher amplifications detected by STD at high diol to peptide ratios, which in turn also increase the extracted values K_D^{STD}. The performed chemical shift fitting in this work is far more sophisticated and takes several additional binding processes into account and thus is considered as more accurate.

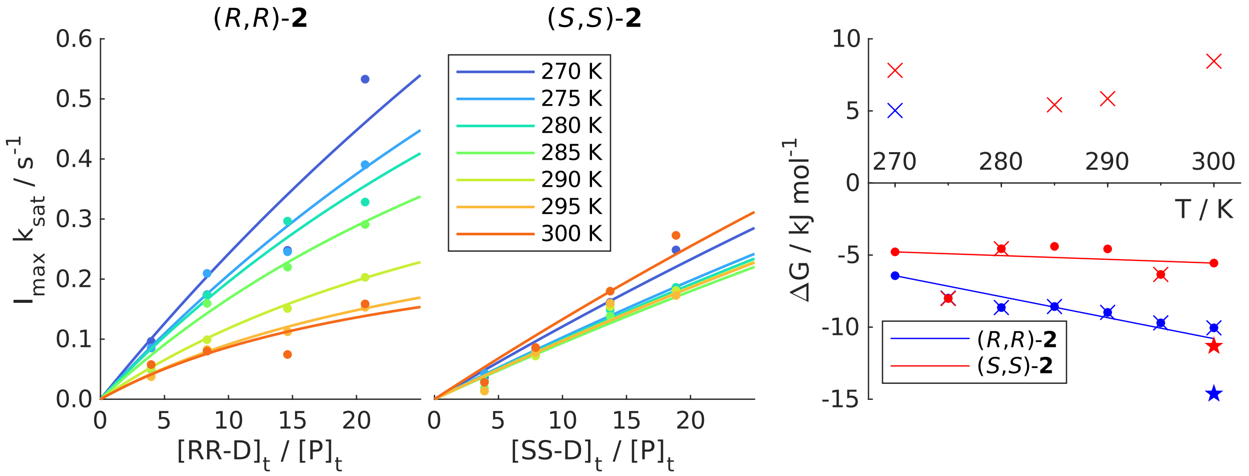

Figure S59: Left and middle: Experimental initial build-up rate in dependency of the diol-peptide ratio r for both enantiomers of diol **2** as •. The solid lines show the best global fit with $B \leq 3$ s^{-1}. Right: The Gibbs energy plot versus the temperature shows the different fits as described in the text. The energies obtained by the fits without restraints, limit B to 3 s^{-1}, and the combination of the B-limit with the determination of ΔG by Equation 6 are displayed as ×, • and as a solid line, respectively. For comparison, the Gibbs energy derived by chemical shift fitting is also plotted (★, ΔG_3 of EM-PD8).

8.1 Exemplary ^{1}H STD spectra

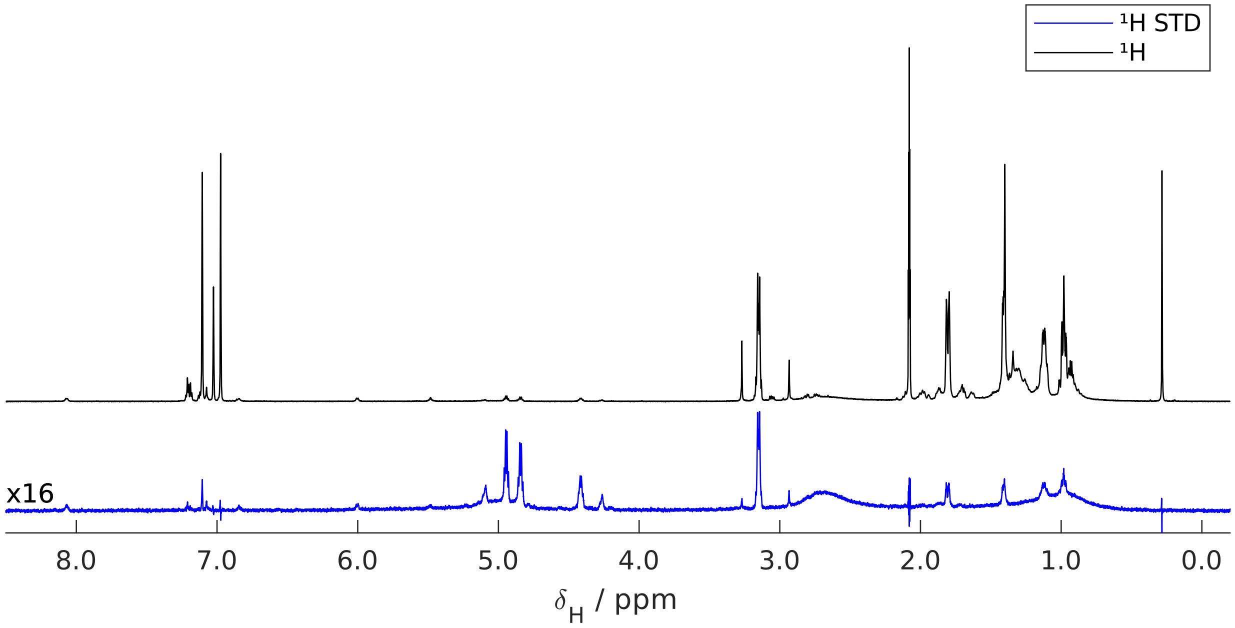

Figure S60: Full conventional ^{1}H spectrum (top) and full ^{1}H STD (difference) spectrum (bottom) of 10 mM (*R*,*R*)-**2** with 0.5 mM **1** in toluene-d_8 at 270 K. **1** is selectively irradiated for 10 s at 4.8 ppm.

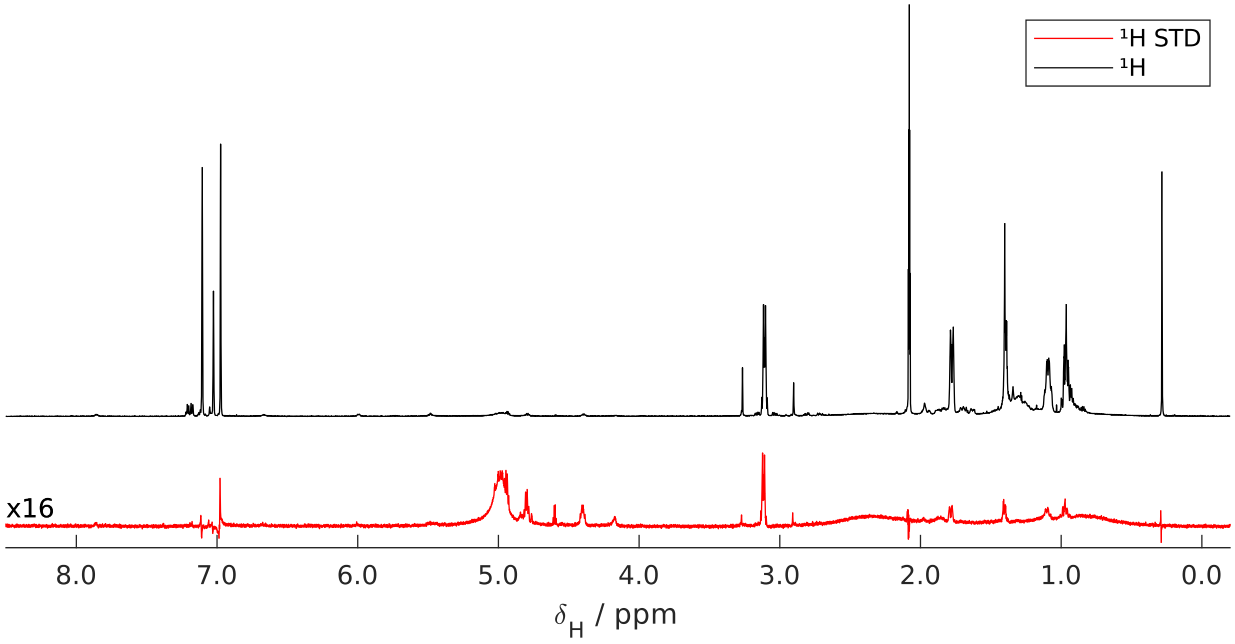

Figure S61: Full conventional ^{1}H spectrum (top) and full ^{1}H STD (difference) spectrum (bottom) of 10 mM (*S*,*S*)-**2** with 0.5 mM **1** in toluene-d_8 at 270 K. **1** is selectively irradiated for 10 s at 4.8 ppm.

8.2 ^{1}H STD Controls

We performed control experiments to exclude the possibility of false positive STD amplifications, which is a known phenomenon for self-associating organic compounds.[55] This is shown in the following section, where the STD response was tested in the presence and absence of peptide **1**. Additionally, the influence of the selective irradiation frequency was investigated. STD spectra were also measured at different peptide concentrations and all samples exhibited an STD amplification (data not shown here). Additionally to these control experiments, the saturation profile of the used pulse (ESnob[22]) is shown in section 10.

8.2.1 Spectra Comparison of Samples with and without Peptide

The influence of the peptide being present is shown in Figure S62. The signal intensities of all diol signals increase if peptide is present (blue and red) compared to the sample without peptide (black). Thus, a false positive is excluded.

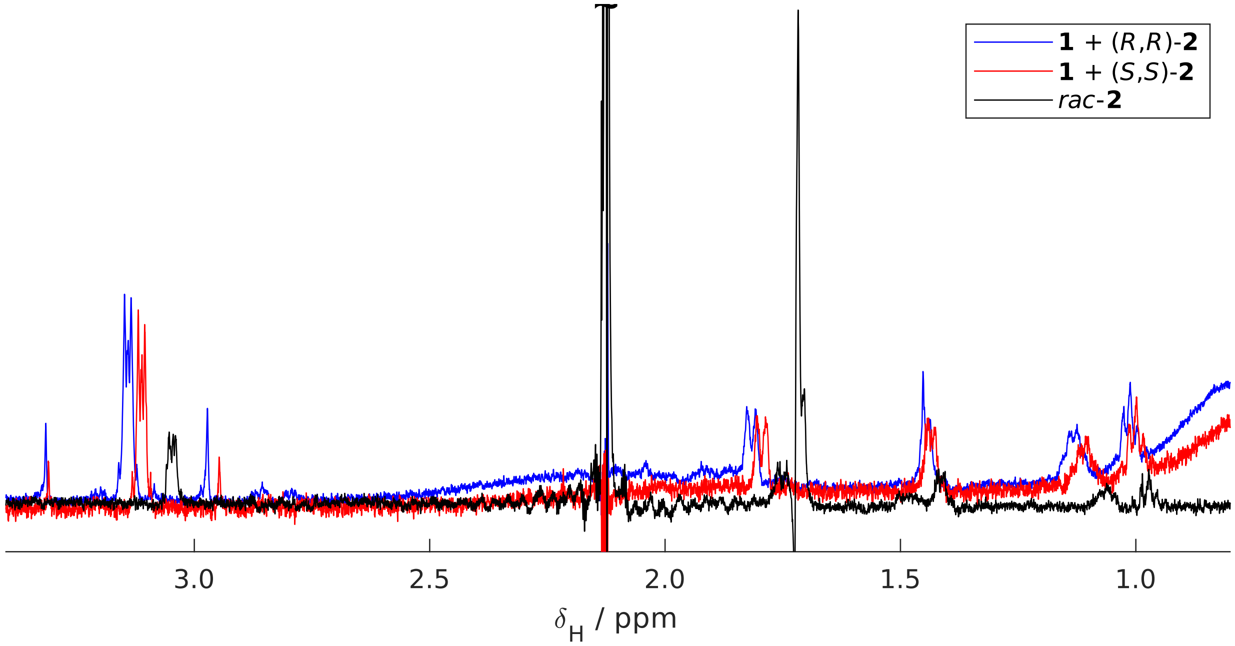

Figure S62: ^{1}H STD difference spectra of different samples (blue: jn-110, red: jn-119, black: jn-113) show the signal amplification by STD if peptide **1** is present in solution. The spectra were measured at 700 MHz resonance frequency and 270 K. The saturation time was 15 s of irradiation at 4.8 ppm. The intensity of ^{D}H1 (approx. 3.1 ppm) is increased by a factor of 2.9 for (*R*,*R*)-**2** and 2.1 for (*S*,*S*)-**2** in relation to the measurement without peptide.

8.2.2 Spectra Comparison of Different Irradiation Frequencies

The influence of the irradiation frequency was tested by shifting the frequency under otherwise identical conditions. As Figure S63 shows, the diol signals are amplified in all cases irrespective of the signal of peptide **1** selected for irradiation. In all cases the signal intensity of ^{D}H1 is similar, with the irradiation at 4.8 ppm showing the highest amplification.

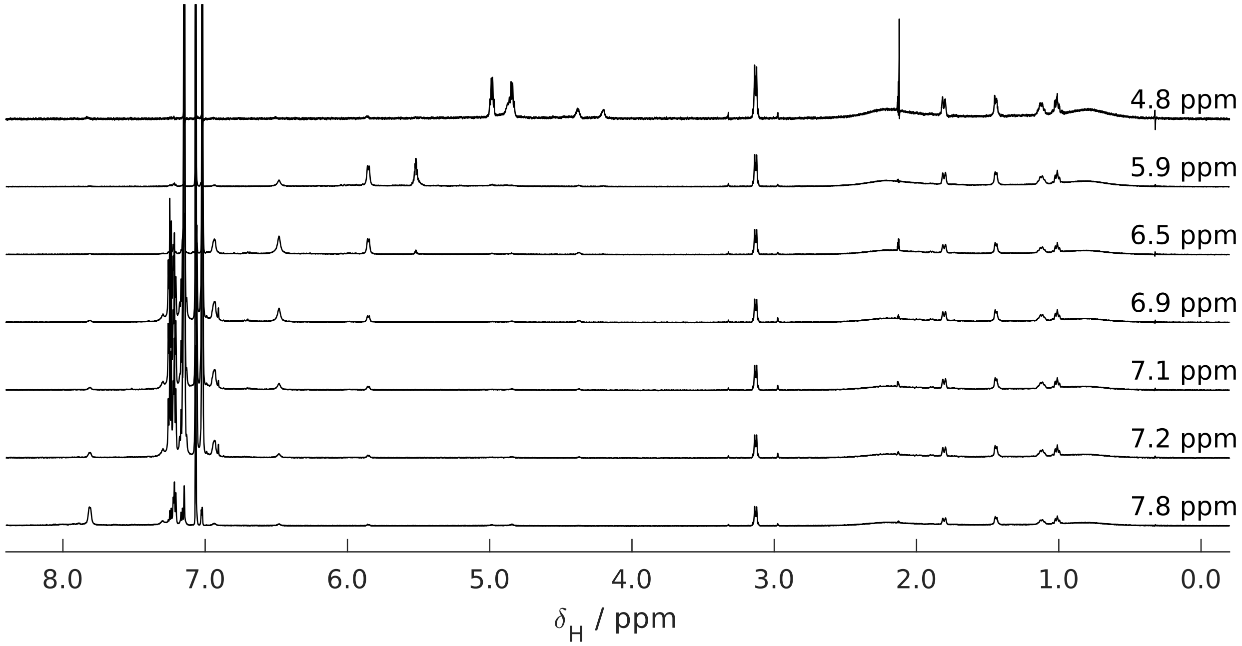

Figure S63: ^{1}H STD difference spectra of 10 mM (*R*,*R*)-**2** with 0.5 mM **1** in toluene-d_8 (jn-112). The spectra were measured at 700 MHz resonance frequency and 280 K. The saturation time was 15 s of irradiation at chemical shifts given in the figure. The signals of (*R*,*R*)-**2** are amplified irrespective of the frequency selected.

9 Acylation Reactions under Catalytical Conditions

In order to interpret the recorded data of the reaction monitoring, some general conditions have to be recapitulated. Basically, two mechanisms with *N*-methylimidazole or similar nitrogen-containing heterocycles (*e.g.* pyridine and its derivatives) as catalyst are considered plausible and discussed in the literature.[56,57] The acylation site identified for the peptide **1** is the imidazole moiety.[58] The underlaying basic mechanisms discussed are assumed to be applicable to the peptide catalyst. Both mechanisms(see Figure S65) consist of three steps; in both an ion pair is formed in the first step. The transition state of the two catalytic mechanisms is shown in Figure S64, with the corresponding ion pair. The imidazole catalyst can acts as Lewis base, with the free electron pair attacking one carbonyl group of acetic anhydride and forming an acylium cation along with acetate (step 1). After that the alcohol approaches the ion pair forming a ternary complex (step 2), which reacts to the product by the transfer of the acyl group (step 3). On the other hand, if the catalyst acts as Brønsted base, the alcohol is deprotonated and an alkoxide forms (step 1). Acetic anhydride adds to the ion pair forming a ternary complex (step 2). The acyl transfer from acetic anhydride to the alcohol occurs and acetic acid is formed (step 3). For both mechanisms the acyl-transfer (step 3) is believed to be the rate-determining step.[59] Which mechanism is prevailing for a particular system is difficult to determine: Depending on reagents, catalyst, and reaction conditions (*e.g.*, temperature, solvent), both limiting mechanisms might play a role in varying ratios. The Lewis base mechanism is generally proposed,[60,61] but also the Brønsted base mechanism was reported to be operative previously.[62]

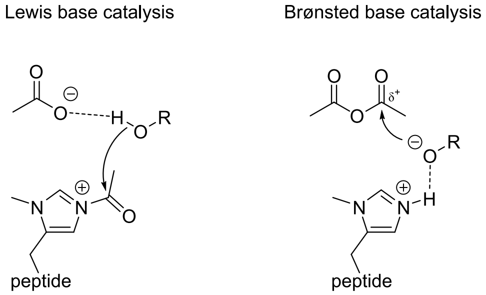

Figure S64: Comparison of the acyl transfer step of both discussed mechanisms.[56] If the imidazole derivative acts as Lewis base (left), an acylium ion and acetate form prior to the attack of the alcohol on the cation. The high basicity of the acetate anion in non-polar solvents deprotonates the alcohol. If the catalyst acts as a Brønsted base (right), it deprotonates the alcohol and the corresponding alkoxide nucleophilically attacks the acyl source.

For acylations with *N*,*N*-dimethyl-4-aminopyridine (DMAP) as catalyst detailed DFT calculations and kinetic studies have been performed. The computed energy profiles of the reaction studied (*tert*-butanol with acetic anhydride) favor the Lewis base mechanism also when considering different non-polar organic solvents (tetrachloromethane, chloroform, dichloromethane). The concentration dependent reaction rate measurements showed a first-order rate dependency in each catalyst (DMAP), alcohol (cyclohexanol), and acyl source (acetic anhydride). No changes in reaction rates (zeroth order) have been observed in the measurements, when the concentration of an auxiliary base (triethylamine) has been varied. The acetate is thus likely the base relevant for the deprotonation.[59] Catalytic activity has also been observed in the complete absence of an auxilary base.[3,63] Different acylpyridinium salts with less basic anions (chloride, tosylate, tetrafluoroborate) do not react with *tert*-butanol in chloroform or more polar organic solvents at 25 °C.[64]

The presence of a preequilibrium prior to the rate-determining step is plausible as an inverse kinetic isotope effect (IKIE) with DMAP, *tert*-butanol, and acetic anhydride was observed.[64]

The kinetic resolution of *rac*-**2** with **1** investigated here, also requires a selection event in the mechanism. This can be formulated to be a preequilibrium between the catalyst and the diol and the catalyst-diol complex. We have shown previously that the acetylated intermediate of peptide **1** in dichloromethane shows a constant concentration in presence of an excess of acetic anhydride during reaction with diol (*R*,*R*)-**2**. This also agrees with a preequilibrium.[58]

The reaction rates also depend on the polarity of the solvent. The highest reaction rates (tested with 1,1-diphenylethanol and DMAP) have been measured in organic solvents of low polarity. Ion pairs are a plausible explanation for the trend found in the reactivities.[65,66] The stabilization of ions is unfavorable in non-polar organic solvents,[67] thus their concentration is low. Compared to water as solvent, non-polar solvents also increase the basicity of acetate and reduce the basicity of *N*-methylimidazole.[68–73] Nevertheless, the acetylated peptide could be detected NMR spectroscopically in dichloromethane and toluene, if the peptide concentration is sufficiently high and an excess of acetic anhydride is provided.[58] In contrast to the interactions of the peptide with diol **2**, which are fast on the NMR time scale, a separate set of signals could be detected for the acetylated peptide,[58] which means that the process of acetylating the peptide is slow on the NMR time scale. For the corresponding acetylimidazolium ion, a rate constant of $17\,\mathrm{M}^{-1}\,\mathrm{min}^{-1}$ has been reported for the cleavage of the ion with acetate at 25 °C in water.[74] Under the same conditions, the hydrolysis of acetylimidazolium is three orders of magnitude ($0.051\,\mathrm{M}^{-1}\,\mathrm{min}^{-1}$)[74] slower, which is roughly comparable to an attack by an alcohol. Ordering the reaction steps by their rate, addition of the diol is the fastest, followed by addition of the acetic anhydride, and acyl transfer from peptide to diol is the slowest and thus rate-determining.

Taking the aforementioned considerations into account, results in the catalytic cycles shown in Figure S65. For catalytic cycle 1 (Figure S65a), which is inspired by Lewis base catalysis, the first step is the formation of the acylated peptide catalyst (PAc^+) and acetate (AcO^-) as loosely bound ion pair. In the second step the diol (D) adds to the ion pair. Both steps are proposed to be equilibria, which is quite reasonable also for the second step because the interactions are non-covalent. From the ternary complex ($\mathrm{PAc}^+\mathrm{D}\cdot\mathrm{AcO}^-$) the final products monoacetylated diol (DAc) and acetic acid (AcOH) form in the rate-determining step. For the catalytic cycle 2 (Figure S65b), the steps in which the reactants add to the peptide catalyst are swapped. The peptide catalyst is approached by the diol first to form the binary complex PD. In the second step the binary complex is acetylated at the peptide. The third final step is the acyl-transfer from the peptide onto the diol, which is the same step as in catalytic cycle 1 and also the rate-determining step.

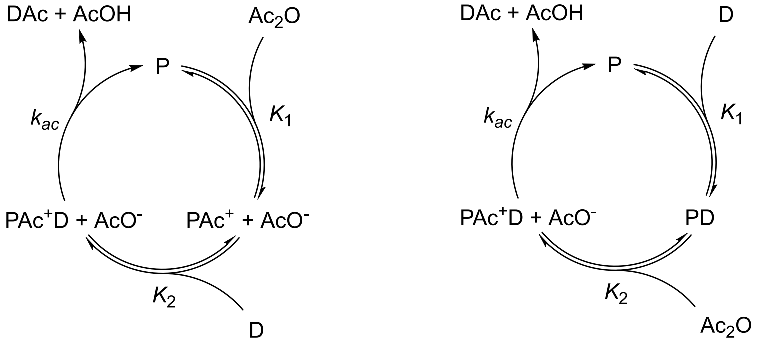

(a) catalytic cycle 1 (b) catalytic cycle 2

Figure S65: Catalytic cycles investigated in this work.

Reaction conditions at which the selectivity exceeds 50 in favor of the (*R*,*R*)-enantiomer of diol **2** were reported at a temperature of 273 K in the non-polar solvent toluene ($\varepsilon \approx 2.4$). The concentrations were 5.4 mM of *trans*-cyclohexane-1,2-diol (*rac*-**2**), 0.054 mM of peptide catalyst (**1**), and a 5.3-fold excess of acetic anhydride relative to the diol. The (*R*,*R*)-enantiomer was depleted to > 99 % within 5 hours.[3] Errors of about 4 % can be assumed for the selectivity for values between 50 and 75.[75]

9.1 Calculation of Selectivity for the two Catalytic Cycles

The selectivity $s > 50$[3] was determined previously by the method of Kagan and Fiaud[76] (Equation 53), assuming first-order kinetics (Equation 54) and the absence of nonlinear effects. Here, the rate constant k_{RR} specifies (*R*,*R*)-**2** as the faster reacting enantiomer, while (*S*,*S*)-**2** is the slower reacting diol with rate constant k_{SS} ($k_{RR} > k_{SS}$), with symbols in brackets denoting the concentrations of the respective species.

$$s = \frac{k_{RR}}{k_{SS}} \tag{53}$$

$$\frac{\mathrm{d}}{\mathrm{d}t}[\mathrm{D}_{RR}] = -k_{RR}[\mathrm{D}_{RR}], \qquad \frac{\mathrm{d}}{\mathrm{d}t}[\mathrm{D}_{SS}] = -k_{SS}[\mathrm{D}_{SS}] \tag{54}$$

The integrated rate laws (Equation 55) can be determined analytically.

$$[\mathrm{D}_{RR}] = [\mathrm{D}_{RR}]_0 \exp(-k_{RR}t), \qquad [\mathrm{D}_{SS}] = [\mathrm{D}_{SS}]_0 \exp(-k_{SS}t) \tag{55}$$

To compare the proposed catalytic cycles with the previous results, an expression for the selectivity of a kinetic resolution is necessary. Both catalytic cycles in Figure S65 feature an overall third-order rate law ($[\mathrm{P}][\mathrm{Ac_2O}][\mathrm{D}]$). The selectivity can be determined in a similar procedure as in References 77 and 78 to account for nonlinear effects, which are expected to occur for non-first order processes. The overall differential rate laws are thus rewritten to Equations 56 and 57.

$$-k_{RR}[\mathrm{D}_{RR}] = -k_{ac,RR}K_{1,RR}K_{2,RR}[\mathrm{P}][\mathrm{Ac_2O}][\mathrm{D}_{RR}] \tag{56}$$

$$-k_{SS}[\mathrm{D}_{SS}] = -k_{ac,SS}K_{1,SS}K_{2,SS}[\mathrm{P}][\mathrm{Ac_2O}][\mathrm{D}_{SS}] \tag{57}$$

Inserting Equations 56 and 57 in Equation 53 yields the selectivity assuming either catalytic cycle 1 or 2 is the underlying mechanism (Equation 58). This relation is used in Tables S36 and S38 to obtain the selectivity.

$$s = \frac{k_{ac,RR}K_{1,RR}K_{2,RR}[\mathrm{P}][\mathrm{Ac_2O}]}{k_{ac,SS}K_{1,SS}K_{2,SS}[\mathrm{P}][\mathrm{Ac_2O}]} = \frac{k_{ac,RR}K_{1,RR}K_{2,RR}}{k_{ac,SS}K_{1,SS}K_{2,SS}} \tag{58}$$

Thus, the selectivity for the kinetic resolution can be obtained by determining the rate and equilibrium constants used for both catalytic cycles in Figure S65. Performing separate reactions with enantiomerically pure starting material allows the determination of these constants in Equation 58.

For the reactions the conversion X is defined by Equation 59, where $[\mathrm{D}]_0$ is the initial diol concentration and DAc means monoacetate **3**.

$$X = 1 - \frac{[\mathrm{D}]}{[\mathrm{D}]_0} = 1 - \frac{[\mathrm{D}]}{[\mathrm{D}] + [\mathrm{DAc}]} \tag{59}$$

Selectivity can also be understood as the ratio of the times required for the two reactions with enantiomerically pure starting material to reach a given, equal conversion (Equation 60). This relation follows when Equations 55 and 59 are inserted into Equation 53. Equation 60 thus provides a way to determine selectivity by graphically analyzing the times required for the reactions to reach the same conversion. For first order kinetics, theory predicts this ratio as constant and thus the selectivity is independent of conversion (*vide infra*, Figure S67d).

$$s(X) = \frac{t_{SS}(X)}{t_{RR}(X)} \tag{60}$$

9.2 Experimental Details Reaction Monitoring

To determine the macroscopic reaction rates, we monitored the reactions separately for both enantiomers of **2** with ^{1}H NMR spectroscopy. For this, solutions of one enantiomer **2** at 2.7 mM concentration in toluene-d_8 were prepared with 0.054 mM catalyst **1** (2 mol-%). All reactions were performed at 0 °C and all solutions were brought to that temperature prior to initiation. Reaction rates determined with NMR spectroscopy are known to be dependent on the monitoring method.[79] Therefore, we conducted catalytic reactions in separate flasks (3.2 mL total volume). The reaction progress was then analyzed by ^{1}H NMR spectroscopy at six different times. At each time point about 0.4 mL aliquots were taken and quenched with 50 µL methanol-d_4. Reactions in NMR tubes were performed without stirring for both enantiomers of **2** (total volume of 0.4 mL). After initiation with the corresponding amount of acetic anhydride (5.3-fold excess relative to the diol) the tubes are shaken vigorously, brought into the spectrometer, and the reactions were followed by series of ^{1}H NMR spectra. The specific reaction conditions and concentrations used are given in Table S34. The resulting time profiles (Figure S66) were fitted under the assumption of the catalytic cycles shown in Figure S65. Here, the conversion is directly accessible via integration of the measured spectra, where the sum of remaining diol **2** (3.03 ppm, 2 H) and monoacetate **3** (3.32 ppm, 1 H) is set to 100 % at each time point taking the number of contributing nuclei into account.

Table S34: Initial concentrations used for the determination of reaction rates.

Diol	vessel	mixing	$[\mathrm{D}]_t$ / mM	$[\mathrm{P}]_t$ / mM	$[\mathrm{Ac_2O}]_t$ / mM	V / mL	sample
(*R*,*R*)-**2**	flask	stirred	2.645	0.052	13.994	3.331	jn-150
(*S*,*S*)-**2**	flask	stirred	2.635	0.053	13.834	3.280	jn-149
(*R*,*R*)-**2**	NMR tube	static	2.749	0.049	12.885	0.500	jn-151
(*S*,*S*)-**2**	NMR tube	static	2.703	0.048	13.643	0.414	jn-147
(*R*,*R*)-**2**	NMR tube	static	2.696	0.059	3.124	0.402	jn-146

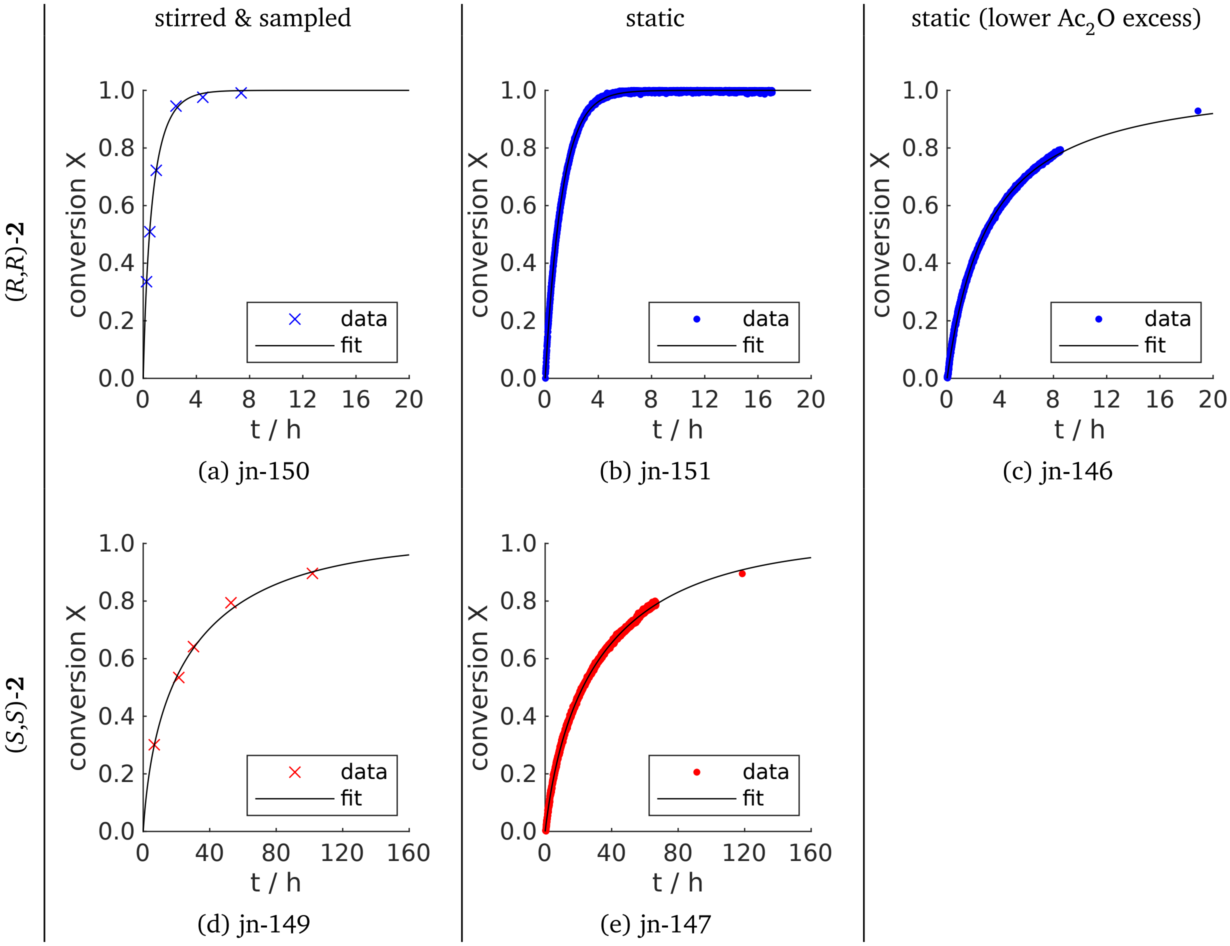

(a) jn-150
(b) jn-151
(c) jn-146
(d) jn-149
(e) jn-147

Figure S66: Conversions versus time during catalysis of **2** with 2 mol-% **1** at 0 °C. Solutions in (a) and (d) were stirred, while (b), (c) and (e) show the reactions as conducted in NMR tubes without additional mixing. The solid lines are the corresponding fits assuming catalytic cycle 1 is present. For plot (c) and (e) additional single point measurements were performed after the original measurement was finished.

9.3 Fitting Procedure

The catalytic cycles were fitted to the experimental data as a system of differential equations similar to the procedure described in section 3.1. The rate constants were varied and then the system of differential equations was solved for each set of rate constants until the best possible fit (low RMSD) is obtained. For this, each forward reaction rate was defined as $k_{i,f} = K_i a_i$ and each back-reaction rate as $k_{i,b} = a_i$, with K_i being the equilibrium constant and a_i a speed factor (also a rate constant). The quotient of the forward and back-reaction rate still gives $k_{i,f}/k_{i,b} = K_i$. We attempted to model the factors a_2 in cycle 1 and a_1 in cycle 2 (addition of diol to the catalyst) to be close to diffusion limited rate constants[80] ($\sim 10^8\ \mathrm{s}^{-1}$) to ensure, that these equilibria were established faster then the reaction proceeds. However, the values for these factors had to be fixed at $10^4\ \mathrm{s}^{-1}$ because higher values induced instabilities when numerically solving the system of differential equations. Doing so did not change the result. As a final restraint, the factors a_i were required to be greater than the rate constant k_{ac}, so that the equilibria were established faster than the reaction progressed.

9.4 Catalytic Cycle 1

For catalytic cycle 1 (Figure S65a), the differential equation 61 in the form of $u = \frac{\mathrm{d}}{\mathrm{d}t}\mathbf{c} = \boldsymbol{\nu}\mathbf{r}^T$ can be formulated. Fitting this cycle to the changing diol concentration (as shown in Figure S66) leads to the equilibrium constants and reaction rate constants given in Table S35. The equilibrium constants determined are presented as Gibbs energy in Table S36. The selectivity s (Equation 58) for each pair under identical conditions is also given.

$$u = \frac{\mathrm{d}}{\mathrm{d}t}\begin{pmatrix} [\mathrm{P}] \\ [\mathrm{D}] \\ [\mathrm{Ac_2O}] \\ [\mathrm{PAc}] \\ [\mathrm{PAcD}] \\ [\mathrm{AcO}] \\ [\mathrm{DAc}] \end{pmatrix} = \begin{pmatrix} -1 & 1 & 0 & 0 & 1 \\ 0 & 0 & -1 & 1 & 0 \\ -1 & 1 & 0 & 0 & 0 \\ 1 & -1 & -1 & 1 & 0 \\ 0 & 0 & 1 & -1 & -1 \\ 1 & -1 & 0 & 0 & 0 \\ 0 & 0 & 0 & 0 & 1 \end{pmatrix} \cdot \begin{pmatrix} k_{1,f}[\mathrm{P}][\mathrm{Ac_2O}] \\ k_{1,b}[\mathrm{PAc}][\mathrm{AcO}] \\ k_{2,f}[\mathrm{PAc}][\mathrm{D}] \\ k_{2,b}[\mathrm{PAcD}] \\ k_{ac}[\mathrm{PAcD}] \end{pmatrix}^T \tag{61}$$

Table S35: Equilibrium constants derived for the equilibria and the reaction rate for the final step in the catalytic cycle 1 (Figure S65a) with peptide **1** at 0 °C.

Diol	mixing	K_1	K_2 / M^{-1}	k_{ac} / s^{-1}	RMSD
(R,R)-**2**	stirred	0.045	55	52.9×10^{-2}	2.156×10^{-5}
(S,S)-**2**	stirred	0.037	21	2.6×10^{-2}	3.973×10^{-5}
(R,R)-**2**	static	0.050	61	50.0×10^{-2}	1.340×10^{-5}
(S,S)-**2**	static	0.092	15	2.7×10^{-2}	1.550×10^{-5}
(R,R)-**2**	static[a]	0.046	58	53.0×10^{-2}	1.728×10^{-5}

[a] reaction with 3 mM $\mathrm{Ac_2O}$, see Table S34

Table S36: Gibbs energies determined for the catalytical acetylation reaction with peptide **1** at 0 °C.

Diol	mixing	ΔG_1 / kJ mol^{-1}	ΔG_2 / kJ mol^{-1}	$k_{ac}K_1K_2$ / M^{-1} s^{-1}	selectivity s
(R,R)-**2**	stirred	7.0	−9.1	1.330	63
(S,S)-**2**	stirred	7.4	−6.9	0.021	
(R,R)-**2**	static	6.9	−9.3	1.488	55
(S,S)-**2**	static	5.5	−6.1	0.027	
(R,R)-**2**	static[a]	7.0	−9.2	1.424	

[a] reaction with 3 mM $\mathrm{Ac_2O}$, see Table S34

9.5 Catalytic Cycle 2

For catalytic cycle 2 (Figure S65b), the differential Equation 62 in the form of $u = \frac{\mathrm{d}}{\mathrm{d}t}\mathbf{c} = \boldsymbol{\nu}\mathbf{r}^T$ can be formulated. Fitting this cycle to the changing diol concentration (as shown in Figure S66) leads to the equilibrium constants and reaction rate constants given in Table S37. The equilibrium constants determined are presented as Gibbs energy in Table S38. The selectivity s (Equation 58) for each pair under identical conditions is also given.

$$u = \frac{\mathrm{d}}{\mathrm{d}t}\begin{pmatrix}[\mathrm{P}]\\ [\mathrm{D}]\\ [\mathrm{Ac_2O}]\\ [\mathrm{PD}]\\ [\mathrm{PAcD}]\\ [\mathrm{AcO}]\\ [\mathrm{DAc}]\end{pmatrix} = \begin{pmatrix}-1 & 1 & 0 & 0 & 1\\ -1 & 1 & 0 & 0 & 0\\ 0 & 0 & -1 & 1 & 0\\ 1 & -1 & -1 & 1 & 0\\ 0 & 0 & 1 & -1 & -1\\ 0 & 0 & 1 & -1 & 0\\ 0 & 0 & 0 & 0 & 1\end{pmatrix} \cdot \begin{pmatrix}k_{1,f}[\mathrm{P}][\mathrm{D}]\\ k_{1,b}[\mathrm{PD}]\\ k_{2,f}[\mathrm{PD}][\mathrm{Ac_2O}]\\ k_{2,b}[\mathrm{PAcD}][\mathrm{AcO}]\\ k_{ac}[\mathrm{PAcD}]\end{pmatrix}^T \tag{62}$$

Table S37: Equilibrium constants derived for the equilibria and the reaction rate for the final step in the catalytic cycle 2 (Figure S65b) with peptide **1** at 0 °C.

Diol	mixing	K_1 / M^{-1}	K_2	k_{ac} / s^{-1}	RMSD
(*R*,*R*)-**2**	stirred	78	0.73	44.5×10^{-2}	2.152×10^{-5}
(*S*,*S*)-**2**	stirred	2.5	0.19	5.7×10^{-2}	4.062×10^{-5}
(*R*,*R*)-**2**	static	330	0.037	36.0×10^{-2}	1.167×10^{-5}
(*S*,*S*)-**2**	static	7.3	0.094	4.5×10^{-2}	1.551×10^{-5}
(*R*,*R*)-**2**	static[a]	110	0.12	55.7×10^{-2}	1.664×10^{-5}

[a] reaction with 3 mM Ac_2O, see Table S34

Table S38: Gibbs energies determined for the catalytical acetylation reaction with peptide **1** at 0 °C.

Diol	mixing	ΔG_1 / kJ mol^{-1}	ΔG_2 / kJ mol^{-1}	$k_{ac}K_1K_2$ / $\mathrm{M}^{-1}\,\mathrm{s}^{-1}$	selectivity s
(*R*,*R*)-**2**	stirred	−4.7	0.7	2.514	91
(*S*,*S*)-**2**	stirred	−2.1	3.8	0.028	
(*R*,*R*)-**2**	static	−13.2	7.5	4.327	138
(*S*,*S*)-**2**	static	−4.5	5.4	0.031	
(*R*,*R*)-**2**	static[a]	−10.7	4.7	7.699	

[a] reaction with 3 mM Ac_2O, see Table S34

9.6 Comparison of Both Catalytic Cycles

As shown in the Tables S35 and S37 the experimental data fit reasonably well (low RMSDs) for both catalytic cycles. However, one would expect to obtain consistent values for equilibrium constants and reaction rate constants for the same diol ((*R*,*R*)-**2** vs. (*S*,*S*)-**2**). As is detailed below, this is not the case and thus this provides a more substantial indicator to decide between the two cycles.

The catalytic cycle 2 showed more fluctuations than cycle 1. The first step in catalytic cycle 2 should be independent of the diol employed and thus ideally give identical values for both enantiomers – one would at least expect consistent vaues for each respective enantiomer. This is not observed: The fits of cycle 2 for (*R*,*R*)-**2** yielded varying Gibbs energies of -4.7, -13.2 and $-10.7\,\mathrm{kJ\,mol^{-1}}$ for the first step (Table S38). In turn, the same cycle yielded -2.1 and $-4.5\,\mathrm{kJ\,mol^{-1}}$ for (*S*,*S*)-**2**. Ideally, those values should be independent on concentration and measurement method (*e.g.* reaction monitoring with and without stirring, chemical shift analysis, STD) and thus consistent with each other. Positive Gibbs energies for the second step in cycle 2 are in agreement with the observation of low peptide acylium ion concentrations. This makes cycle 2 less plausible.

Catalytic cycle 1 on the other hand leads to more consistent results in these aspects. The first step of cycle 1 gave positive Gibbs energies (Table S36), meaning the equilibrium is located on the side of the peptide and acetic anhydride. For all five reactions performed the resulting Gibbs energies in the first step (addition of acetic anhydride) vary less than those of the corresponding step in cycle 2 (step 2). These energies are reproduced well and are independent of the diol used, as would be expected: The same equilibrium constants in the second step in cycle 1 were determined for (*R*,*R*)-**2** (on average $-9.2\,\mathrm{kJ\,mol^{-1}}$) and (*S*,*S*)-**2** (on average $-6.5\,\mathrm{kJ\,mol^{-1}}$). The same is true if a smaller excess of acetic anhydride was provided.

The previously determined selectivities can be reproduced ($s > 50$[3]) for both catalytic cycles. However, also here significant differences exist, which point towards catalytic cycle 1 being operative: Equation 60 can be used for estimating the selectivity by analyzing the time-conversion-profiles (Figure S66) of the reactions with (*R*,*R*)-**2** and (*S*,*S*)-**2** under identical conditions. This provides a graphical approach to the selectivity. Conversions can either be interpolated or extrapolated directly from the experimental data. Thus, this estimate is largely invariant to the chosen cycle (model-free). Both catalytic cycles can be fitted reasonably well, which allows accurate interpolating. Figure S67e and S67f show very similar dependency on conversion with a maximum value of 50 to 60, when the selectivity is determined with Equation 60. When comparing the selectivity-conversion-profiles with the standard case (first-order kinetics, Figure S67d), the nonlinear effects present in this reaction are evident from both plots. The selectivities obtained from this graphical procedure are in accordance with those obtained by Equation 58 for catalytic cycle 1 (63 and 55, see Table S36), but not for cycle 2 (91 and 138, see Table S38), despite the fact the concentrations are described equally well with both cycles.

Additionally, in cycle 1, the formation of a catalyst acylium ion prior to the acyl transfer onto the alcohol is in line with previous investigations, where 4-(dimethylamino)pyridine (DMAP) as achiral catalyst has been investigated.[59] Furthermore, the cycle is consistent with the mechanistic proposal of the acylation of *trans*-2-*N*-acetamidocyclohexanol,[57] *myo*-inositols, and glycerols[56] with imidazole derivatives as catalyst.

We determined a difference in Gibbs energy of about $3\,\mathrm{kJ\,mol^{-1}}$ in favor of (*R*,*R*)-**2**. This is approximately the same energy difference as determined by chemical shift analysis (section 3.3.6) and STD (section 8). However, under catalytic conditions this is the affinity of the peptide acylium ion to the diol and not the plain peptide to the diol – as is the case for the NMR titration and STD experiments. Therefore, selectivity can be attributed to the peptide and additional influence of the acyl group seems negligible. This means that spectroscopic investigations of selectivity on this or related catalysts do not necessarily have to be performed on the reactive intermediate.

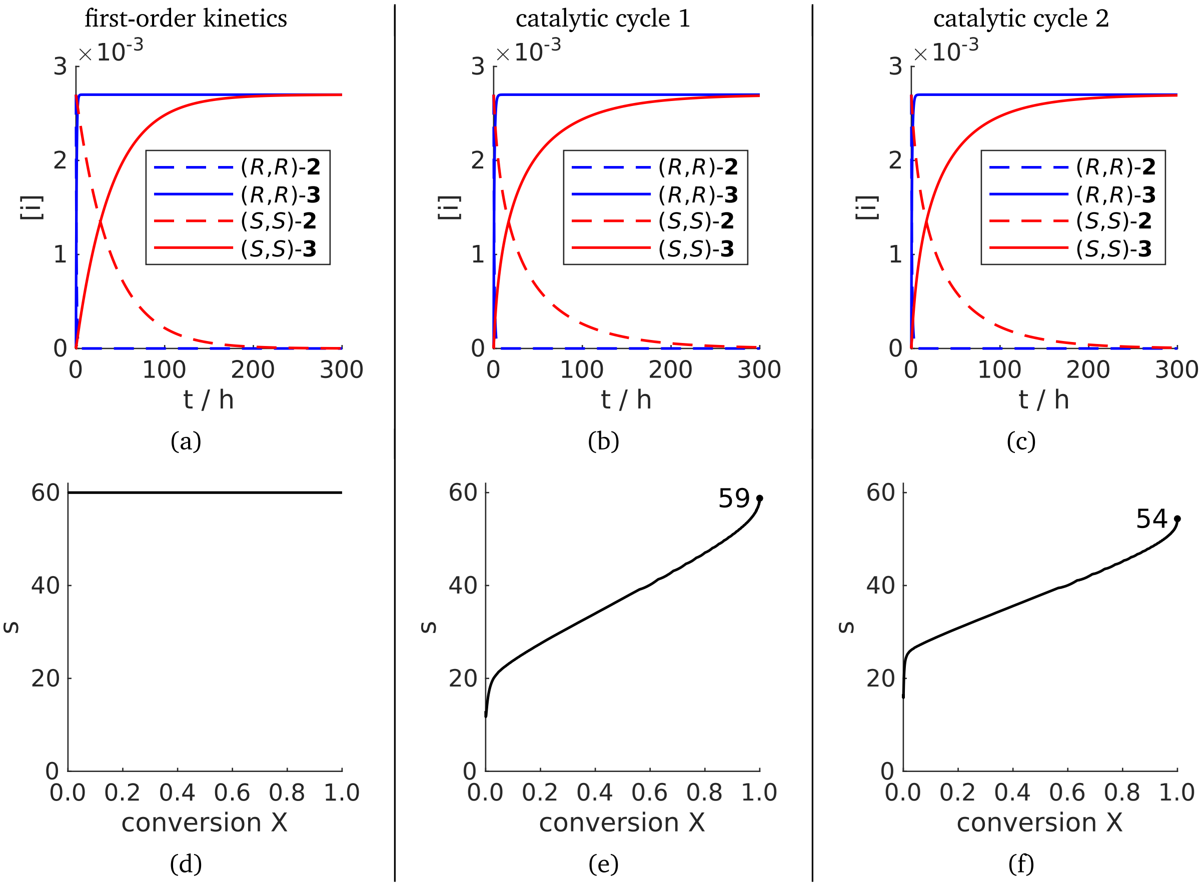

(a) (b) (c)

(d) (e) (f)

Figure S67: Hypothetical kinetic resolutions of 5.4 mM *rac*-**2** with 0.054 mM catalyst and a 5.3-fold excess of acetic anhydride calculated by numerically solving the corresponding differential equations. For comparison with the simplest case first-order kinetics were assumed in the first column with rate constants $k_{RR} = 420 \times 10^{-6}\,\mathrm{s}^{-1}$ and $k_{SS} = 7 \times 10^{-6}\,\mathrm{s}^{-1}$ to roughly match the reaction progress as observed in the experiment and providing a selectivity of $s = 60$. In the second and third column the catalytic cycles 1 and 2, respectively, are assumed. The parameters retrieved from the stirred reactions (first two entries of Tables S35 and S37) are used for this. The first row depicts the concentration-time-profiles of all three cases. (*R*,*R*)-diol is consumed fast, but the reaction of (*S*,*S*)-diol takes several hundred hours to complete. The plots in the second row are derived from the times required to reach a particular conversion (Equation 60). For the first-order kinetics no dependency on the conversion is present and the selectivity of 60 is reproduced.

10 Saturation Profile of ESnob Cascades in STD Spectra

The saturation profile of an ESnob[22] pulse cascade was determined by utilizing the 1D variant of the STD pulse sequence used herein. The results of this section were measured on the *Bruker* standard sample Z10120, that consisted of 0.1 % ethylbenzene in $CDCl_3$. The excited molecule ethylbenzene is thought to show no interactions with surrounding molecules, so in an ideal STD experiment exciting non-intramolecular resonances would give no STD response. Also it exhibits signals with multiplet structures, like the excited resonances in peptide **1**. A 10 ms ESnob with 1 ms interpulse delay and a fixed saturation time of 15 s (cascade of 1364 individual pulses) was chosen. The pulse power was calculated according to a single, selective 90° pulse (*Bruker shapetool*). For analysis the relative intensity of the CH_2-group in ethylbenzene (ca. 2.67 ppm) in $CDCl_3$ was monitored with varying irradiation offsets between 1.90 ppm and 3.50 ppm in steps of 0.05 ppm. The final saturation profile of an ESnob pulse cascade is shown in Figure S68. This can be used as an estimate how broad the saturation profile of the pulse cascade will be. From the offset about 2.5 times of the calculated bandwidth of a single pulse no significant excitation was observed. For comparison, the profile of a single ESnob pulse is simulated with the *NMR-SIM* tool of *Topspin 4.0.8*. For this, 1201 points were calculated between −600 Hz to 600 Hz with the ESnob shape (`ESnob.1000`) and a pulse length (P0) of 10 ms and a power (SP0) of 56.14 Hz. The resulting transverse xy-magnetization is plotted in Figure S68 as $1 - M_{xy}$ in order to establish comparability.

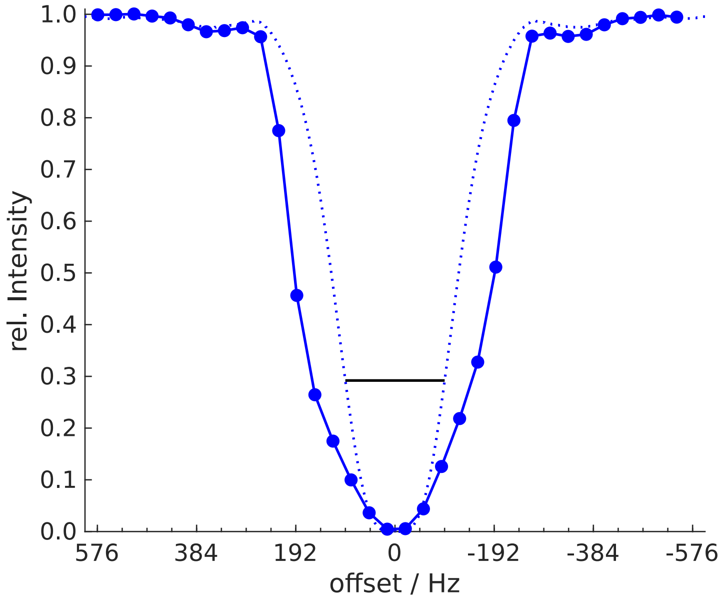

Figure S68: Saturation profile of an ESnob cascade after 15 s saturation time as function of irradiation frequency. The dotted line is the expected profile of a single ESnob pulse (details are given in this section) and the black solid line indicates the calculated excitation bandwidth at the 3 dB point.

11 Content of the Supplementary Material and Data

Supplementary materials and raw experimental data is provided at DOI 10.5281/zenodo.7872629, where the following contents can be found:

- Matlab scripts with examples
- experimental spectra (203 experiments of *rac*-**2** in toluene; 248 experiments of **1** in toluene; 46 experiments of **1** in dichloromethane; 47 experiments of **1** in acetone; 25 experiments reaction monitoring in toluene; 772 experiments of **1** with (*R*,*R*)-**2** in toluene; 423 experiments of **1** with (*S*,*S*)-**2** in toluene)
- spreadsheets with extracted observables (chemical shifts, relaxation rates, diffusion coefficients, STD amplification factors, time-dependent diol concentrations)
- *Bruker* pulse sequence codes (1D and pseudo-2D) of the STD experiment used

References

(1) (a) Procházková, E.; Kolmer, A.; Ilgen, J.; Schwab, M.; Kaltschnee, L.; Fredersdorf, M.; Schmidts, V.; Wende, R. C.; Schreiner, P. R.; Thiele, C. M. *Angew. Chem. Int. Ed.* **2016**, *55*, 15754–15759; (b) Procházková, E.; Kolmer, A.; Ilgen, J.; Schwab, M.; Kaltschnee, L.; Fredersdorf, M.; Schmidts, V.; Wende, R. C.; Schreiner, P. R.; Thiele, C. M. *Angew. Chem.* **2016**, *128*, 15986–15991.

(2) Harris, R. K.; Becker, E. D.; De Menezes, S. M. C.; Granger, P.; Hoffman, R. E.; Zilm, K. W. *Magn. Reson. Chem.* **2008**, *46*, 582–598.

(3) (a) Müller, C. E.; Wanka, L.; Jewell, K.; Schreiner, P. R. *Angew. Chem. Int. Ed.* **2008**, *47*, 6180–6183; (b) Müller, C. E.; Wanka, L.; Jewell, K.; Schreiner, P. R. *Angew. Chem.* **2008**, *120*, 6275–6278.

(4) Fulmer, G. R.; Miller, A. J. M.; Sherden, N. H.; Gottlieb, H. E.; Nudelman, A.; Stoltz, B. M.; Bercaw, J. E.; Goldberg, K. I. *Organometallics* **2010**, *29*, 2176–2179.

(5) Findeisen, M.; Brand, T.; Berger, S. *Magn. Reson. Chem.* **2007**, *45*, 175–178.

(6) Koos, M. R. M.; Kummerlöwe, G.; Kaltschnee, L.; Thiele, C. M.; Luy, B. *Angew. Chem. Int. Ed.* **2016**, *55*, 7655–7659.

(7) Foroozandeh, M.; Adams, R. W.; Meharry, N. J.; Jeannerat, D.; Nilsson, M.; Morris, G. A. *Angew. Chem. Int. Ed.* **2014**, *53*, 6990–6992.

(8) Thiele, C. M.; Petzold, K.; Schleucher, J. *Chem. Eur. J.* **2009**, *15*, 585–588.

(9) Gyöngyösi, T.; Timári, I.; Haller, J.; Koos, M. R. M.; Luy, B.; Kövér, K. E. *ChemPlusChem* **2018**, *83*, 53–60.

(10) Aguilar, J. A.; Nilsson, M.; Bodenhausen, G.; Morris, G. A. *Chem. Commun.* **2012**, *48*, 811–813.

(11) Jerschow, A.; Müller, N. *J. Magn. Reson.* **1997**, *125*, 372–375.

(12) (a) Mayer, M.; Meyer, B. *Angew. Chem. Int. Ed.* **1999**, *38*, 1784–1788; (b) Mayer, M.; Meyer, B. *Angew. Chem.* **1999**, *111*, 1902–1906.

(13) Zhou, Z.; Kümmerle, R.; Qiu, X.; Redwine, D.; Cong, R.; Taha, A.; Baugh, D.; Winniford, B. *J. Magn. Reson.* **2007**, *187*, 225–233.

(14) Shaka, A.; Keeler, J.; Freeman, R. *J. Magn. Reson.* **1983**, *53*, 313–340.

(15) Shaka, A.; Keeler, J.; Frenkiel, T.; Freeman, R. *J. Magn. Reson.* **1983**, *52*, 335–338.

(16) (a) Böhlen, J.-M.; Burghardt, I.; Rey, M.; Bodenhausen, G. *J. Magn. Reson.* **1990**, *90*, 183–191; (b) Böhlen, J.-M.; Rey, M.; Bodenhausen, G. *J. Magn. Reson.* **1989**, *84*, 191–197.

(17) Davis, A. L.; Keeler, J.; Laue, E. D.; Moskau, D. *J. Magn. Reson.* **1992**, *98*, 207–216.

(18) Cicero, D. O.; Barbato, G.; Bazzo, R. *J. Magn. Reson.* **2001**, *148*, 209–213.

(19) Kogler, H.; Sørensen, O.; Bodenhausen, G.; Ernst, R. *J. Magn. Reson.* **1983**, *55*, 157–163.

(20) Vold, R. L.; Waugh, J. S.; Klein, M. P.; Phelps, D. E. *J. Chem. Phys.* **1968**, *48*, 3831–3832.

(21) Sinnaeve, D. *Concepts Magn. Reson.* **2012**, *40A*, 39–65.

(22) Kupče, E.; Boyd, J.; Campbell, I. D. *J. Magn. Reson.* **1995**, *106*, 300–303.

(23) Ley, N. B.; Rowe, M. L.; Williamson, R. A.; Howard, M. J. *RSC Adv.* **2014**, *4*, 7347.

(24) Gossert, A. D.; Jahnke, W. *Prog. Nucl. Magn. Reson. Spectrosc.* **2016**, *97*, 82–125.

(25) Thordarson, P. *Chem. Soc. Rev.* **2011**, *40*, 1305–1323.

(26) Atkins, P. W.; De Paula, J. *Physical chemistry*, 8th ed.; Oxford University Press: Oxford; New York, 2006.

(27) Lagarias, J. C.; Reeds, J. A.; Wright, M. H.; Wright, P. E. *SIAM J. Optim.* **1998**, *9*, 112–147.

(28) De Levie, R. *J. Chem. Educ.* **1999**, *76*, 1594–1598.

(29) Shampine, L. F.; Reichelt, M. W. *SIAM J. Sci. Comput.* **1997**, *18*, 1–22.

(30) Shampine, L. F.; Reichelt, M. W.; Kierzenka, J. A. *SIAM Rev.* **1999**, *41*, 538–552.

(31) Martin, R. B. *Chem. Rev.* **1996**, *96*, 3043–3064.

(32) Lopes Jesus, A. J.; Redinha, J. S. *J. Mol. Struct.* **2014**, *1067*, 104–111.

(33) Hess, G. H. *Ann. Phys.* **1840**, *126*, 385–404.

(34) Sandler, S. I.; Woodcock, L. V. *J. Chem. Eng. Data* **2010**, *55*, 4485–4490.

(35) Hahn, E. L. *Phys. Rev.* **1950**, *80*, 580–594.

(36) Stejskal, E. O.; Tanner, J. E. *J. Chem. Phys.* **1965**, *42*, 288–292.

(37) Johnson, C. S.; Wu, D. *eMagRes* **2011**, 1–24.

(38) Einstein, A. *Ann. Phys.* **1905**, *322*, 549–560.

(39) Neufeld, R.; Stalke, D. *Chemical Science* **2015**, *6*, 3354–3364.

(40) Kabelac, S.; Kind, M.; Martin, H.; Mewes, D.; Schaber, K.; Stephan, P. *VDI-Wärmeatlas*; Springer Berlin Heidelberg: Berlin, Heidelberg, 2013.

(41) Price, W. S.; Tsuchiya, F.; Arata, Y. *J. Am. Chem. Soc.* **1999**, *121*, 11503–11512.

(42) Alex, A.; Millan, D. S.; Perez, M.; Wakenhut, F.; Whitlock, G. A. *Med. Chem. Commun.* **2011**, *2*, 669–674.

(43) Ajitha, M.; Huang, K.-W. *Synthesis* **2016**, *48*, 3449–3458.

(44) Born, M. *Z. Physik* **1920**, *1*, 45–48.

(45) Nageswara Rao, C.; Ramanaiah, M.; Sailaja, B. B. V. *Chem. Speciation Bioavailability* **2014**, *26*, 266–272.

(46) Fujii, Y.; Yamada, H.; Mizuta, M. *J. Phys. Chem.* **1988**, *92*, 6768–6772.

(47) Shirota, H.; Fukuda, T.; Kato, T. *J. Phys. Chem.* **2013**, *117*, 16196–16205.

(48) Cook, J. L.; Hunter, C. A.; Low, C. M. R.; Perez-Velasco, A.; Vinter, J. G. *Angew. Chem. Int. Ed.* **2007**, *46*, 3706–3709.

(49) Haynes, W. M., Lide, D. R., Eds. *CRC Handbook of Chemistry and Physics*, 96th ed.; CRC Press: Boca Raton, Fla., 2015.

(50) Fielding, L. *Prog. Nucl. Magn. Reson. Spectrosc.* **2007**, *51*, 219–242.

(51) Ni, F. *Prog. Nucl. Magn. Reson. Spectrosc.* **1994**, *26*, 517–606.

(52) Viegas, A.; Manso, J.; Nobrega, F. L.; Cabrita, E. J. *J. Chem. Educ.* **2011**, *88*, 990–994.

(53) Angulo, J.; Enríquez-Navas, P. M.; Nieto, P. M. *Chem. Eur. J.* **2010**, *16*, 7803–7812.

(54) Kemper, S.; Patel, M. K.; Errey, J. C.; Davis, B. G.; Jones, J. A.; Claridge, T. D. *J. Magn. Reson.* **2010**, *203*, 1–10.

(55) Vom, A.; Headey, S.; Wang, G.; Capuano, B.; Yuriev, E.; Scanlon, M. J.; Simpson, J. S. *Aust. J. Chem.* **2013**, *66*, 1518–1524.

(56) Metrano, A. J.; Miller, S. J. *Acc. Chem. Res.* **2019**, *52*, 199–215.

(57) Liao, R.-Z.; Santoro, S.; Gotsev, M.; Marcelli, T.; Himo, F. *ACS Catal.* *6*, 1165–1171.

(58) Brauser, M.; Heymann, T.; Thiele, C. M. *Molecules* **2022**, *27*, 6351.

(59) Xu, S.; Held, I.; Kempf, B.; Mayr, H.; Steglich, W.; Zipse, H. *Chem. Eur. J.* **2005**, *11*, 4751–4757.

(60) Furuta, T.; Kawabata, T. In *Asymmetric Organocatalysis 1: Lewis Base and Acid Catalysts*; List, B., Ed.; Georg Thieme Verlag: Stuttgart, 2012; pp 497–546.

(61) Smith, A. D.; Woods, P. A. In *Asymmetric Organocatalysis 1: Lewis Base and Acid Catalysts*; List, B., Ed.; Georg Thieme Verlag: Stuttgart, 2012; pp 547–590.

(62) Bonduelle, C.; Martín-Vaca, B.; Cossío, F. P.; Bourissou, D. *Chem. Eur. J.* **2008**, *14*, 5304–5312.

(63) Lamaty, G.; Mary, F.; Roque, J. P. *J. Chim. Phys. Phys.-Chim. Biol.* **1991**, *88*, 1793–1810.

(64) Guibe-Jampel, E.; Le Corre, G.; Wakselman, M. *Tetrahedron Lett.* **1979**, *20*, 1157–1160.

(65) (a) Höfle, G.; Steglich, W.; Vorbrüggen, H. *Angew. Chem. Int. Ed.* **1978**, *17*, 569–583; (b) Höfle, G.; Steglich, W.; Vorbrüggen, H. *Angew. Chem.* **1978**, *90*, 602–615.

(66) Lutz, V.; Glatthaar, J.; Würtele, C.; Serafin, M.; Hausmann, H.; Schreiner, P. R. *Chem. Eur. J.* **2009**, *15*, 8548–8557.

(67) (a) Bülow, M.; Ascani, M.; Held, C. *Fluid Phase Equilib.* **2021**, *535*, 112967; (b) Bülow, M.; Ascani, M.; Held, C. *Fluid Phase Equilib.* **2021**, *537*, 112989.

(68) Bordwell, F. G. *Acc. Chem. Res.* **1988**, *21*, 456–463.

(69) Pandit, N. K.; Connors, K. A. *J. Pharm. Sci.* **1982**, *71*, 485–491.

(70) Benoit, R. L.; Boulet, D.; Séguin, L.; Fréchette, M. *Can. J. Chem.* **1985**, *63*, 1228–1232.

(71) Klicić, J. J.; Friesner, R. A.; Liu, S.-Y.; Guida, W. C. *J. Phys. Chem.* **2002**, *106*, 1327–1335.

(72) Kolthoff, I. M.; Chantooni, M. K.; Bhowmik, S. *J. Am. Chem. Soc.* **1968**, *90*, 23–28.

(73) Cox, B. G. *Org. Process Res. Dev.* **2015**, *19*, 1800–1808.

(74) Wolfenden, R.; Jencks, W. P. *J. Am. Chem. Soc.* **1961**, *83*, 4390–4393.

(75) Greenhalgh, M. D.; Taylor, J. E.; Smith, A. D. *Tetrahedron* **2018**, *74*, 5554–5560.
(76) Kagan, H. B.; Fiaud, J. C. *Top. Stereochem.* **1988**, *18*, 249–330.
(77) Johnson, D. W.; Singleton, D. A. *J. Am. Chem. Soc.* **1999**, *121*, 9307–9312.
(78) Blackmond, D. G. *Journal of the American Chemical Society* **2001**, *123*, 545–553.
(79) Foley, D. A.; Dunn, A. L.; Zell, M. T. *Magn. Reson. Chem.* **2016**, *54*, 451–456.
(80) Meyer, B.; Peters, T. *Angew. Chem. Int. Ed.* **2003**, *42*, 864–890.